Modeling, Theoretical and Observational Studies of the Lunar Photoelectron Sheath

by

Andrew Reinhold Poppe

B.A., Physics, *summa cum laude*

B.A., Mathematics

University of Colorado, Boulder, CO, 2006

A thesis submitted to the

Faculty of the Graduate School of the

University of Colorado in partial fulfillment

of the requirements for the degree of

Doctor of Philosophy

Department of Physics

2011

This thesis entitled:
Modeling, Theoretical and Observational Studies of the Lunar Photoelectron Sheath
written by Andrew Reinhold Poppe
has been approved for the Department of Physics

Mihály Horányi

Scott Robertson

Date _____

The final copy of this thesis has been examined by the signatories, and we find that both the content and the form meet acceptable presentation standards of scholarly work in the above mentioned discipline.

Poppe, Andrew Reinhold (Ph.D., Physics)

Modeling, Theoretical and Observational Studies of the Lunar Photoelectron Sheath

Thesis directed by Prof. Mihály Horányi

The Moon, lacking an atmosphere and a global magnetic field, is directly exposed to both solar ultraviolet radiation and a variety of ambient plasmas. On the lunar dayside, a photoelectron sheath develops and the surface typically charges positively since the photoemission current is at least an order-of-magnitude greater than any ambient current. This sheath dominates the near-surface plasma environment and controls the charging, levitation and transport of micron-sized dust grains.

In this thesis, we first model the lunar near-surface plasma environment via a one-dimensional particle-in-cell code. The sheath potential, electric field and plasma densities are presented over a wide range of plasma parameters. Additionally, the charging and transport of micron- and sub-micron sized dust grains is modeled via a test-particle approach in an attempt to explain Apollo-era observations of lunar dust dynamics. Secondly, we present a comparison of the particle-in-cell results with theoretical, kinetic derivations of the lunar photoelectron sheath. We extend previous theories to include the presence of a κ-distribution for the solar wind electrons. Finally, we present a comparison of *in-situ* measurements of the lunar photoelectron sheet in the terrestrial plasma sheet by the Lunar Prospector Electron Reflectometer with particle-in-cell simulations to confirm the presence of non-monotonic sheath potentials above the Moon. Future work in all three sections, (simulation, theory and observation) is presented as a guide for continuing research.

Dedication

To my parents, sister and brother, who have provided the support, encouragement, and love for me to pursue my dreams;

And, to Adam, for patiently seeing me through the conclusion of my graduate career, and for being willing to take the next steps by my side.

Acknowledgements

Reflecting upon the work done to accomplish this thesis, I realize that I am indebted to a number of people who have helped me achieve my goals. First and foremost is my advisor, Mihály Horányi, who patiently and enthusiastically guided me from a wide-eyed junior undergraduate to the scientist I am today. Mihály never once hesitated to offer me words of support or to provide me with the tools and opportunities I needed to fully develop my skills.

To Carl, Adam and Scott, who made the late nights and early mornings of grad school infinitely more bearable;

To David Wilson James, for three years of sheer entertainment and camaraderie, whether in Boulder, San Francisco, Montreal, Hampton or Washington D.C;

To Addie, Xu and the rest of the lab folks, for putting up with me wandering around the lab, as well as for finally teaching me not to leave the espresso machine on;

To Jasper Halekas and Greg Delory at SSL/UC Berkeley for suggesting a collaboration regarding LP plasma sheet data;

And, to Jamey and Marcus, who were brave enough to share an office with me, and patient enough to listen to my long-winded digressions on dust.

Contents

Chapter

1 Introduction and Previous Work 1

1.1 The Lunar Plasma Environment 1

1.1.1 Plasma Environments around other Airless Bodies 6

1.2 The Lunar Dust Environment 8

1.2.1 Dust on Other Bodies 14

1.3 Scientific Motivation and Thesis Outline 14

2 Particle-in-Cell Photoelectron Sheath Simulations 17

2.1 One-dimensional PIC Simulations 17

2.2 Photoelectron-Only Sheath 19

2.3 Effect of the Photoelectron Energy Distribution and the Solar Wind 20

2.3.1 Solar UV Variability 25

2.3.2 Solar Zenith Angle Dependence 28

2.3.3 T_{ph} and T_{sw} Dependence 30

2.4 Dust Particle Levitation 32

2.4.1 Levitation Equilibria 32

2.4.2 Levitation Dynamics 37

2.5 Discussion 41

2.6 Ongoing and Future Work 44

2.6.1 Three-dimensional PIC Simulations 44

3 Comparison with Theory 48

3.1 Kinetic Derivation - Maxwellian Solar Wind 49

3.1.1 Comparison of Theory and Simulation 51

3.2 Kinetic Derivation - κ-Distribution Solar Wind 55

3.2.1 Distributions 56

3.2.2 Conditions 57

3.2.3 Monotonic Potential Solutions 68

3.2.4 Non-monotonic Potential Solutions 70

3.3 Future Theoretical Work 73

3.3.1 Energy of Sheath Solutions 73

3.3.2 Photoelectron Sheaths in the Terrestrial Plasma Sheet 73

4 Comparison with In-situ Measurements 75

4.1 Lunar Prospector 75

4.2 Lunar Surface Charging in Daylight - Plasma Sheet 78

4.2.1 Measurements 80

4.2.2 Simulations 83

4.2.3 Summary and Discussion 86

4.3 Future Work 88

4.3.1 Lunar Surface Charging in Daylight - Solar Wind 88

4.3.2 Lunar Secondary Electron Emission 89

4.3.3 Upcoming Measurements: ARTEMIS 91

5 Conclusion 93

5.1 Summary 93

Bibliography 98

Appendix

A Publications 106

A.1 Published Papers: Lunar 106

A.2 Published Papers: Other 106

A.3 Papers in Review 107

A.4 Papers in Preparation 107

Figures

Figure

1.1 A graphic overview of the lunar plasma environment, showing the presence of solar UV radiation, incoming solar wind electrons and ions, and impact-generated secondary electrons. Also denoted is the possible presence of lunar dust dynamics near the terminator region. [*NAC / GSFC / UCB*] 2

1.2 A graphic of the plasma environment on the day-side of the lunar surface. Photoelectrons generated by UV illumination are emitted from the surface and solar wind electrons and ions impinge on the surface. The presence of a non-monotonic potential would reflect some solar wind electrons back to space while trapping some photoelectrons near the surface. [Courtesy: A. Shinn] 3

1.3 The count rate of electrons measured by the Apollo 14 CPLEE instrument during a solar eclipse. As the lunar surface fell into shadow, UV-stimulated photoemission ceased, resulting in a complete drop-out of electrons. This measurement confirms that CPLEE was measuring photoelectrons from the surface. From *Reasoner and Burke* [1972a]. 4

1.4 A schematic of the near-surface plasma environment near an obstacle, such as a boulder or crater rim. While the solar wind electrons easily penetrate into the region just behind the obstacle, the ions cannot respond as fast and thereby set up an ambipolar electric field. The field eventually pulls the ions down and into the 'mini-wake'; however, there may exist a stable electron cloud immediately behind the obstacle. From *Farrell et al.* [2010]. 5

1.5 A schematic of the Mercurian near-surface plasma environment, including solar UV radiation, trapped and escaping photoelectrons and incoming magnetospheric electrons. From *Grard* [1997]. 7

1.6 A schematic of the various plasma environments that a Saturnian moon would be exposed to as it orbits Saturn. The solar UV flux is from a constant direction while the magnetospheric co-rotation flow is constantly swept through different angles with respect to the UV incidence. From *Roussos et al.* [2010]. 8

1.7 An image taken by the Surveyor 7 camera showing lunar horizon glow shortly after sunset (upper glow). The lower glow is the reflection of the primary horizon glow off of the lunar surface [*Colwell et al.*, 2007]. 9

1.8 A series of sketches by Apollo 17 Commander E. Cernan of the coronal-zodiacal light (CZL) and two additional, unexpected features: the shoulders on the main CZL bulge and several, time-dependent 'streamers' [*Zook and McCoy*, 1991]. 11

1.9 A series of images taken a successive times of a dust grain pile exposed to a plasma. Over time, the pile electrostatically spreads out as dust grains charge and are transported horizontally. Additionally, dust grain accumulation on the sides and the top of the insulating rubber block show that the grain movement includes vertical 'hops' in addition to horizontal transport [*Wang et al.*, 2010]. 12

1.10 An image of several dust ponds on the surface of 433 Eros, taken by the NEAR spacecraft during closest approach in 2001 [*Robinson et al.*, 2001]. 15

2.1 (a) The theoretical potential as a function of height above a photoemitting surface with no ambient plasma for three different photoelectron distributions. (b) The theoretical photoelectron density as a function of height for three different photoelectron distributions. Adapted from *Grard and Tunaley* [1971]. 21

2.2 A comparison of 1-d PIC and theoretical results [*Grard and Tunaley*, 1971] for the normalized electron density above a photoemitting plate (with no ambient plasma) for a Maxwellian photoelectron distribution. 22

2.3 A comparison of the various photoelectron velocity distributions normalized to the area under the curve. The solid line is the distribution measured from lunar fines returned by Apollo 17 [*Feuerbacher et al.*, 1972], the diamonds are the function used as the lunar distribution in this paper and the dashed line is the comparable Maxwellian distribution. 23

2.4 A comparison of the particle densities as a function of height for both the lunar and Maxwellian photoelectron sheaths. 24

2.5 A comparison of the sheath potential and electric field above the surface for both the lunar and Maxwellian photoelectron sheaths. 26

2.6 The photoelectron density as a function of height for solar minimum, solar maximum, and flare conditions is shown in (a). An increase in the photoemission current by a factor of ≈ 8 yields a factor of 10 change in the photoelectron density. In (b) the electric field as a function of height for all three cases is shown. The surface electric field increases by ≈ 2 from solar minimum to flare conditions. All three conditions still maintain regions of negative electric field. The inset shows an expanded view of the region from 2 to 3 m, where the fields become negative, to highlight the differences among the three cases. 27

2.7 (a) The potential as a function of height above the lunar surface in the solar wind for a series of solar zenith angles (SZA). As the SZA increases, the sheath switches from non-monotonic to monotonically negative. (b) The surface and minimum potentials for the SZA values modeled in (a). As α increases, both potentials decrease, as does the potential difference between the surface and minimum. At $\alpha = 80°$, the surface and minimum potential values are identical as the sheath has become monotonically negative. 29

2.8 (a) The potential as a function of height above the lunar surface for $1 < T_{ph} < 10$ eV with $T_{sw} = 10$ eV. (b) The potential as a function of height above the lunar surface for $10 < T_{sw} < 100$ eV for $T_{ph} = 2.2$ eV. 31

2.9 The equilibrium grain potential for both the Maxwellian and lunar cases. Depicted on the right axis is the equilibrium charge for a 0.02 μm grain. 33

2.10 The ratio of the electric to gravitational force for a 0.02 μm grain for both the Maxwellian and lunar cases. The Maxwellian grain has an equilibrium at $z \approx 8.5$ m while the lunar grain has an equilibrium at $z \approx 2.5$ m. The line, $F_e/F_g = 1$ is shown for visual aid. 35

2.11 The equilibrium levitation height as a function of particle radius is shown for both the Maxwellian and lunar sheaths. For the Maxwellian case, particles with radii, $r > 0.072$ μm, cannot be stably levitated in the sheath, while for the lunar sheath, this limit drops to $r > 0.04$ μm. 35

2.12 The equilibrium grain potential and charge for a 0.02 μm grain as a function of height above the lunar surface for the solar minimum, solar maximum and solar flare conditions. Increased photoemission leads to a greater equilibrium grain potential and charge. 36

2.13 The ratio of the electric and gravitation forces for a 0.02 μm grain is shown as a function of height above the lunar surface for the solar minimum, solar maximum and solar flare conditions. Increased photoemission causes a higher sheath electric field and higher grain charge, leading to an increased ability to levitate dust grains on the lunar surface. 37

2.14 The equilibrium levitation height is shown as a function of particle radius for solar minimum, solar maximum and flare conditions. The increased photoemission current increases the maximum possible levitation grain radius from 0.04 μm at solar minimum to 0.075 μm and 0.12 μm for solar maximum and flare conditions, respectively. 38

2.15 The position, velocity and charge for a 0.02 μm grain, with initial position, $x_o = 0$, initial velocity, $v_o = 3$ m/s and initial charge, $q_o = 1$ e. Discrete jumps in the grain position and velocity are due to the collection or loss of a single electron. 40

2.16 The potential above a lunar crater for three cases of the solar wind / UV incidence: (a) 0°; (b) 45°; (c) 90°. 45

2.17 The surface potential as a function of horizontal distance along the crater surface (shown in Figure 2.16) for solar zenith angles ranging from 0° to 90°. As the sun sets, the leeward side of the crater (approximately $0 < x < 3$ m), becomes increasingly negative. For large values of the solar zenith angle ($\alpha > 75°$), the entire surface potential rapidly becomes negative. 47

3.1 The existence of monotonic and non-monotonic potential structures in the T_{sw}-T_{ph} phasespace for typical lunar values of the other parameters ($n_{ph} = 1.3 \times 10^8$ m^{-3}, $n_{sw} = 10^7$ m^{-3}, $M \approx 3$). 52

3.2 A comparison of simulation and theoretical results of the surface potential, V_o, the minimum potential, V_m, and the non-monotonic potential drop, $V_o - V_m$, versus the solar wind temperature, T_{sw}. 53

3.3 A comparison of simulation and theoretical results for the surface potential as a function of the photoelectron temperature, T_{ph}. The theory predicts simultaneous solutions for both monotonic and non-monotonic potentials for $T_{ph} < 3$ eV, while the simulation results predict non-monotonic potentials only for $T_{ph} < 6$ eV. 54

3.4 A comparison of the Maxwellian and κ-distributions for various values of κ. 56

3.5 The hypergeometric function of the second kind, ${}_2F_1[0.5, 2.0; 1.5; x]$, for $-1 < x < 1$. 61

3.6 The ratio of the κ-dependent surface potential to the Maxwellian surface potential, $V_o(\kappa)/V_o(maxwell)$, as a function of κ. Decreasing the κ value yields a larger high energy tail of incoming solar wind electrons and correspondingly lowers the surface potential. 69

3.7 The surface and minimum potentials as a function of κ for solar wind temperatures, $10 < T_{sw} < 50$ eV. Black lines represent $T_{sw} = 10$ eV while red lines represent $T_{sw} = 50$ eV. 72

4.1 The average lunar surface potential as measured by the Lunar Prospector MAG/ER instrument. From *Halekas et al.* [2005a]. 77

4.2 Data from Lunar Prospector during a passage through the terrestrial current sheet in April, 1999. The panels show the calculated spacecraft potential, ambient electron density, electron temperature, electron current to the lunar surface, inferred lunar surface potential and sunlight/shadow flag. From *Halekas et al.* [2008c]. 79

4.3 Lunar Prospector orbit in the terrestrial magnetotail during a series of plasmasheet passages on March 1, 1999, showing the magnetic field at LP [nT], the plasma sheet electron temperature [eV], electron differential energy flux [eV/(cm^2 sr s eV)] in five different pitch angle channels (0-30°, 30-60°, 60-120°, 120-150°, 150-180°), sun/shadow color bar, 'Sun' (blue = sun, black = shadow), magnetic connection to surface, 'Pol' (assuming no field curvature, red = positive connection, black = negative connection, white = no connection), and solar zenith angle (SZA) of connection to surface. Lunar Prospector observes an upward-going electron beam during this time period whenever magnetically connected to the surface, in both sunlight and shadow. 81

4.4 Energy pitch angle spectrogram at 22:40:10 on March 1, 1999, shown in units of electron differential energy flux [eV/(cm^2 sr s eV)]. Counts from scattered photons and internally produced photoelectrons have been approximately subtracted, as described in the text. Some residual background counts may remain at energies above 1000 eV in the upward-going pitch angles. The upward-going beam is seen in the loss cone at energies of ∼200-500 eV and pitch angles of 0-45°. 83

4.5 The potential as a function of height above the lunar surface for plasma sheet conditions ($T_{ps} = 500$ eV) for varying values of the plasma sheet ion temperature with $m_i/m_e = 100$. 84

4.6 The potential as a function of height above the lunar surface from the simulations for five different cases (solid lines) of the plasma sheet electron temperature, T_{ps}. Additionally, the potential for the $T_{ps} = 350$ eV case is also shown (dashed line). . . 85

4.7 The differential energy distribution of escaping photoelectrons (blue curve), reflected (upward-traveling) plasma sheet electrons (red curve), the sum of photoelectrons and reflected plasma sheet electrons (black curve), and LP ER measurements (dashed line), all normalized by the downward-traveling plasma sheet electron differential energy distribution, from the simulation with T_{ps} = 350 eV. LP-measured fluxes greater than 500 eV are most likely due to remaining noise contamination. 87

4.8 The median electron distribution for LP observations above the dayside lunar surface in the solar wind, categorized into: (a) "None", those with no upward going enhancement, (b) "Conic", those with an upward conic pitch angle distribution, and (c) "Beam", those with a upward field-aligned beam distribution. The top panel shows the unnormalized distribution and the bottom panel shows the distribution normalized by the median downward electron distribution for all observations. 90

4.9 The frequency distribution of measurements of the ratio of secondary to primary electron currents above the lunar nightside made by the Lunar Prospector Electron Reflectometer. The dashed line shows the median value while the solid line shows the value approximately consistent with laboratory measurements. From *Halekas et al.* [2009a]. 91

4.10 A picture of the ARTEMIS spacecraft. From *Angelopoulos* [2010]. 92

Chapter 1

Introduction and Previous Work

1.1 The Lunar Plasma Environment

The plasma environment on the Moon is shaped by a combination of processes that vary as it orbits the Earth, many of which are depicted graphically in Figure 1.1. On the sunlit side of the Moon, photoelectric charging due to solar ultraviolet (UV) radiation and the collection of solar wind ions and electrons from the solar wind or terrestrial magnetotail dominate the creation of the lunar plasma environment. On the night-side of the Moon, the surface is exposed to the tenuous, yet hot, plasma environment of the lunar wake. Other processes, such as secondary electron emission, pick-up ions and surface remanent magnetic fields further enrich the lunar plasma environment. While the Moon spends a majority of its time in the solar wind, it also traverses the terrestrial magnetosphere, including the magnetosheath, the tail lobes and occasionally the plasma sheet during each lunation. The differing characteristics of these external plasma sources result in significant changes in the near-surface lunar plasma environment.

The interaction of the incoming solar wind (or other external plasma) with the UV-generated photoelectrons from the surface generates a complex and dynamic photoelectron sheath immediately above the lunar surface. The photoemission current on the dayside is greater than the current collected from the solar wind and therefore the sunlit lunar surface is expected to charge positively. The photoelectron sheath accelerates electrons towards the moon while retarding ions, shown in Figure 1.2. Previous work has derived theoretical expressions for the potential and electron density above a photoemitting surface [*Guernsey and Fu*, 1970; *Grard and Tunaley*, 1971; *Walbridge*,

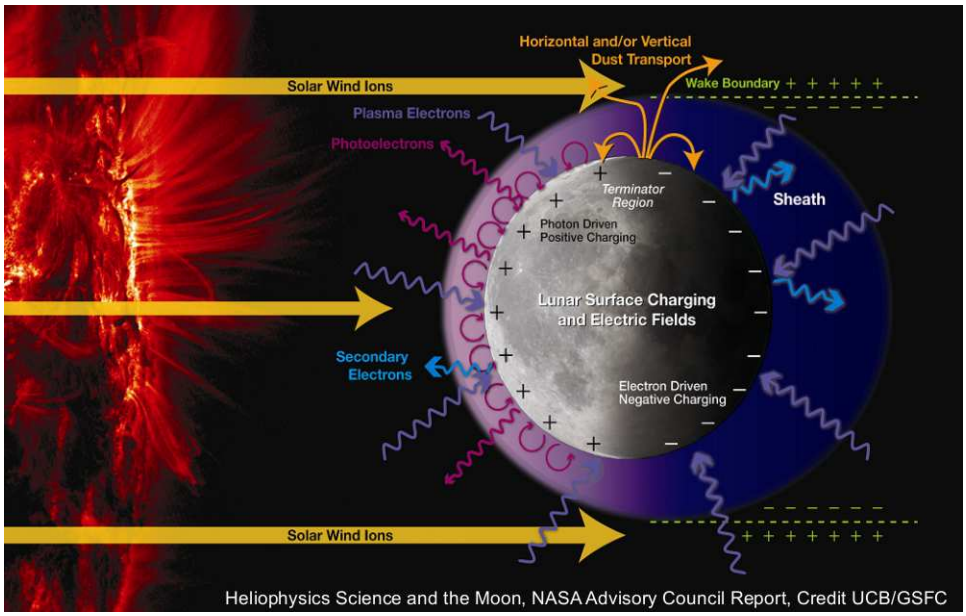

Figure 1.1: A graphic overview of the lunar plasma environment, showing the presence of solar UV radiation, incoming solar wind electrons and ions, and impact-generated secondary electrons. Also denoted is the possible presence of lunar dust dynamics near the terminator region. [*NAC / GSFC / UCB*]

1973] for an assumed Maxwellian energy distribution for the emitted photoelectrons. However, the emitted photoelectron energy distribution for the lunar surface differs from a Maxwellian distribution since it is dependent on the incoming solar UV flux, the lunar dust work function and the photoelectric yield function [*Feuerbacher et al.*, 1972; *Sternovsky et al.*, 2008]. Additionally, the solar wind alters the extent and nature of the photoelectron sheath by providing a flux of ions and electrons to the surface. While previous work has modeled the plasma environment above the lunar surface [*Freeman and Ibrahim*, 1975; *De and Criswell*, 1977; *Criswell and De*, 1977; *Nitter et al.*, 1998; *Borisov and Mall*, 2006; *Farrell et al.*, 2007], a study combining the effects of the distinct lunar photoelectron distribution and the inflowing solar wind flux has not yet been undertaken, until now.

The Apollo-era yielded some of the first direct measurements of the lunar plasma environment and today, form the basis of our understanding of the near-surface plasma properties. The Apollo 12, 14, 15 and 17 missions left a variety of instruments on the surface, including the Suprathermal

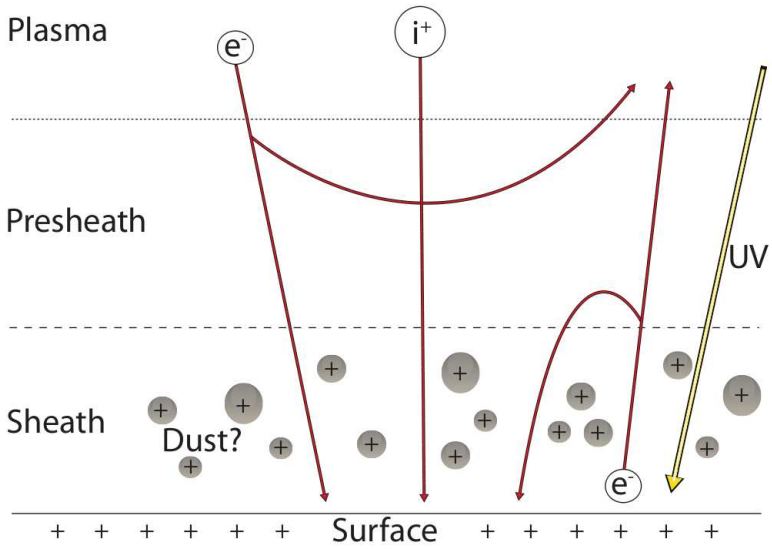

Figure 1.2: A graphic of the plasma environment on the day-side of the lunar surface. Photoelectrons generated by UV illumination are emitted from the surface and solar wind electrons and ions impinge on the surface. The presence of a non-monotonic potential would reflect some solar wind electrons back to space while trapping some photoelectrons near the surface. [Courtesy: A. Shinn]

Ion Detector (SIDE, Apollo 14 and 15) [*Freeman et al.*, 1970, 1972], the Charged Particle Lunar Environment Experiment (CPLEE, Apollo 14) [*O'Brien and Reasoner*, 1971], the Solar Wind Spectrometer (SWS, Apollo 12 and 15) [*Neugebauer et al.*, 1972] and the Lunar Ejecta and Meteorites Experiment (LEAM, Apollo 17) [*Berg et al.*, 1973, 1974]. The measurements made by these instruments confirmed the basic view of the lunar surface plasma environment as dominated in sunlight by the UV-generated photoelectron sheath. For example, the CPLEE instrument measured a complete drop-out of electrons during a total lunar eclipse, shown in Figure 1.3, confirming that the plasma environment on the day-side lunar surface is dominated by photoelectrons [*Reasoner and Burke*, 1972a,b]. Variations in the plasma environment are seen by CPLEE when the Moon is alternately in the solar wind, the terrestrial magnetotail or the terrestrial plasma sheet [*Reasoner and Burke*, 1972a; *Rich et al.*, 1973].

Modeling of the lunar near-surface (< 1 km) plasma environment has become an important component of understanding the lunar dusty plasma environment. While initial views of the surface plasma environment were relatively simple, recent work has shown the near-surface plasma envi-

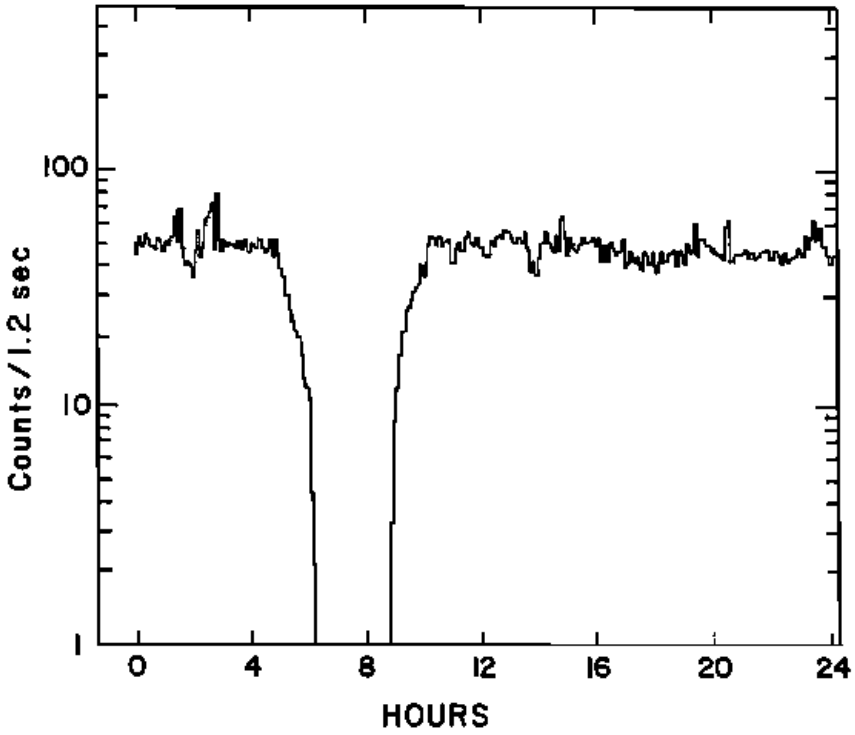

Figure 1.3: The count rate of electrons measured by the Apollo 14 CPLEE instrument during a solar eclipse. As the lunar surface fell into shadow, UV-stimulated photoemission ceased, resulting in a complete drop-out of electrons. This measurement confirms that CPLEE was measuring photoelectrons from the surface. From *Reasoner and Burke* [1972a].

ronment to be complex and dynamic [*Freeman and Ibrahim*, 1975; *De and Criswell*, 1977; *Criswell and De*, 1977; *Nitter et al.*, 1998; *Borisov and Mall*, 2006; *Farrell et al.*, 2007]. One of the key areas of interest is the lunar terminator, where boundaries between sunlit and shadowed regions can alter the near-surface plasma environment. Photoelectrons are emitted from sunlit patches and can return to the lunar surface in either a sunlit or a shadowed patch. While photoelectrons that return to a sunlit patch simply represent a return current, photoelectrons that return to the surface in a shadowed patch cannot conduct to a sunlit patch due to the extremely high resistivity of the lunar regolith [*Olhoeft et al.*, 1974]. It has been suggested that such boundaries on the lunar surface could lead to extremely large electric fields ($> 10^5$ V/m) [*De and Criswell*, 1977; *Criswell and De*, 1977]; however, this work did not consider the neutralizing return current of the solar wind electrons, which would decrease any large potential differences. To date, no direct measure-

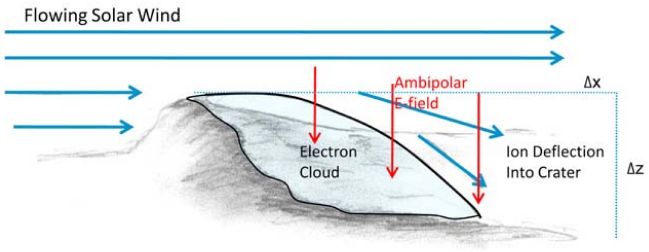

Figure 1.4: A schematic of the near-surface plasma environment near an obstacle, such as a boulder or crater rim. While the solar wind electrons easily penetrate into the region just behind the obstacle, the ions cannot respond as fast and thereby set up an ambipolar electric field. The field eventually pulls the ions down and into the 'mini-wake'; however, there may exist a stable electron cloud immediately behind the obstacle. From *Farrell et al.* [2010].

ments of such strong electric fields in the terminator region have been made, leaving the question of 'supercharging' an open one.

Additional work has focused on the effect that non-trivial topography on the lunar surface may have on the near-surface plasma environment [*Farrell et al.*, 2007, 2010]. As the solar wind convects past the terminator region of the lunar surface, solar wind shadowing by complex topography, including boulders and crater rims, may generate 'mini-wakes' behind them. While the solar wind electrons penetrate into the shadowed regions behind the obstacle relatively easily due to their high thermal velocity, solar wind ions cannot immediately follow the electrons due to their higher mass and correspondingly lower thermal speed (in addition to their convective velocity). The difference in diffusion rates between the electrons and the ions results in a net charge separation and correspondingly sets up an ambipolar electric field pointing into the mini-wake. Eventually, the ions are deflected into the mini-wake region; however, there may exist a stable region of net negative charge immediately behind the obstacle. Such a charge separation could lead to the generation of electric field strengths above the nominal photoelectron sheath electric field strengths ($\approx 1 - 5$ V/m) and contribute to enhanced dust transport near obstacles and the terminator region. Figure 1.4 depicts the processes that may be in effect immediately behind an obstacle on the lunar surface at the terminator, including an electron cloud and an ambipolar electric field [*Farrell et al.*, 2010].

Laboratory measurements have investigated the concept of supercharging by measuring the

potential horizontally above a series of differentially illuminated plates [*Wang et al.*, 2007b]. The experiment showed that differential illumination can lead to horizontal electric fields that are orders of magnitude larger than the associated vertical fields. Additionally, the illumination was allowed to change over time in order to simulate moving shadows from obstacles on the lunar surface, and it was found that time-dependent illumination could further enhance the horizontal potential gradient across the plates. While this experiment demonstrated the concept of supercharging due to differential illumination in the laboratory, it remains to be seen if a similar effect is present *in-situ*. Specifically, the presence of the neutralizing background solar wind electrons would tend to short out any significant potential gradients that might arise near sunlit-shadowed boundaries. One situation that is worth further investigation is the role that the solar wind ion aberration (on the order of 4°) may play a role in allowing narrow regions of the lunar surface to experience larger potential gradients than other regions.

1.1.1 Plasma Environments around other Airless Bodies

Studying the plasma interaction with the Moon can serve as an important analogue for a variety of airless bodies throughout the solar system. These range from kilometer-scale asteroids to the major moons of Jupiter and Saturn. Solar UV-induced photoemission is a critical physical mechanism at any body without a significant atmosphere, similar to the Moon. Asteroids represent the most direct comparison to the Moon, lacking both an atmosphere and a global magnetic field. Since the Moon and asteroids are larger than the Debye length in the solar wind ($\approx$ 10 m), both fall into the same category with respect to basic plasma interactions. One would expect similar charging profiles on asteroids (positive dayside potentials transitioning to larger, negative potentials on the nightside) as well as the generation of a plasma wake behind the asteroid.

Bodies with similar, yet slightly different environments include Mercury and the satellites of the giant planets. The Mercurian environment is dominated by the presence of a global magnetic field, which shields the surface to some degree from the intense solar wind [*Grard*, 1997; *Grard et al.*, 1999]; however, the lack of an atmosphere means that solar UV radiation will stimulate large

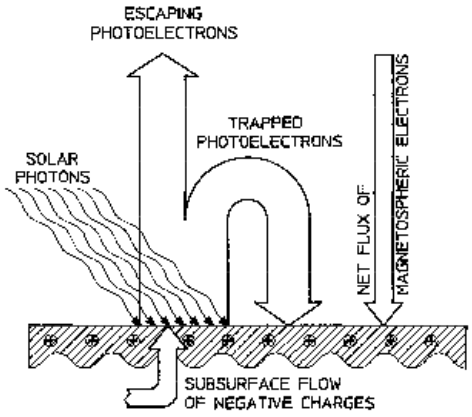

Figure 1.5: A schematic of the Mercurian near-surface plasma environment, including solar UV radiation, trapped and escaping photoelectrons and incoming magnetospheric electrons. From *Grard* [1997].

amounts of photoemission from the surface. Additionally, while the global magnetic field will shield some areas of the surface from incoming magnetospheric electrons, other regions will be subjected to intense magnetospheric currents via cusp regions. Figure 1.5 shows a schematic of the near-surface Mercurian plasma environment, showing solar UV radiation, trapped (both magnetically and electrostatically) and escaping photoelectrons and incoming magnetospheric electrons [*Grard*, 1997].

Another set of bodies that bear similarity to the Moon are some of the satellites of the giant planets. For satellites that do not have appreciable surface conductivity and are not geologically active (ie. Rhea, Tethys, Dione), the interaction between the satellite surface and the ambient magnetospheric plasma environment can resemble that of the Moon. At the heliocentric distances of Jupiter and beyond, the photoemission current is reduced from the terrestrial value by r_h^{-2}, where r_h is the heliocentric distance of the satellite in AU; however, this current, in addition to secondary electron emission, still plays a critical role in shaping the plasma environment. As the satellite progresses in its orbit about the planet, the angle between the UV incidence and the magnetospheric plasma incidence rotates through 360°, exposing the satellite's surface to a wide range of plasma inputs. Recent work has used current-balance equations to explore the longitudinal dependence of the surface potential and electric field of the satellites of Saturn [*Roussos et al.*, 2010]

with results that are qualitatively similar to the Moon. Figure 1.6 shows a schematic of the various plasma environments that a Saturnian satellite would be exposed to as it orbited the planet. Recent fly-bys of the Saturnian satellite Rhea by the Cassini spacecraft have yielded measurements of the plasma environment near the surface, which can be used to validate models of surface charging.

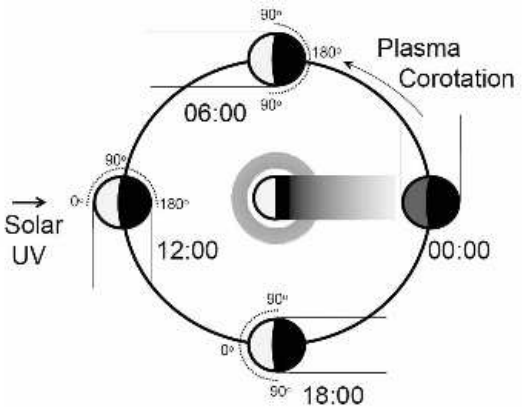

Figure 1.6: A schematic of the various plasma environments that a Saturnian moon would be exposed to as it orbits Saturn. The solar UV flux is from a constant direction while the magnetospheric co-rotation flow is constantly swept through different angles with respect to the UV incidence. From *Roussos et al.* [2010].

1.2 The Lunar Dust Environment

Micron and sub-micron sized dust grains from the lunar regolith are present in, and can alter the nature of, the lunar photoelectron sheath. These grains charge via photoemission and the collection of electrons and ions, and change the local plasma environment. *In-situ* experimental evidence suggests that lunar dust grains can be mobilized and transported above the lunar surface [*Criswell*, 1972; *Rennilson and Criswell*, 1974; *Berg et al.*, 1974; *Zook and McCoy*, 1991]. While originally designed to measure the bombardment rate of interplanetary dust, the Lunar Ejecta and Meteorites experiment (LEAM), deployed by the Apollo 17 astronauts, recorded evidence of slowly moving, highly charged lunar dust moving across the lunar surface near the terminators [*Berg et al.*, 1974]. Since the instrument was not designed to measure this type of dynamics, it was not able to constrain the size, velocity and charge of the transported grains. Therefore, it

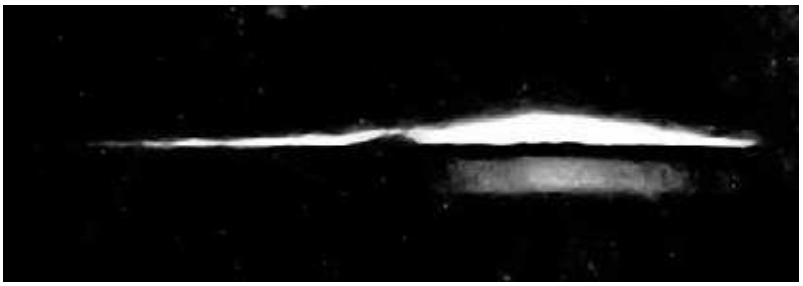

Figure 1.7: An image taken by the Surveyor 7 camera showing lunar horizon glow shortly after sunset (upper glow). The lower glow is the reflection of the primary horizon glow off of the lunar surface [*Colwell et al.*, 2007].

remains an open question as to whether the grains were transported horizontally large distances while electrostatically levitated above the surface, or if the grains made a series of small 'hops'. Nevertheless, the LEAM measurements are perhaps the most concrete indication of lunar dust dynamics on the surface.

An additional piece of *in-situ* evidence for near-surface dust dynamics comes from the video cameras aboard the Surveyor 5, 6 and 7 spacecraft, which recorded images of lunar 'horizon glow' just after sunset. The horizon glow was characterized by a thin band of brightness seen immediately above the lunar surface, in excess of what the coronal-zodiacal light would contribute [*Criswell*, 1972; *Rennilson and Criswell*, 1974]. Figure 1.7 shows an image of lunar horizon glow taken by the Surveyor 7 spacecraft [*Colwell et al.*, 2007]. Best fits using scattering theory yielded average dust grain sizes of approximately 5 μm at heights of approximately 30 cm [*Criswell*, 1972]. The levitation height is similar to the local Debye length (and sheath thickness) which suggested that the grains were levitated (either stably or ballistically) above the lunar surface. Lunar surface supercharging, as discussed in Section 1.1, was cited as a possible explanation for the observed motion of these dust grains [*Rennilson and Criswell*, 1974; *Wang et al.*, 2007b]; however, this is not yet confirmed.

Other *in-situ* measurements of lunar dust dynamics come from observations made by the Apollo astronauts while at the Moon [*Zook and McCoy*, 1991]. During their time spent orbiting the Moon, the Apollo 15, 16 and 17 astronauts took a series of photographs of the coronal-zodiacal

light (CZL). These measurements would improve upon their terrestrial counterparts by eliminating the presence of any atmospheric effects, which complicate the analysis when observed from Earth. A recent re-analysis of these photographs using updated Mie-scattering retrievals was undertaken to verify previous models of lunar exospheric dust concentration [*McCoy*, 1976; *Glenar et al.*, 2011]. Images from Apollo 15 and 17 were shown to contain the unambiguous presence of lunar horizon glow due to light scattering by sub-micron sized dust grains; however, the mechanism by which these grains might be ejected from the lunar surface remains unclear. The authors suggested that episodic meteor streams may trigger a 'dust cascade' by providing an initial source of ejected grains which then re-impact the lunar surface and dislodge further grains. Verification of this or other possible theories may come with the Lunar Atmospheric and Dust Environment Explorer (LADEE) mission, which is slated to launch in early-2013 and take measurements of the lunar dust exosphere from orbit, both via photography and *in-situ* dust detection.

As the astronauts were engaged in the photographic campaign, they also sketched several additional unanticipated features. Figure 1.8 shows a series of sketches by the Apollo 17 Commander, E. Cernan, of observations made approaching sunrise above the Moon (as viewed from the Apollo Command Module (CM), which in a retrograde orbit would have orbital sunrise above the lunar sunset terminator). The main two additional features observed were a shoulder on the main CZL bulge and a series of time-dependent 'streamers' that varied rapidly as the CM approached sunrise. These sketches have generated considerable discussion regarding their origin and possible dynamics. Calculations using dimensions and brightnesses of the CZL shoulders estimated from the Apollo sketches have ruled out lunar gas as the source and strongly suggested scattering by micron and sub-micron sized dust grains [*Zook and McCoy*, 1991]. The streamers were not analyzed quantitatively by the authors, but provide qualitative evidence of dust dynamics above the lunar terminator.

Laboratory experiments have demonstrated the ability to charge and transport micron-sized dust grains in a plasma environment [*Walch et al.*, 1994, 1995; *Horányi et al.*, 1995, 1998; *Sickafoose et al.*, 2000, 2001, 2002; *Robertson et al.*, 2003; *Flanagan and Goree*, 2006; *Wang et al.*,

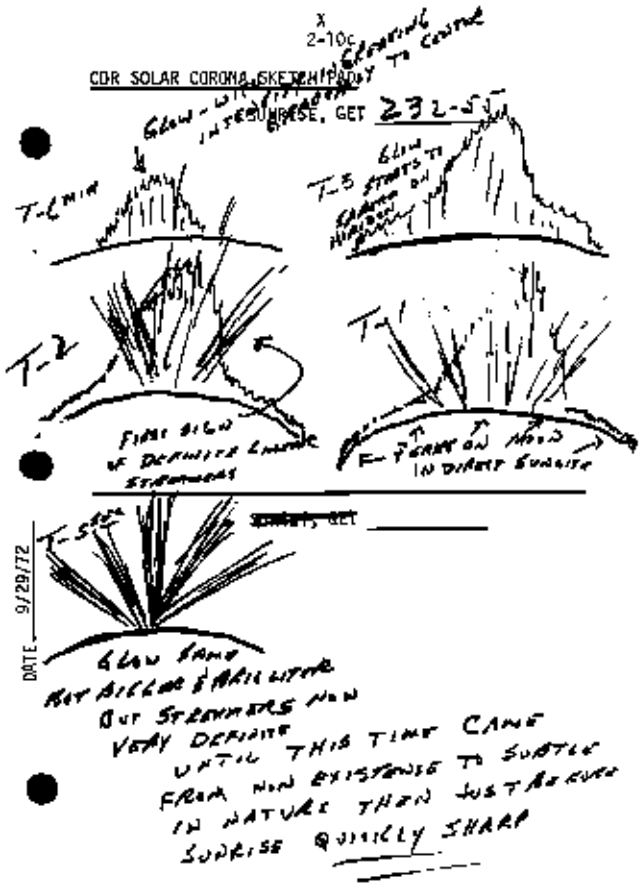

Figure 1.8: A series of sketches by Apollo 17 Commander E. Cernan of the coronal-zodiacal light (CZL) and two additional, unexpected features: the shoulders on the main CZL bulge and several, time-dependent 'streamers' [*Zook and McCoy*, 1991].

2007a, 2009, 2010, 2011]. Initial experiments focused on the charging mechanisms of both lunar and simulant dust grains in a plasma, and found charging in agreement with orbit-motion-limited charging theory [*Walch et al.*, 1994, 1995; *Horányi et al.*, 1995; *Horányi*, 1996; *Horányi et al.*, 1998]. The next two studies characterized a wider range of dust grain charging mechanisms present in space environments, including photoemission, electron and ion collection, secondary emission and tribo-electric charging [*Sickafoose et al.*, 2000, 2001]. These experiments again confirmed standard charging theories of dust grains [*Horányi*, 1996] and also yielded support for lunar dust transport theories. An additional experimental study analyzed the ability to electrostatically levitate charged dust grains above a biased plate immersed in a low-density plasma [*Sickafoose et al.*, 2002]. While

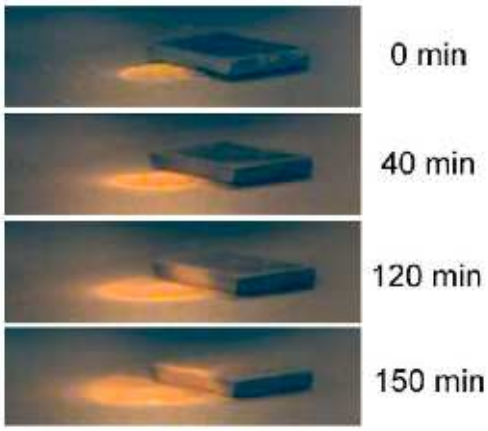

Figure 1.9: A series of images taken a successive times of a dust grain pile exposed to a plasma. Over time, the pile electrostatically spreads out as dust grains charge and are transported horizontally. Additionally, dust grain accumulation on the sides and the top of the insulating rubber block show that the grain movement includes vertical 'hops' in addition to horizontal transport [*Wang et al.*, 2010].

the plasma parameters and plate bias were different from those found at the lunar surface, the confirmation of the ability to levitate grains in a plasma sheath represents additional support for lunar dust grain levitation theories.

Further experimental work focused on the ability to electrostatically levitate dust grains when grouped in aggregate, rather than as single particles. Using a similar laboratory setup to previous experiments [*Sickafoose et al.*, 2001, 2002], a dust grain pile, comprising millions of individual dust grains, was laid on a graphite plate and exposed to either a background ambient plasma or an energetic electron beam [*Wang et al.*, 2009, 2010]. Under the influence of both vertical and horizontal electric fields, the dust grain piles were observed to spread outwards radially. Figure 1.9 shows an example of this transport mechanism as a time-series of photographs of the dust pile [*Wang et al.*, 2010]. As seen in the pictures, the dust grains are transported radially and vertically, as evidenced by the placement of dust grains on the side and top of a nearby insulating block. Such transport was only seen to happen after the introduction of plasma into the chamber, demonstrating that the motion was electrostatically induced.

Although previous work has addressed both the required conditions and subsequent dynamics

of electrostatically charged lunar dust grains in a variety of environments [*Nitter and Havnes*, 1992; *Nitter et al.*, 1994, 1998; *Borisov and Mall*, 2006; *Stubbs et al.*, 2006], these processes are not yet fully understood for the lunar surface. Typically, a photoelectron sheath model is assumed or calculated, allowing both the electric field above the surface and the grain charging characteristics to be calculated. For example, dust grains on the dayside of the Moon should typically charge positively due to photoemission, while on the night side, in the absence of photoemission, grains charge negatively. The positive grains on the dayside would typically feel an upward electric force from the photoelectron sheath and for certain values of the charge, grain size and electric field, levitation and/or transport can result. Two significant areas of uncertainty throughout these theories are (a) the exact nature of the near-surface plasma environment and (b) the microphysics of grain charging and cohesion on the lunar surface. Theoretical derivations can provide a reasonable estimate for photoelectron sheath plasma properties on the dayside; however, open questions about the near-surface plasma environment include the presence of non-montonic potentials, the role of remanent crustal magnetic fields and the impact of topography on the plasma environment. The initial conditions of surface dust grains, including their charge state and ejection mechanism(s), also remains poorly understood. Careful application of Gauss' Law to the surface would suggest that micron and sub-micron sized dust grains are almost all uncharged, with only a few grains having a single electron. For example, the typical electric field strength, E, near the sub-solar point is approximate 5 V/m, which, using the relation,

$$E = \sigma/\epsilon_o, \tag{1.1}$$

where σ is the surface charge density and ϵ_o is the permittivity of free space, gives a surface charge density of approximately $\sigma = 3 \times 10^8$ e m^{-2}. If we approximate the surface as being comprised of only 1.0 μm sized grains, (meaning that there are approximately 10^{12} such grains per square meter), then there is a factor of ten more grains than free charges. This picture is most likely overly simplistic, in that the electrostatics on the micron scale, including the dielectric and angular nature of the grains, may allow for larger charge states and electric fields than predicted on the

macro scale. In sum, while recent work has begun to refine our understanding of the charging and dynamics of micron-sized lunar dust grains, there remains significant uncertainty with regards to key electrostatic properties of the lunar dusty plasma environment.

1.2.1 Dust on Other Bodies

Electrostatic dust transport has also been suggested to be present on other airless bodies or structures, including Mercury, 433 Eros and the rings of Saturn [*Hill and Mendis*, 1981; *Ip*, 1986; *Colwell et al.*, 2005]. While Mercury's plasma environment is distinctly different from that of the Moon due to its global magnetic field and proximity to the Sun, the lack of an atmosphere remains as a key factor in the possibility of dust transport [*Ip*, 1986]. Observations by the NEAR spacecraft of smooth deposits of dust in the bottom of several craters on the surface of 433 Eros, termed 'dust ponds', yielded several theories involving the preferential transport of micron-sized dust grains into craters [Veverka *et al.*, 2001; *Robinson et al.*, 2001; *Cheng et al.*, 2002; *Colwell et al.*, 2005; *Hughes et al.*, 2008]. Figure 1.10 shows an image taken by the NEAR spacecraft of a series of dust ponds of various sizes. These ponds are thought to form as electrostatically charged dust is transported into the crater, perhaps during terminator crossings [*Hughes et al.*, 2008]. The lack of observations of such ponds on the Moon could be explained by either observational bias or by differing geophysical parameters; however, the mechanism for the ponds is as-of-yet unexplained.

1.3 Scientific Motivation and Thesis Outline

The study of the lunar dusty plasma environment is motivated by the investigation of basic plasma physics on the lunar surface, the role of dust grains in modifying this environment and the impact that these grains can have on robotic and human exploration of the lunar surface. A study of the Moon-plasma interaction can yield information not only about our nearest cosmic neighbor, but can also elucidate the environment in several corners of the solar system, from Mercury to the moons of the giant planets. This thesis is presented in three main sections:

(1) Chapter 2: Simulation of the near-surface plasma and dust environment via particle-in-cell

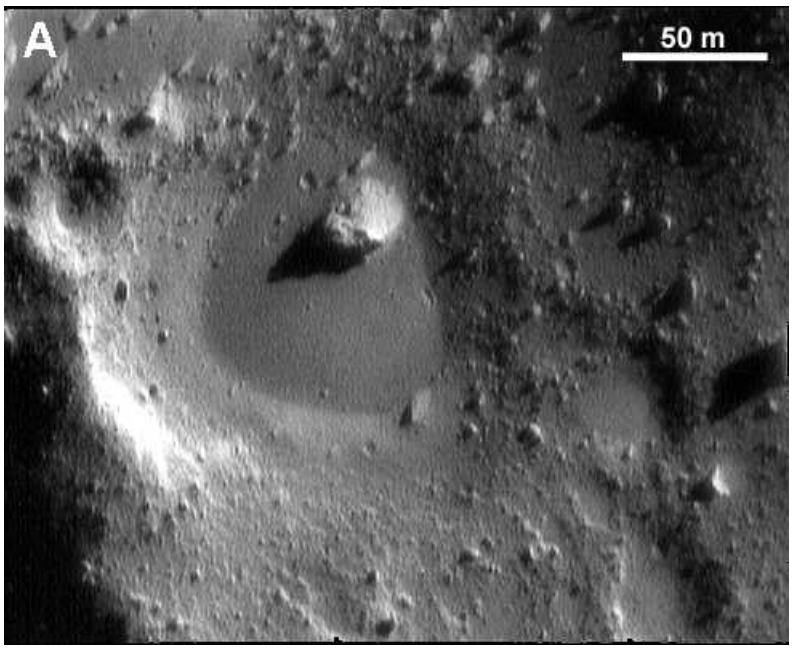

Figure 1.10: An image of several dust ponds on the surface of 433 Eros, taken by the NEAR spacecraft during closest approach in 2001 [*Robinson et al.*, 2001].

and test-particle codes. A one-dimensional particle-in-cell model explores the fundamental plasma physics of the interaction of the lunar photoelectron sheath with an ambient plasma (solar wind, terrestrial plasma sheet, etc.), and finds that in nearly all cases of the model parameters (photoelectron temperature, solar wind temperature, solar wind density, etc.), a non-monotonic sheath potential is present above the lunar surface. To stably maintain the non-monotonic potential, a layer of space charge forms immediately above the lunar surface, effectively shielding the surface photoelectrons from the ambient plasma. A range of model results provides the input (in terms of potential, electric field and particle densities) for the study the charging and dynamics of micron and sub-micron sized dust grains in the lunar plasma environment via a test-particle approach. The models predicts limits on the ability of the photoelectron sheath to levitate and transport dust grains above the lunar surface. Additionally, preliminary work on modeling the effect of surface topography on the lunar near-surface plasma environment with a three-dimensional PIC code, VORPAL, is shown. The initial model results show that relatively simple surface relief creates complex potentials and electric fields that may contribute to the ability to transport dust grains beyond the predictions of the one-dimensional results.

(2) Chapter 3: Comparison of the particle-in-cell results of the lunar photoelectron sheath to a theoretical, kinetic derivation. The code is initially compared to previous analytical work that describes the potential and density distributions above a photoemitting plate in the absence of an ambient plasma and good agreement is found. Theoretical work that builds on previous work by including the presence of a Maxwellian solar wind and a streaming solar wind ion beam is briefly described and compared to relevant PIC results. Again, good agreement is found, not only validating the PIC code, but also lending support to

the hypothesis that non-monotonic potentials have lower electrostatic energy than their monotonic counterparts, and thus, represent the more stable state. Finally, we extend the theoretical derivation for a photoemitting surface in an ambient plasma to include a κ-distribution for the ambient plasma. Kappa distributions have a larger high-energy tail compared to an equivalent Maxwellian distribution and are present in a wide variety of space plasma environments.

(3) Chapter 4: Comparison of the particle-in-cell results to *in-situ* measurements of the lunar plasma environment by the Lunar Prospector (LP) spacecraft. The Lunar Prospector spacecraft has measured several characteristics of the lunar plasma environment through the use of electron reflectometry and these measurements can reveal the nature of the near-surface ($z < 1$ km) lunar plasma environment. Electron reflectometry exploits the magnetic mirror effect to determine the surface remanent magnetic field strength and the surface potential with respect to the solar wind. Typically, the surface potential measurements correspond well to simple point-wise current balance calculations; however, some measurements in the terrestrial plasma sheet show "anomalous" negative surface charging, in which the daylit lunar surface appears to be hundreds of volts negative when point-wise theory would predict a positive potential less than 10 V. We compare the LP measurements with complementary model runs and show that the apparent negative surface charging is due to the presence of large (hundreds of volts), stable non-monotonic potentials above the lunar surface. Future data analysis, including LP measurements of the lunar surface potential in the solar wind, higher resolution ARTEMIS measurements of the plasma environment, and LADEE measurements of the dust environment are discussed.

The results presented in this thesis have advanced the understanding of the lunar plasma environment and its role as a 'natural dusty plasma physics laboratory'. The results are shown not only to be relevant to the Moon, but also to numerous bodies throughout the solar system. As with any scientific investigation, new understanding generates new questions, new areas to explore and further applications which are discussed specifically in each chapter.

Chapter 2

Particle-in-Cell Photoelectron Sheath Simulations

2.1 One-dimensional PIC Simulations

In order to simulate the lunar surface plasma environment, a one-dimensional electrostatic particle-in-cell (PIC) code has been developed, following the general outline established in *Birdsall and Langdon* [1985]. Briefly, a PIC code models a plasma environment by advancing plasma "macroparticles" in time, using Poisson's equation to calculate the electric potential and Newton's equation to advance the macroparticle spatially. The macroparticles are simulation particles that represent a large number of physical particles (ie., electrons, ions) and are used to reduce the computational work-load of the simulation, which would be unable to process the large number of physical particles in any given situation. For example, macroparticles in the PIC code described here typically represent between 10^4 and 10^6 physical particles, depending on the specific parameters chosen. An additional feature of a PIC code is the use of a discrete spatial grid, on which the charge density, ρ, electric potential, ϕ, and electric field, E, are calculated. This vastly simplifies the number of calculations needed to run the simulation. Transformation between values needed at the grid points (ρ, ϕ, E) and values needed at the particles (force, F, position, x, velocity, v) are done by weighting the particle to its nearest grid points.

To advance the simulation in time, a set of calculations are iteratively solved, in the following order:

(1) The charge density is calculated from the macroparticle positions;

(2) Poisson's equation ($\nabla^2\phi = -\rho/\epsilon_o$) is solved for the electric potential, ϕ, from the charge density, ρ on the grid;

(3) The electric field is calculated from the potential on the grid;

(4) The force on each macroparticle is calculated from the electric field;

(5) The macroparticles are advanced one timestep using the calculated force and previously known velocity.

The equations used in this computational cycle must be expressed in their finite-difference form due to the discretization of space and time. The continuous equations of motion must be transformed into finite-difference equations, as shown below:

$$F = m\frac{dv}{dt} \quad \rightarrow \quad F_{i+1} = m\frac{v_{i+1} - v_i}{\Delta t} \tag{2.1}$$

$$v = \frac{dx}{dt} \quad \rightarrow \quad v_{i+1} = \frac{x_{i+1} - x_i}{\Delta t}. \tag{2.2}$$

The timestep, Δt, must obey the Courant-Friedrichs-Lewy (CFL) condition [*Courant et al.*, 1928], which states that $c\Delta t < \Delta x$, where c is the speed of light and Δx is the simulation gridsize. While the simulation time increases as $\Delta t \rightarrow 0$, this also decreases the error associated with discretization, which scales as $(\Delta t)^2$ [*Birdsall and Langdon*, 1985]. Other equations must be transformed into their finite-difference analogues, such as the relationships between the electric field, potential and charge density,

$$E = -\nabla\phi \quad \rightarrow \quad E_j = \frac{\phi_{j-1} - \phi_{j+1}}{2\Delta x} \tag{2.3}$$

$$\nabla^2\phi = -\frac{\rho}{\epsilon_o} \quad \rightarrow \quad \frac{\phi_{j-1} - 2\phi_j + \phi_{j+1}}{(\Delta x)^2} = -\frac{\rho_j}{\epsilon_o}. \tag{2.4}$$

In Equations 2.1 through 2.4, j is the index for the grid points, while i is the index for the time step. Thus, the practice of discretizing space, when applied to the equations for the electric field and potential, transforms differential equations into simpler, algebraic equations, decreasing the computational load and increasing the speed at which the computer can step through the computational cycle.

To customize the PIC code to represent the lunar surface, the left boundary ($x = 0$) was assigned to be the photoemitting surface and ambient ions and electrons enter the simulation from the right ($x = L$). All species are absorbed upon reaching the left boundary (lunar surface) and the net surface charge is continuously calculated. While recent observations have shown that a small fraction ($\approx 1\%$) of solar wind protons may be scattered off the lunar surface rather than absorbed [Saito *et al.*, 2008], we do not include such an effect at this time. Photoelectrons that reach the right boundary are re-introduced at the right boundary as solar wind electrons in order to maintain current neutrality at the simulation boundary. All simulations are run long enough to ensure that equilibrium conditions are established. In order to resolve the sheath, the ratio of the Debye length at the surface, λ_D, to the simulation gridsize was maintained on the order of 25. The total simulation volume was approximately 85-100 λ_D for all simulations. Under nominal solar wind conditions on the lunar dayside, secondary electron emission (via either solar wind electrons or ions) does not represent a significant current [*Willis et al.*, 1973; *Whipple*, 1981] and therefore, has not been included. It is important to note that the lunar surface has a rich variety of topographic relief, as well as a complex magnetic field structure, neither of which are reproduceable in a one-dimensional code. Therefore, this model is best representative of a flat plain on the lunar surface at local noon, with either no or a normal magnetic field. Higher dimensionality codes will be able to take into account these, and many other, phenomena. Initial three-dimensional simulations are discussed further in Section 2.6.1.

2.2 Photoelectron-Only Sheath

The original work in photoelectron sheaths considered a photoemitting plate without an ambient plasma present, such as the solar wind [*Grard and Tunaley*, 1971]. For the photoelectrons, the authors considered three distributions: a monokinetic beam ($f(v) = \delta(v_o)$), a rectangular distribution ($f(v) \propto 1, v < v_o$) and a Maxwellian distribution ($f(v) \propto \exp(-v^2/v_{th}^2)$). Using Poisson's equation, electron continuity and energy conservation, the potential, electric field and photoelectron density above the surface can be calculated. The normalized electric potential above

the lunar surface for the three distributions are given by,

$$\frac{\phi - \phi_o}{\Phi_e} = \left(1 - \frac{3}{\sqrt{2}}\frac{z}{\lambda_o}\right)^{4/3} - 1 \qquad \text{[Monokinetic]} \tag{2.5}$$

$$\frac{\phi - \phi_o}{\Phi_e} = 3\left(1 - \frac{1}{3\sqrt{2}}\frac{z}{\lambda_o}\right)^{4} - 3 \qquad \text{[Rectangular]} \tag{2.6}$$

$$\frac{\phi - \phi_o}{\Phi_e} = -4\ln\left(1 + \frac{1}{\sqrt{2}}\frac{z}{\lambda_o}\right) \qquad \text{[Maxwellian]}, \tag{2.7}$$

where ϕ, ϕ_o and Φ_e are the potential, the surface potential and the potential corresponding to the mean particle velocity, respectively, and z and λ_o are the height above the surface and the sheath thickness (approximately the Debye length) [*Grard and Tunaley*, 1971]. Figures 2.1(a) and (b) show the normalized potential and electron density, respectively, as a function of the normalized height above the surface for all three distributions. For the monokinetic case, the sheath does not extend above $\sqrt{2}\lambda_o/3 \approx 0.5\lambda_o$ and for the rectangular case, the sheath extends only to $3\sqrt{2}\lambda_o \approx 4.2\lambda_o$.

While seldom would a surface in space not be immersed in an ambient plasma, the derivation still provides a useful comparison to ensure that the 1-dimensional particle-in-cell code is properly functioning. The 1-d PIC code was run without an ambient plasma for all three photoelectron distributions and compared to the theoretical expressions. Shown in Figure 2.2 is a comparison of the theoretical and simulation results for the normalized electron density above the surface for the Maxwellian case. The two curves show excellent agreement and thereby validate the simulation code. Similar agreement is seen for the rectangular distribution; however, the monokinetic distribution was seen not to agree with theory [*Grard and Tunaley*, 1971]. Upon further investigation, it was noted that a monokinetic photoelectron distribution will produce an unstable photoelectron sheath and is the basis for the virtual cathode oscillator, or "Vircator" [*Birdsall and Bridges*, 1961; *Bridges and Birdsall*, 1963; *Kadish et al.*, 1986; *Intrator et al.*, 1988]. While beyond the scope of this thesis, this field of research presents an additional application for the 1-dimensional PIC code.

2.3 Effect of the Photoelectron Energy Distribution and the Solar Wind

The photoelectron energy distribution used in the model is of particular importance, as the solar UV-induced photoelectron current is the dominant charging process for the sunlit lunar surface.

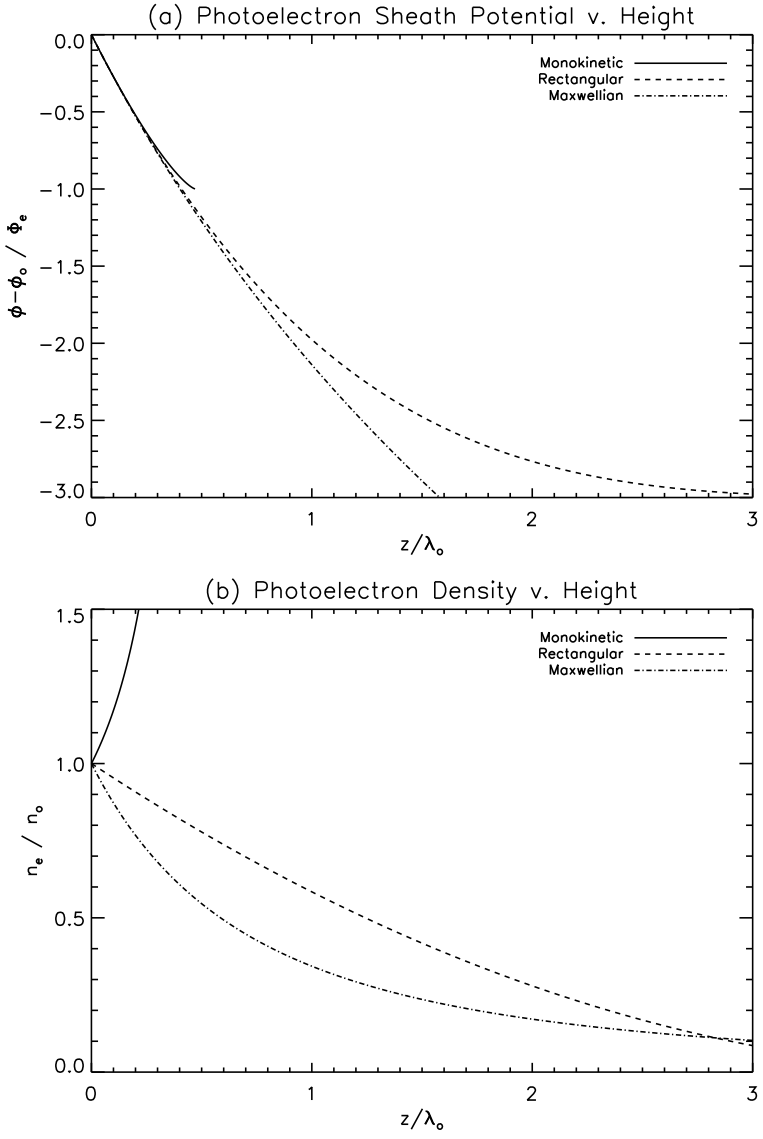

Figure 2.1: (a) The theoretical potential as a function of height above a photoemitting surface with no ambient plasma for three different photoelectron distributions. (b) The theoretical photoelectron density as a function of height for three different photoelectron distributions. Adapted from *Grard and Tunaley* [1971].

Previous work has shown that the distribution plays a significant role in determining the photoelectron sheath characteristics [*Grard and Tunaley*, 1971; *Walbridge*, 1973]. The emitted photoelectron energy distribution from lunar fines returned by the Apollo missions has been calculated from measurements of the photoelectron yield of lunar dust, convolved with the solar UV spectrum and the work function of lunar dust [*Feuerbacher et al.*, 1972]. To use this measurement in our model, we

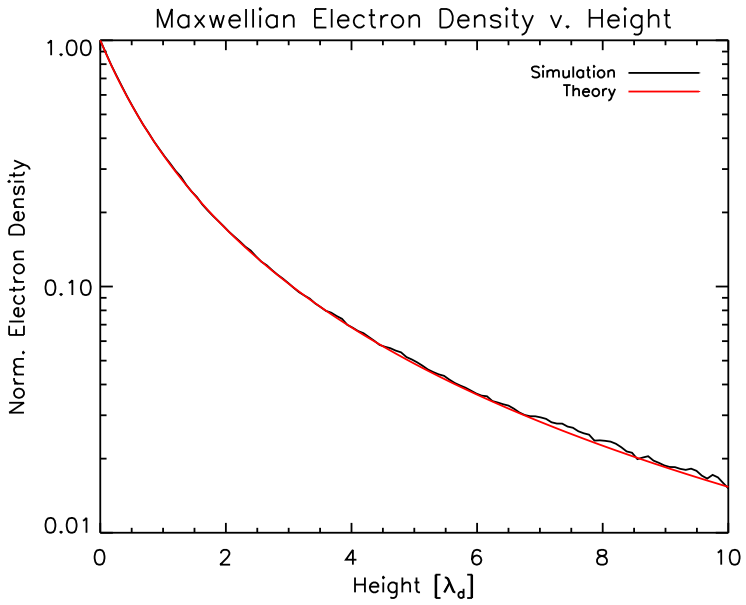

Figure 2.2: A comparison of 1-d PIC and theoretical results [*Grard and Tunaley*, 1971] for the normalized electron density above a photoemitting plate (with no ambient plasma) for a Maxwellian photoelectron distribution.

fit the experimentally-measured distribution to a function of the form, $f(v) \propto v^4 e^{-v^4/v_{pe}^4}$, where $v_{pe} = 6.21 \times 10^5$ m/s. The fit function reproduces several features of the measured distribution, including a strong peak at v_{pe} and a rapid decrease in the amount of higher energy photoelectrons. For our discussions, we shall refer to the measured distribution as the lunar case. A Maxwellian velocity distribution with $kT_{pe} = 2.2$ eV ($v_{th,e} = 6.21 \times 10^5$ m/s) is also used throughout our analysis as a comparison to the lunar distribution. Shown in Figure 2.3 are the emitted flux velocity distribution ($v\dot{f}(v)$) for the experimentally measured lunar distribution [*Feuerbacher et al.*, 1972], the analytic fit to this curve, and the reference Maxwellian. It should be noted that the angular distribution of lunar photoelectron emission is not known. The most significant difference between the two distributions is the lack of high-energy (> 6 eV) photoelectrons in the lunar distribution. In both cases, the photoelectron emission current density was kept constant at $J_{pe} = 4.5 \times 10^{-6}$ A/m^2 [*Willis et al.*, 1973]. The presence of the incoming solar wind flux was also included in the simulation to accurately represent the lunar plasma environment. Both solar wind ions and electrons are modeled as Maxwellians with $kT_{sw} = 10$ eV with a drift speed of $v_d = 4 \times 10^5$ m/s.

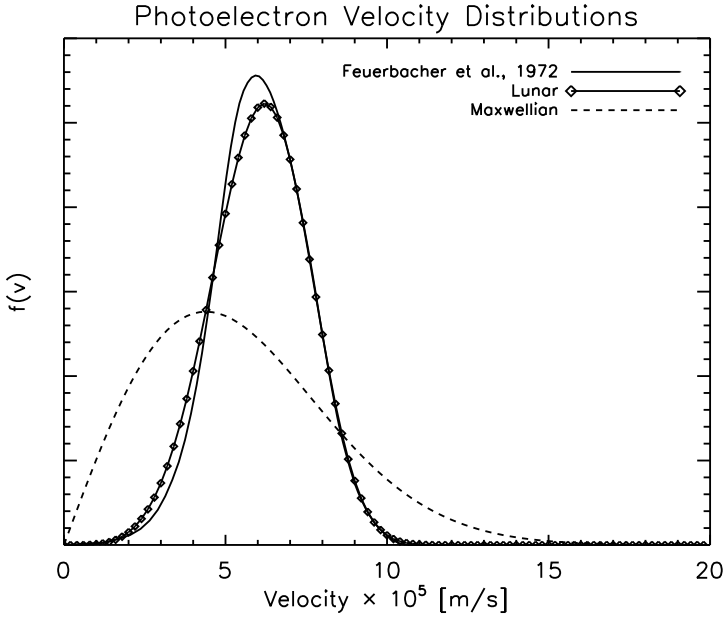

Figure 2.3: A comparison of the various photoelectron velocity distributions normalized to the area under the curve. The solid line is the distribution measured from lunar fines returned by Apollo 17 [*Feuerbacher et al.*, 1972], the diamonds are the function used as the lunar distribution in this paper and the dashed line is the comparable Maxwellian distribution.

Far from the lunar surface ($z > 50\lambda_D$), the plasma is quasi-neutral with a density of $n_e \approx n_i \approx 10^7$ m^{-3}.

Simulation results for the particle densities (photoelectron, solar wind electron and ion) for both the lunar and Maxwellian sheaths as a function of height are shown in Figure 2.4. The two profiles are qualitatively similar in many respects, including: (1) a high density of photoelectrons for $z \sim< 5$ m; (2) a decrease in the solar wind electron density as the solar wind electrons are accelerated towards the positively charged surface; (3) a constant solar wind ion density due to the supersonic velocity of the solar wind ions; and (4) a return to quasineutrality for $z >\sim 25$ m. The major differences between the density profiles is in the photoelectron density, which has a peak offset from the surface in the lunar case and decreases more rapidly as a function of height. For the Maxwellian case, the model predicts at the surface an electron density of $n_{e,o} = 1.5 \times 10^8$ m^{-3}, Debye length, $\lambda_D = 1.0$ m, and electric field $E_o = 3.0$ V m^{-1}, while for the lunar case, $n_{e,o} = 1.3 \times 10^8$ m^{-3}, $\lambda_D = 1.1$ m and $E_o = 3.1$ V m^{-1}. While the two different cases, Maxwellian

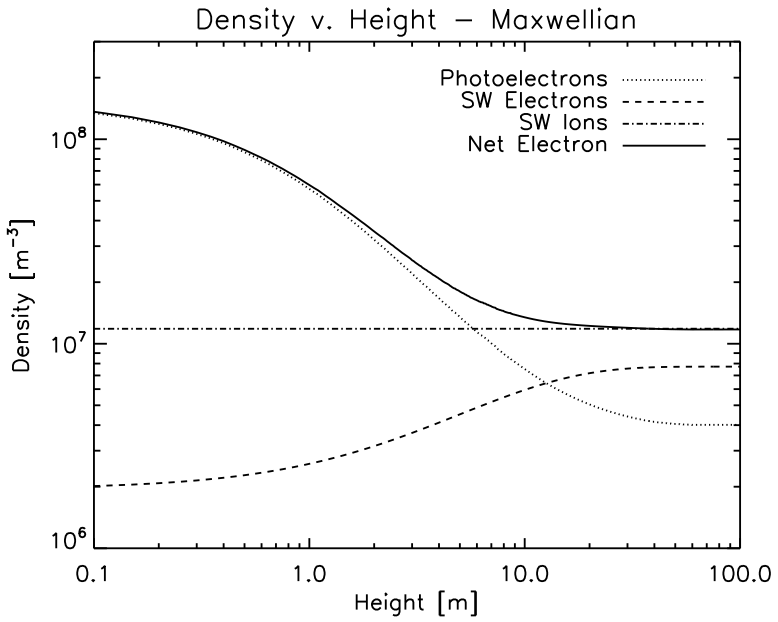

(a) Particle densities v. height - Maxwellian.

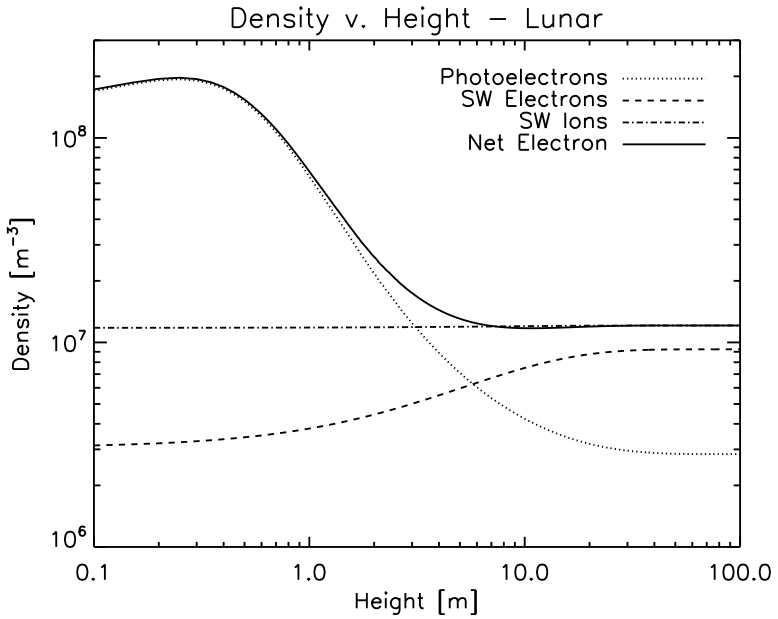

(b) Particle densities v. height - Lunar.

Figure 2.4: A comparison of the particle densities as a function of height for both the lunar and Maxwellian photoelectron sheaths.

and lunar, have similar plasma parameters, their potential profiles differ significantly. As shown in Figure 2.5(a), both cases were found to have non-monotonic potential distributions, as analytically predicted [*Guernsey and Fu*, 1970; *Nitter et al.*, 1998]. Shown in Figure 2.5(b) is a comparison of the electric field above the surface for the lunar and Maxwellian cases. The electric field in the lunar photoelectron sheath is weaker than the field in the Maxwellian sheath, mainly due to the lack of high-energy photoelectrons in the lunar distribution. Additionally, due to the non-monotonicity of the potential, both cases have a region of negative, or downward-pointing, electric field. As dust particles are expected to charge positively throughout most of the photoelectron sheath [*Whipple*, 1981; *Horányi*, 1996], regions of negative electric field will prevent any dust grain levitation. By $\approx$ 50 m above the surface in both cases, the sheath dies out and the plasma returns to the background, quasi-neutral state of the solar wind.

2.3.1 Solar UV Variability

A significant source of variability of the lunar surface plasma environment is due to solar UV irradiance. As the sun goes through its eleven year cycle, the UV irradiance can change by several orders of magnitude, with occasional solar flares drastically increasing the solar UV output from solar maximum levels [*Chamberlin et al.*, 2008]. Previous work has shown that conditions at solar maximum and during a solar flare can increase the lunar photoelectric current by factors of three and ten, respectively, from solar minimum conditions [*Sternovsky et al.*, 2008].

We have simulated the lunar photoelectron sheath (as defined in Section 2.3) for two additional photoelectron currents, $J_{pe} = 15.5$ μA m^{-2} and 45 μA m^{-2}, corresponding to solar maximum and flare conditions, respectively. All other parameters have been kept constant. Figure 2.6 shows the photoelectron density and electric field versus height for the solar minimum, solar maximum and flare conditions. For the photoelectron density, shown in Figure 2.6(a), the increased solar UV irradiance mainly contributes to increasing the photoelectron density by approximately three and ten for the solar maximum and flare conditions, respectively, from the solar minimum conditions, as was found in previous work [*Sternovsky et al.*, 2008]. For heights greater than 1 m, the photo-

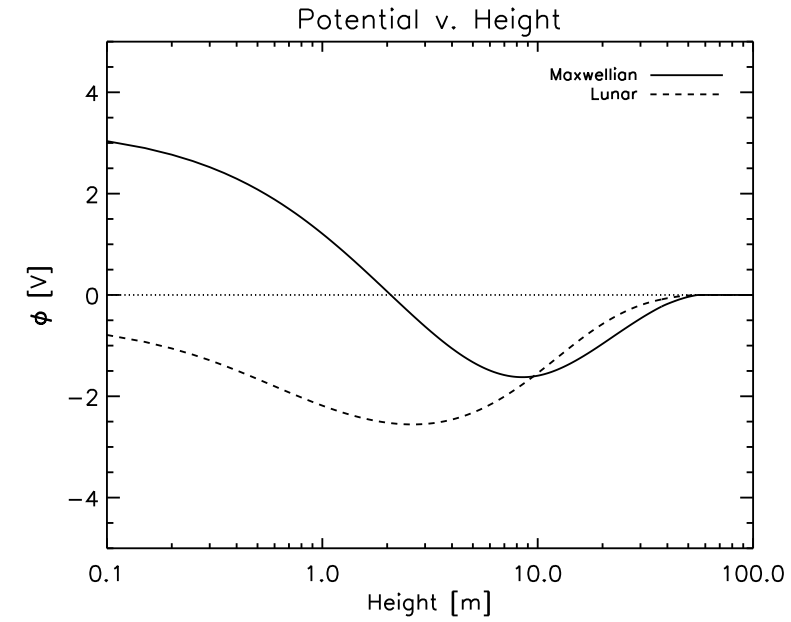

(a) Potential v. height.

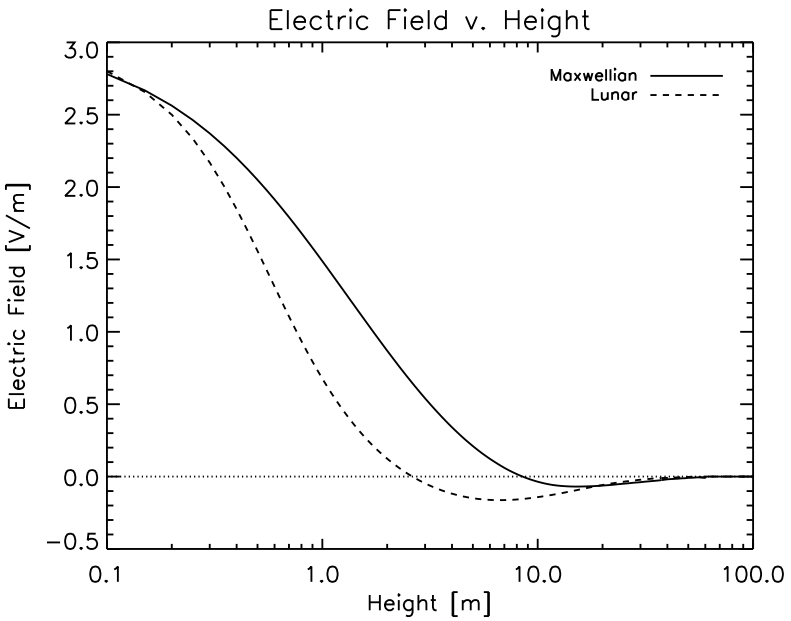

(b) Electric field v. height.

Figure 2.5: A comparison of the sheath potential and electric field above the surface for both the lunar and Maxwellian photoelectron sheaths.

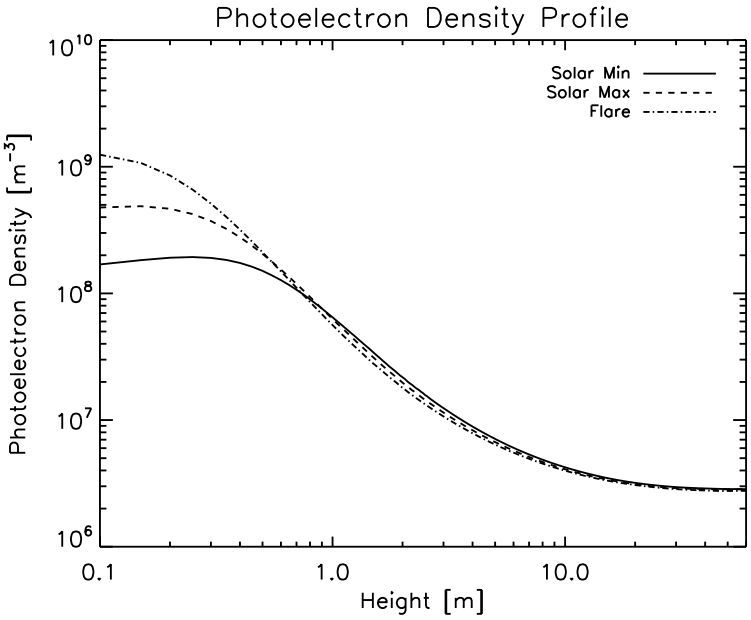

(a) Photoelectron density v. height

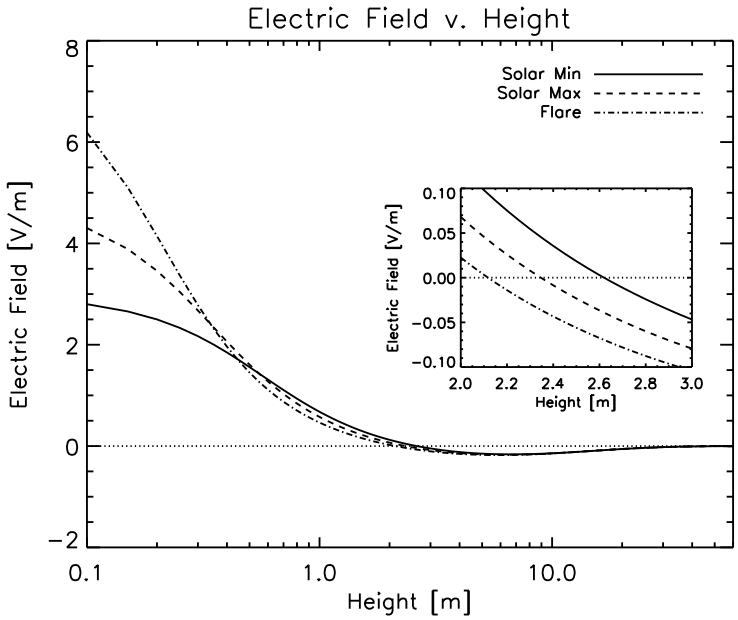

(b) Electric field v. height

Figure 2.6: The photoelectron density as a function of height for solar minimum, solar maximum, and flare conditions is shown in (a). An increase in the photoemission current by a factor of ≈ 8 yields a factor of 10 change in the photoelectron density. In (b) the electric field as a function of height for all three cases is shown. The surface electric field increases by ≈ 2 from solar minimum to flare conditions. All three conditions still maintain regions of negative electric field. The inset shows an expanded view of the region from 2 to 3 m, where the fields become negative, to highlight the differences among the three cases.

electron density profiles for all three conditions are nearly equivalent, yet small differences are seen due to the nonlinear nature of surface shielding effects. Figure 2.6(b) shows an increase of 1.5 and 2 times the solar minimum surface electric field for the solar maximum and flare conditions. These values are significantly lower than those calculated before, which predicted multiplicative increases of 2.5 and 5, respectively [*Sternovsky et al.*, 2008]. These results again show the relative weakness of the electric field in the lunar photoelectron sheath as compared to an equivalent Maxwellian distribution. Shown in the inset in Figure 2.6(b) is a subtle, yet important, difference between the three cases. Increased photoemission causes the transition from positive to negative electric field to occur closer to the lunar surface, as the surface charge density is shielded more effectively in the higher current cases.

2.3.2 Solar Zenith Angle Dependence

While the one-dimensional simulations to this point have focused on the plasma environment over a range of conditions, they have all been set to values at the sub-solar point, defined as the point where the solar zenith angle, $\alpha = 0$. The solar zenith angle is an interesting parameter to study as a transition must occur between the non-monotonic potentials on the dayside to the (supposedly) monotonic potentials on the nightside of the moon (neglecting secondary emission). To study the dependence of the photoelectron sheath on the solar zenith angle, the standard solar wind case ($T_{ph} = 2.2$ eV, $T_{sw} = 10.0$ eV, $u_i = 400$ km s^{-1}), was run with the photoelectron current, J_{ph}, and the solar wind ion current, J_{swi}, modified by $\cos(\alpha)$ for values in the range $0 < \alpha < 80°$. The solar wind electron current, J_{swe}, is not modified due to the highly thermalized nature of the solar wind electrons. Essentially, the lunar surface (except the deep wake region) is bathed in an isotropic flux of solar wind electrons. Shown in Figure 2.7 are the simulation results for the sheath potential as a function of height above the lunar surface for these cases. For $\alpha < 70°$, the non-monotonic sheath is present with the surface potential, V_o, and the minimum potential, V_m, decreasing with increasing α. Eventually, for $\alpha > 70°$, the sheath reverts to a negative monotonic sheath.

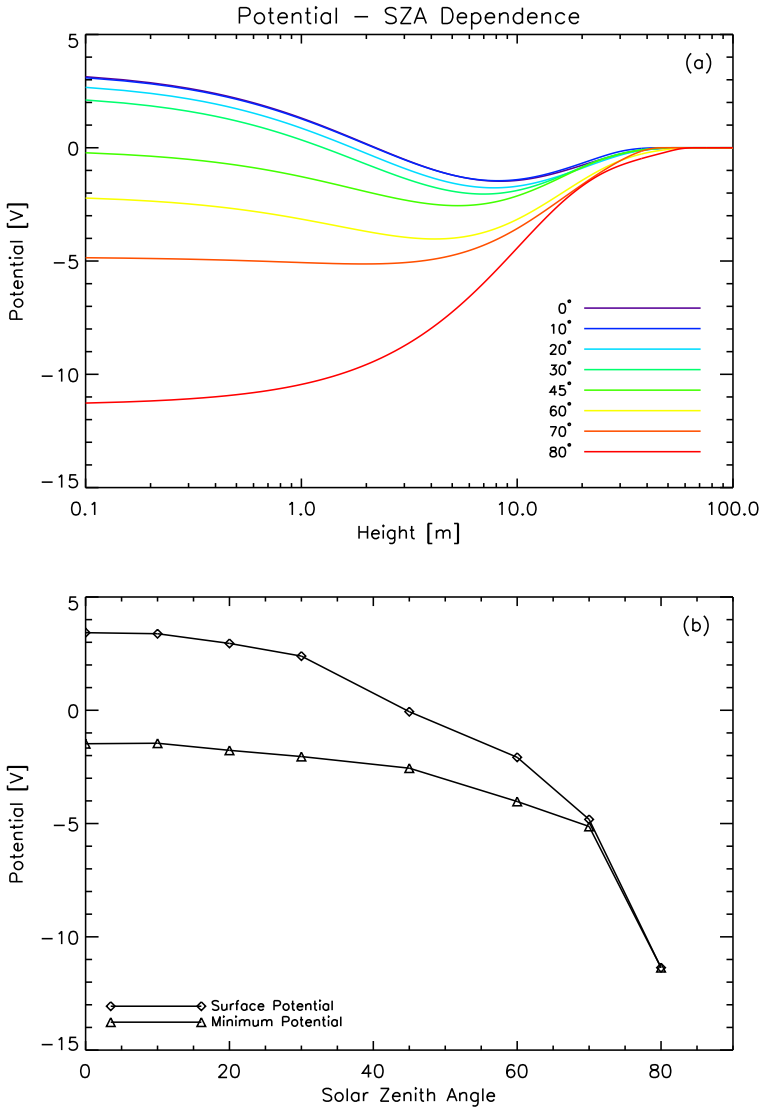

Figure 2.7: (a) The potential as a function of height above the lunar surface in the solar wind for a series of solar zenith angles (SZA). As the SZA increases, the sheath switches from non-monotonic to monotonically negative. (b) The surface and minimum potentials for the SZA values modeled in (a). As α increases, both potentials decrease, as does the potential difference between the surface and minimum. At $\alpha = 80°$, the surface and minimum potential values are identical as the sheath has become monotonically negative.

2.3.3 T_{ph} and T_{sw} Dependence

While typical values for the photoelectron and solar wind temperatures have been used in all previous simulations, there exists both variability and uncertainty in these values. For the photoelectron temperature, T_{ph}, the best value comes from measurements of the photoelectric yield and energy distribution from lunar fines returned by the Apollo astronauts [*Feuerbacher et al.*, 1972]; however, the applicability of these measurements to the bulk lunar surface is not completely established. Effects arising from both bulk photoemission and compositional variability could cause *in-situ* photoelectron temperatures to vary from ground-based measurements. The solar wind temperature, T_{sw}, has been extensively measured by a variety of spacecraft near the Moon, and is generally in the range of 10 eV but can vary slightly [*Halekas et al.*, 2008c].

Shown in Figures 2.8(a) and 2.8(b) are the potential as a function of height above the lunar surface for variation in T_{ph} and T_{sw}, respectively. For Figure 2.8(a), the photoelectron temperature is modeled between 1 and 10 eV with the solar wind temperature constant at $T_{sw} = 10$ eV. As T_{ph} increases, the surface and minimum sheath potentials both increase and for $T_{ph} > 6$ eV, the sheath changes from non-monotonic to monotonically positive. In contrast, the surface charge density (and in turn, the surface electric field) remains relatively constant over this range. The solar wind temperature was modeled for $10 < T_{sw} < 100$ eV with the photoelectron temperature at $T_{ph} = 2.2$ eV. Figure 2.8(b) shows that as the solar wind temperature increases, the surface and minimum potentials decrease with an approximately linear relationship. Interestingly, the increase in solar wind temperature does not affect the near-surface (photoelectron-dominated) sheath, but rather causes a double-layer like structure to form. This structure serves to reflect an increasing portion of the solar wind electrons back from the surface, in part to maintain quasineutrality far from the lunar surface. Additionally, the small fraction of energetic photoelectrons that do escape the near-surface potential well are subsequently accelerated through the double layer to energies far above their temperature. As discussed further in Chapter 4, this beam of photoelectrons can be detected by orbiting instrumentation and is a hallmark for non-monotonic potentials *in-situ* [*Halekas et al.*,

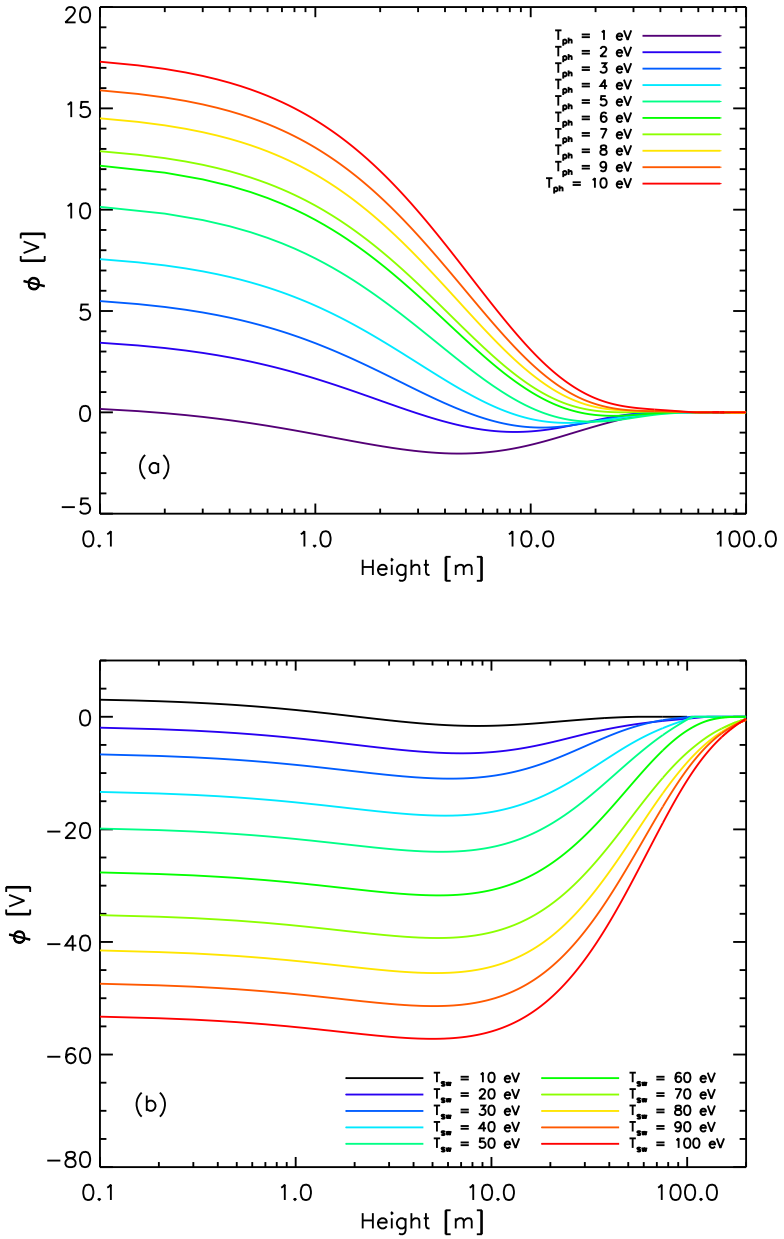

Figure 2.8: (a) The potential as a function of height above the lunar surface for $1 < T_{ph} < 10$ eV with $T_{sw} = 10$ eV. (b) The potential as a function of height above the lunar surface for $10 < T_{sw} < 100$ eV for $T_{ph} = 2.2$ eV.

2008c; *Poppe et al.*, 2011].

2.4 Dust Particle Levitation

The dynamics and equilibria of charged and levitated dust particles above the lunar surface have been previously studied by a number of other models [*Nitter and Havnes*, 1992; *Nitter et al.*, 1994, 1998; *Colwell et al.*, 2005; *Borisov and Mall*, 2006; *Stubbs et al.*, 2006; *Farrell et al.*, 2007]. Here, we model lunar dust charging and dynamics in a time-dependent fashion using the photoelectron sheath profile specific to the lunar surface.

2.4.1 Levitation Equilibria

A dust particle suspended in a photoelectron sheath will levitate if the electric and gravitational forces on the particle balance. The electric force on the grain is given by $F_e = q_d E$, where q_d is the charge on the grain. This charge is related to the grain potential, ϕ_d, by,

$$\phi_d = q_d / C_d, \tag{2.8}$$

where we have used the capacitance of a spherical grain, $C_d = 4\pi\epsilon_o a$, where a is the grain radius [*Goertz*, 1989; *Horányi*, 1996]. The equilibrium grain potential, ϕ_d, which is independent of grain size, is determined as a function of height in the sheath by calculating the grain potential at which the sum of all currents to the grain is zero. The currents included are photoemission, photoelectron collection, and solar wind ion and electron collection [*Whipple*, 1981; *Northrop and Birmingham*, 1996; *Horányi*, 1996]. While recent work has shown that photoemission from micron and sub-micron sized grains may be grain-size dependent [*Abbas et al.*, 2006, 2007], there is some uncertainty regarding the physical mechanism behind this. Therefore, we have not included such an effect at this time. The equilibrium levitation points of the charged dust grain are found by searching for locations where the electric and gravitational forces balance. There are typically two points in the photoelectron sheath at which this condition is satisfied [*Nitter et al.*, 1998; *Robertson et al.*, 2003; *Colwell et al.*, 2005]. By considering the second derivative of the net mechanical

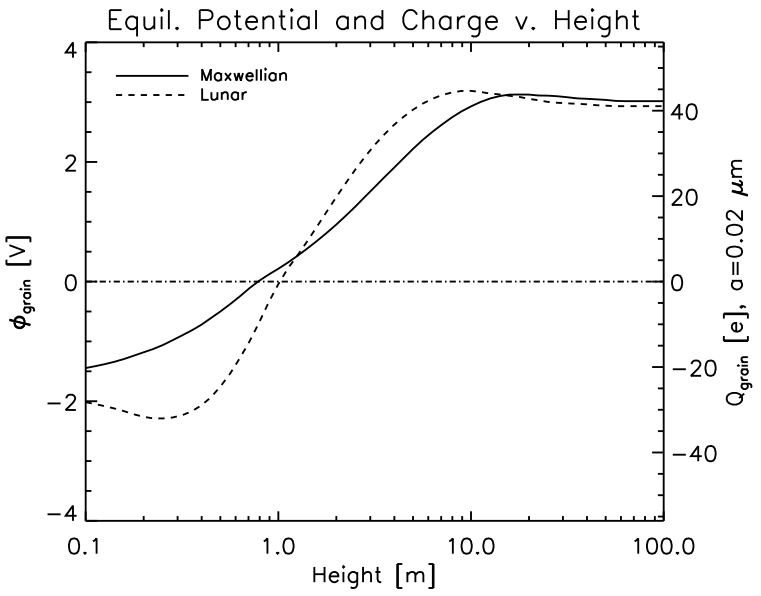

Figure 2.9: The equilibrium grain potential for both the Maxwellian and lunar cases. Depicted on the right axis is the equilibrium charge for a 0.02 μm grain.

potential on the grain, the levitation points can be classified according to their stability. In the cases presented here, the lower point is unstable while the upper point is stable. We perform this analysis for the two case studies presented in Section 2.1: (1) comparison of the Maxwellian and lunar photoelectron distributions, and (2) inclusion of the variability in the solar UV irradiance for the lunar distribution. The plasma densities and electric field are taken from the results of the PIC code for each condition.

2.4.1.1 The Effect of the Photoelectron Energy Distribution on Levitation

Figure 2.9 shows the equilibrium grain surface potential, as well as the grain charge for a 0.02 μm grain, as a function of height above the surface for the Maxwellian and lunar cases. To obtain the potential, the net current to the grain was set to zero and solved for roots in ϕ, given,

$$I_{ph}(q) - I_{phc}(x,q) - I_{swe}(x,q) + I_{swi}(x,q) = 0, \tag{2.9}$$

where I_{ph} is the photoemission current from the grain, I_{phc} is the current from the collection of ambient photoelectrons, and I_{swe} and I_{swi} are the solar wind electron and ion collection currents, respectively. Both cases qualitatively show similar curves for the grain potential and charge, however, grains in the lunar case have a lower surface potential and charge closer to the surface and a greater potential and charge farther from the surface than in the Maxwellian case. Above ≈ 10 m, grains in both cases, regardless of size, reach a maximum potential of ≈ 3 V. For a 0.02 μm grain, the potential is equivalent to a grain charge of ≈ 40 e. Figure 2.10 shows the ratio of the electric to gravitational forces for a 0.02 μm grain for the Maxwellian and lunar sheaths. The Maxwellian case has a consistently higher force ratio than the lunar case due to its stronger electric field. For heights too close to the lunar surface, the force ratio becomes negative due to the negative charge on the grain, while for heights too far from the lunar surface, the ratio becomes negative because of the negative electric field in the sheath. For the particle size presented ($a = 0.02$ μm), the equilibrium points for the Maxwellian and lunar cases are at ≈ 8.5 m and ≈ 2.5 m, respectively. Thus, for identically sized grains, the lunar sheath cannot support dust levitation as high as the Maxwellian sheath, mainly due to the weaker lunar electric field.

Figure 2.11 shows the stable levitation height for dust grains in the Maxwellian and lunar sheaths as a function of grain radius. An upper limit on the radius of levitating particles as a function of height above the lunar surface can be set at ≈ 0.072 μm and ≈ 0.04 μm for the Maxwellian and lunar cases, respectively. Additionally, particles cannot be levitated higher than ≈ 8.5 m and ≈ 2.5 m, corresponding respectively to the height at which the electric field becomes negative in each case. These values place important constraints on the interpretation of the observations of levitating dust above the lunar surface and are discussed further in Section 2.5.

2.4.1.2 The Effect of Solar UV Variability on Levitation

The increased photoemission for the solar maximum and solar flare conditions increases the sheath electric field and also causes grains to attain a higher charge throughout the sheath. These two effects increase the ability of the sheath to levitate dust grains. Figure 2.12 shows the

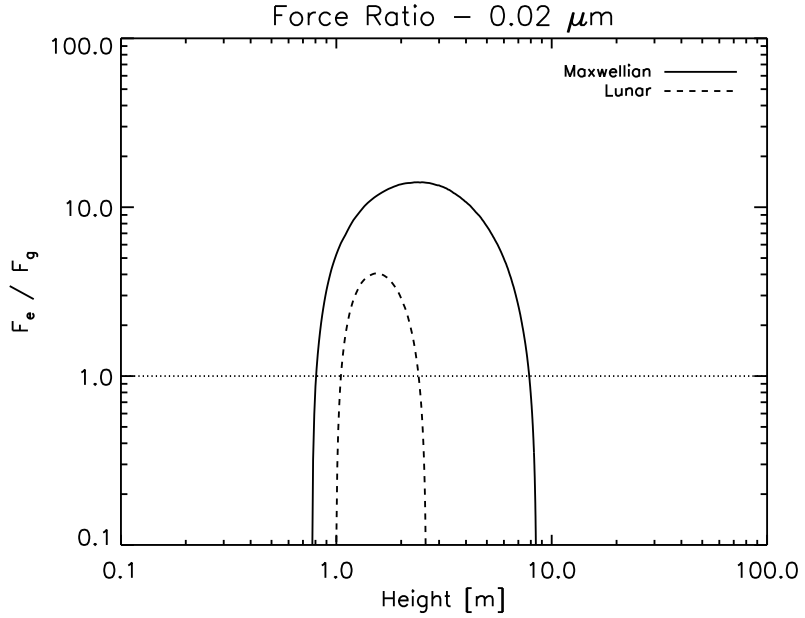

Figure 2.10: The ratio of the electric to gravitational force for a 0.02 μm grain for both the Maxwellian and lunar cases. The Maxwellian grain has an equilibrium at $z \approx 8.5$ m while the lunar grain has an equilibrium at $z \approx 2.5$ m. The line, $F_e/F_g = 1$ is shown for visual aid.

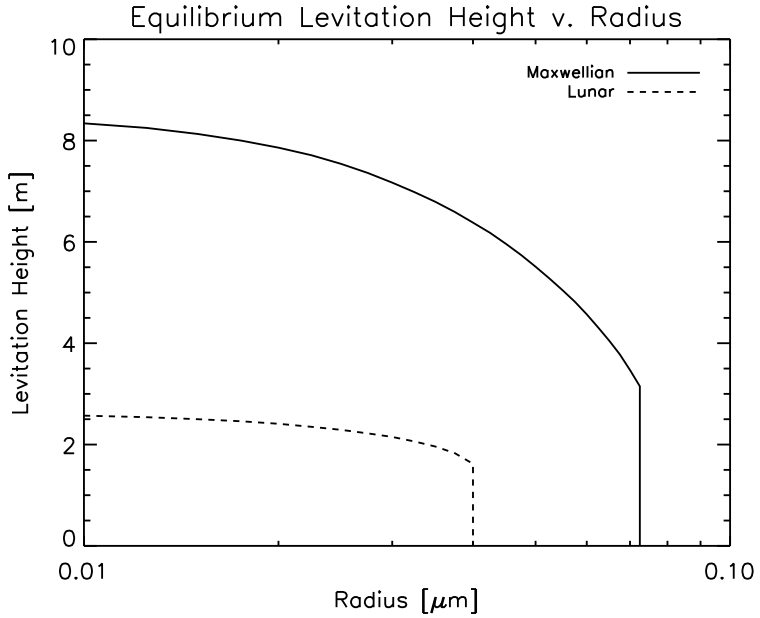

Figure 2.11: The equilibrium levitation height as a function of particle radius is shown for both the Maxwellian and lunar sheaths. For the Maxwellian case, particles with radii, $r > 0.072$ μm, cannot be stably levitated in the sheath, while for the lunar sheath, this limit drops to $r > 0.04$ μm.

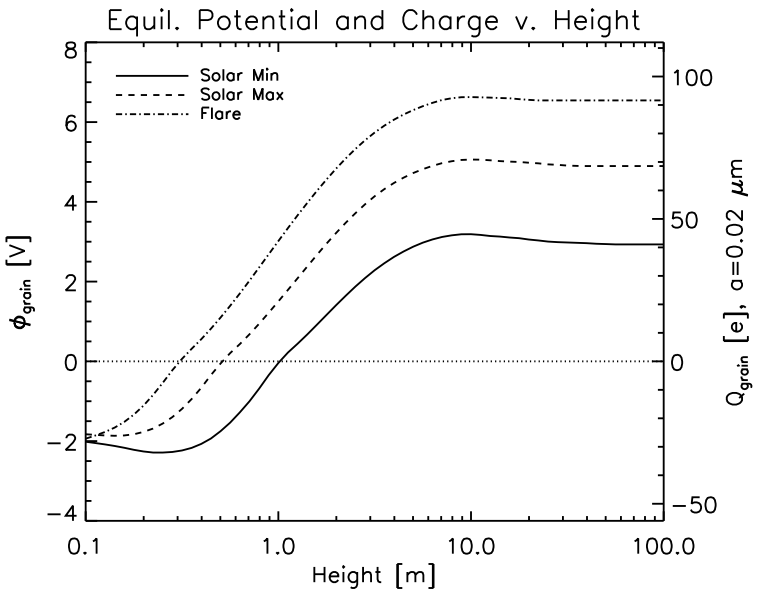

Figure 2.12: The equilibrium grain potential and charge for a 0.02 μm grain as a function of height above the lunar surface for the solar minimum, solar maximum and solar flare conditions. Increased photoemission leads to a greater equilibrium grain potential and charge.

equilibrium grain potential and charge for a 0.02 μm grain for the solar minimum, solar maximum and solar flare conditions. The maximum charge on a 0.02 μm grain increases from $\approx$ 40 e during solar minimum to $\approx$ 70 e and $\approx$ 90 e during solar maximum and solar flare conditions, respectively. Additionally, the height at which the grain potential and charge transition from negative to positive occurs at successively lower heights for increased photoemission.

Using the same analysis as Section 2.4.1.1, the force ratio as a function of height and the equilibrium levitation height as a function of grain radius can be determined for the solar maximum and solar flare conditions. In Figure 2.13, an increase in the ratio of the electric to gravitational forces on a 0.02 μm grain for both the solar maximum and solar flare conditions is shown. For example, at 1 m, the force ratio for the 0.02 μm grain increases by factors of 10- and 20-fold for the solar maximum and solar flare conditions, respectively. The increase is due to the combination of the increase in the sheath electric field and the increase in the equilibrium grain charge. Figure 2.14 shows the equilibrium levitation height as a function of grain radius for all three solar UV

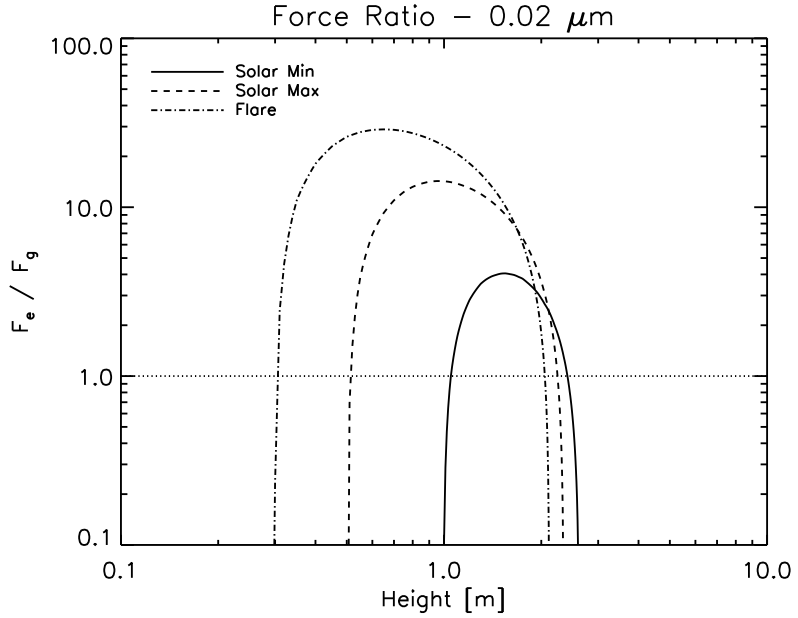

Figure 2.13: The ratio of the electric and gravitation forces for a 0.02 μm grain is shown as a function of height above the lunar surface for the solar minimum, solar maximum and solar flare conditions. Increased photoemission causes a higher sheath electric field and higher grain charge, leading to an increased ability to levitate dust grains on the lunar surface.

conditions. The maximum grain radius that can be levitated increases from 0.04 μm for solar minimum conditions, to 0.075 μm and 0.12 μm for solar maximum and flare conditions, respectively. Additionally, the maximum levitation height decreases for increasing solar irradiation, due to the decreasing height of the point at which the sheath electric field becomes negative, as seen in the inset in Figure 2.6(b).

2.4.2 Levitation Dynamics

Despite the theoretical prediction of stable levitation equilibria for dust grains in both the lunar and Maxwellian sheaths, the accessibility of these equilibria must also be considered. By some mechanism, either micrometeoroid bombardment or electrostatic liftoff, dust grains can be ejected from the surface into the photoelectron sheath. With a set of general initial conditions for grains on the sunlit lunar surface, we can simulate the instantaneous position, velocity and charge of the grain by simultaneously integrating a coupled set of differential equations. The set of differential

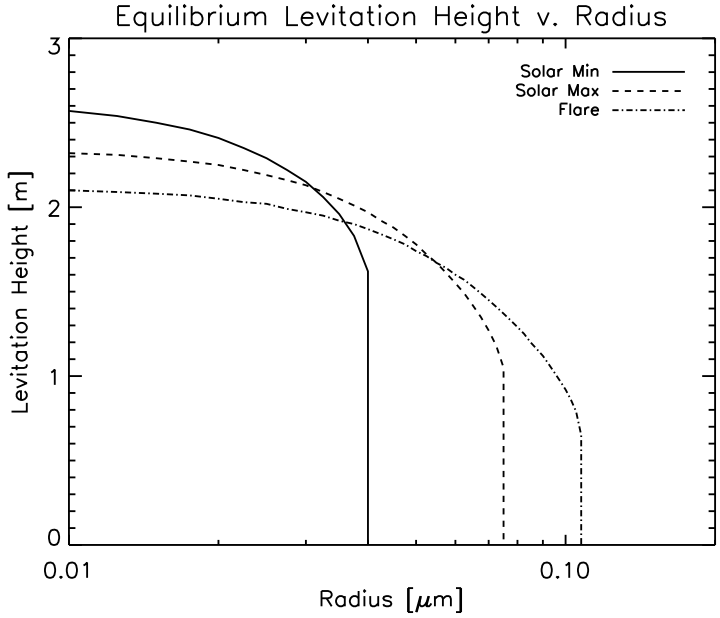

Figure 2.14: The equilibrium levitation height is shown as a function of particle radius for solar minimum, solar maximum and flare conditions. The increased photoemission current increases the maximum possible levitation grain radius from 0.04 μm at solar minimum to 0.075 μm and 0.12 μm for solar maximum and flare conditions, respectively.

equations that governs the test particle dynamics and charging are,

$$\frac{dx}{dt} = v \tag{2.10}$$

$$\frac{dv}{dt} = \frac{qE(x)}{m} - g_{moon} \tag{2.11}$$

$$\frac{dq}{dt} = I_{ph}(q) - I_{phc}(x,q) - I_{swe}(x,q) + I_{swi}(x,q), \tag{2.12}$$

where x, v, q and m are the particles height, velocity, charge, and mass, respectively, g_{moon} is the lunar gravitational acceleration (1.6 m s^{-2}), $E(x)$ is the sheath electric field, and I_{ph}, I_{phc}, I_{swe} and I_{swi} are the currents due to photoelectron emission, photoelectron collection, solar wind electron and solar wind ion collection, respectively. We explore a broad range of initial velocities for completeness. Typical initial charges for these grains can be estimated by using the surface charge density from the PIC simulations in Section 2.1. For the lunar case, the surface charge density, σ, is approximately 3×10^8 e m^{-2}. With this charge density, only one in one hundred 1.0 μm-sized grains has a single charge. Therefore, in our simulations, we explore the behavior of grains with

either zero or one unit of charge initially. As time evolves, the grain charges discretely with a Monte Carlo type analysis, in order to capture the quantized nature of the grain charge. At each time step, the net current to the grain is calculated, a probability is assigned for the collection or loss an electron, and a random number generator is used to determine if the grain gains or loses a charge. Shown in Figure 2.15 are the position, velocity and charge for a 0.02 μm grain with initial position, $x_o = 0$, initial velocity, $v_o = 3$ m s^{-1}, and initial charge, $q_o = 1$ e during the first 200 s of grain levitation. Within two minutes, the grain oscillates stably between 1 and 4 m, with velocities between ± 3 m s^{-1}. While not shown, the grain charge reaches an equilibrium of ≈ 20 e within minutes as well. The grain remained stably oscillating for the entire duration of the simulation, more than 15 minutes.

Due to the random charging model of the dust grains, repeated simulations of the same radius and initial velocity will yield different results. Grains that do not attain enough charge during the first pass through the photoelectron sheath will not be able to overcome the gravitational force on the grain. In order to assess the likelihood of stable levitation for dust grains, each combination of radius and initial velocity are traced 100 times. If the grain levitates for more than ten minutes, it is considered stably levitating. After simulating a large set of grain radii and initial velocities ($0.005 < a < 0.1$ μm, $0.5 < v_o < 25$ m s^{-1}), the region of accessible stable levitation for the lunar sheath was determined to exist for grains less than 0.02 μm and initial velocities less than ≈ 4 m s^{-1}. Grains launched with too large of an initial velocity ($v_o > 4$ m s^{-1}), regardless of size, cannot be slowed by the sheath electric field enough to prevent re-impact into the lunar surface and essentially follow ballistic trajectories. Furthermore, for regions in which stable, dynamically accessible levitation does exist, the probability of stable levitation is less than 20%. The same analysis was repeated for the solar maximum and solar flare conditions. Similar to the solar minimum case, not all theoretical levitation equilibria are dynamically accessible, with limits on the solar maximum case of approximately $a < 0.03$ μm and $v_o < 5$ m s^{-1} and on the solar flare case of $a < 0.05$ μm and $v_o < 7$ m s^{-1}. In both the solar maximum and solar flare conditions, the probability of levitation increased to $\approx 50\%$ and $\approx 90\%$, respectively, for the smallest grains.

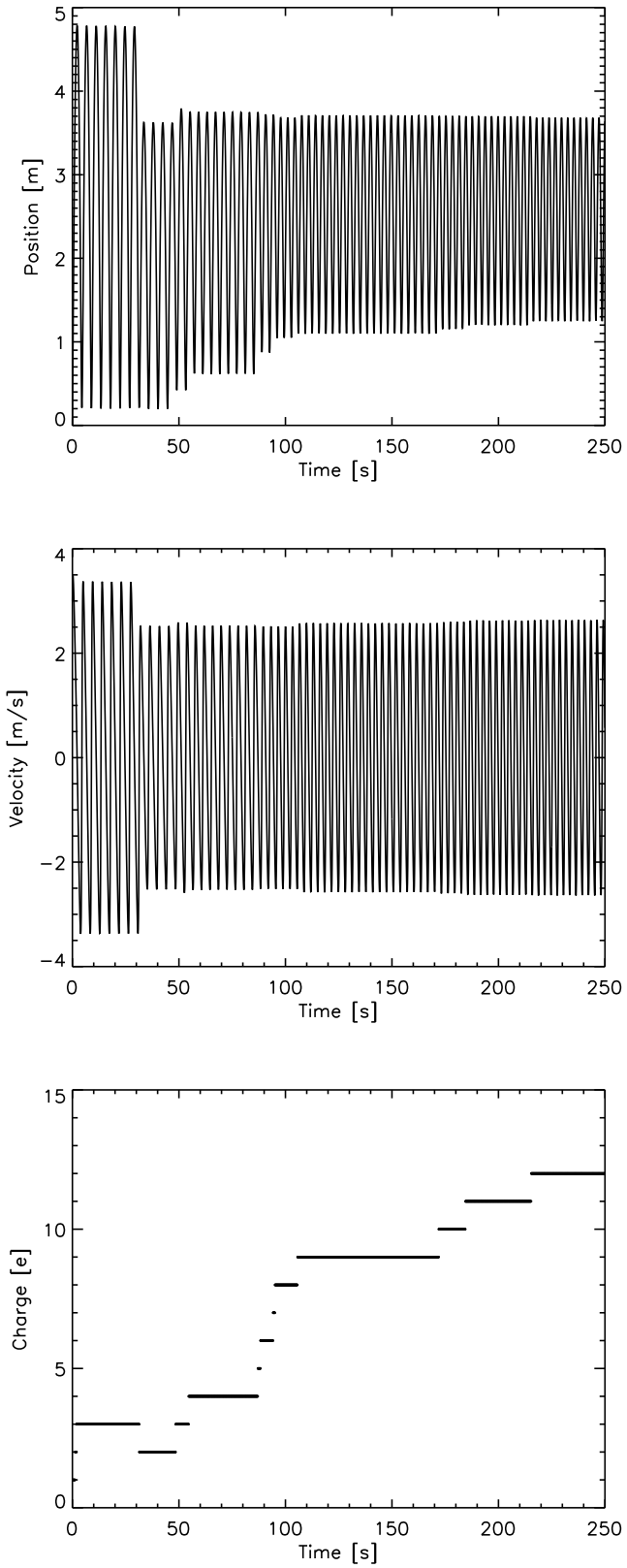

Figure 2.15: The position, velocity and charge for a 0.02 μm grain, with initial position, $x_o = 0$, initial velocity, $v_o = 3$ m/s and initial charge, $q_o = 1$ e. Discrete jumps in the grain position and velocity are due to the collection or loss of a single electron.

2.5 Discussion

The lunar photoelectron sheath has been simulated using a PIC method in order to investigate the nature of the lunar plasma environment and to explain observed dusty plasma phenomena. The model has been applied to five main areas:

(1) Modeling the sunlit, solar-wind exposed lunar surface plasma environment at the sub-solar point: We have found that inclusion of the measured lunar photoelectron velocity distribution predicts a much weaker photoelectron sheath than a sheath with a Maxwellian distribution of equivalent temperature. We attribute this to the relative lack of high-energy photoelectrons in the lunar distribution. We have also found that inclusion of the solar wind yields stable non-monotonic potentials in both the lunar and Maxwellian cases, as analytically predicted.

(2) Inclusion of the variability of the solar UV irradiance: By repeating the model with the solar UV irradiance set to solar maximum and solar flare conditions, we predict a change in the photoelectron density of 3 and 10, respectively, and a change in the surface electric field of 1.5 and 2 times, respectively. We suggest that any future measurements or observations of lunar dust activity should be correlated with solar UV irradiation conditions.

(3) Investigation of the variability of the photoelectron sheath with respect to the solar zenith angle, α, the photoelectron temperature, T_{ph}, and the solar wind temperature, T_{sw}: The model shows that for varying values of these three parameters, the sheath can take significantly different forms, including both negative and positive monotonic sheaths (for high SZA and high T_{ph}, respectively). Combined variation over these parameters yields a significant amount of geophysical variability and *in-situ* measurements should correlate measurements with these values.

(4) Presence of levitation equilibria for sub-micron and micron sized dust grains: Using a test-particle approach, we have calculated the characteristics of levitation equilibria for lunar

dust grains at the sub-solar point. The model predicts that both the lunar and Maxwellian sheaths are not capable of supporting electrostatic dust grain levitation for grains with radii, $r > 0.4$ and $r > 0.7$ μm, respectively. A comparison of these limits with previous *in-situ* observations is made below.

(5) Time-dependent charging and dynamics of lunar dust grains: Using the output from the PIC code, combined with a coupled set of differential equations for the grain position, velocity and charge, we have studied the dynamics of lunar dust grains embedded in the photoelectron sheath. The test-particle model predicts that despite the prediction of stable levitation equilibria, not all grain sizes and initial velocities yield stable, electrostatically levitated dust grains above the lunar surface.

Comparison to previous models of the lunar photoelectron sheath and associated dust dynamics highlights some of the important results from this work. Previous work derived a model concerning the lofting of lunar dust grains, where lofting is defined as the ballistic ejection of micron and sub-micron sized dust grains to altitudes > 100 m [*Stubbs et al.*, 2006]. While our work has primarily focused on the possibility of electrostatic levitation using both the lunar-specific sheath profiles and time-dependent dust grain charging, our model can be qualitatively compared with the *Stubbs et al.* [2006] model. Notably, the presence of a downward electric field above the photoelectron sheath (due to the non-monotonic potential profile), would decelerate any charged grains (assuming positive charge in sunlight) that were ejected from the surface. While this deceleration would imply a lesser ability to loft grains to km-scale heights, it would not necessarily preclude all grains from begin lofted. Additionally, we find no reason why both static levitation and ballistic lofting would not simultaneously be present, albeit with different characteristics. Previous models of electrostatic levitation of dust grains for the asteroid 433 Eros [*Colwell et al.*, 2005; *Hughes et al.*, 2008] or the Moon [*Nitter and Havnes*, 1992; *Nitter et al.*, 1998; *Colwell et al.*, 2009] differ in their reported maximum levitating grain size. In both models, this is attributable to the assumption of a Maxwellian photoelectron distribution, which, as demonstrated in this model, yields typically

stronger electric fields than the lunar photoelectron distribution. Additionally, in the 433 Eros model, the weaker gravity allows levitation of larger particles than an equivalent case on the lunar surface. Notably, the *Nitter et al.* [1998] model included the possibility of non-monotonic potential profiles by including the solar wind influx.

While we assumed that grains on the lunar surface begin with at most a single charge based on the simulated surface charge density, it is theoretically possible that other processes, such as micrometeorite bombardment or energetic particle impact could increase the initial grain charge and therefore increase the likelihood of levitation. Micrometeorite bombardment has been previously studied as a possible mechanism for dust grain levitation and lofting [*Rennilson and Criswell*, 1974; *Zook and McCoy*, 1991; *Colwell et al.*, 2005] and has been found insufficient in magnitude to explain various lunar dusty phenomena. Recent laboratory experiments have demonstrated the ability to electrostatically mobilize micron-sized dust grains in a plasma environment similar to the night-side of the Moon [*Wang et al.*, 2009], and such an electrostatic transport mechanism may also be active near the lunar terminator.

Previous analyses of both the Lunar Ejecta and Meteorites experiment (LEAM) measurements of lunar dust transport and the Surveyor images of lunar horizon glow have determined the height and size of typical levitated dust grains. A typical grain radius of $a \approx 6$ μm and levitation height of $h \approx 3 - 30$ cm has been calculated for levitated lunar dust grains based on analysis of the Surveyor images [*Criswell*, 1972; *Rennilson and Criswell*, 1974; *Colwell et al.*, 2007]. While this grain radius contradicts predictions by the PIC model presented here, the explanation of this discrepancy most likely is due to the one-dimensional constraints of the model. Previous work has theorized that lofting of dust grains is most effective near the lunar terminator where sunlit and shadowed patches are immediately adjacent, resulting in larger electric fields. The one-dimensional PIC model cannot simulate topographical relief and thus, we cannot make explicit comparison to either the LEAM or the Surveyor measurements near the terminator [*Criswell*, 1972; *Berg et al.*, 1974].

The set of simulations presented here have only begun to explore the richness and complexity of the lunar photoelectron sheath. Many additional factors, including the self-consistent presence of charged, sub-micron and micron-sized dust grains and local lunar topography may have significant effects on the profile of the lunar photoelectron sheath and its ability to charge, mobilize and levitate dust grains. LEAM and Surveyor observations have indicated that the prime regions of interest for lunar dust grain levitation are the terminators, where oblique solar illumination and complex surface topography will significantly alter the near-surface lunar plasma environment.

2.6 Ongoing and Future Work

2.6.1 Three-dimensional PIC Simulations

The one-dimensional simulations presented above have yielded significant insight into the structure and variability of the lunar near-surface plasma environment. One area of investigation which the 1-d code cannot explore is the role of surface topography in modifying the spatial structure of the lunar photoelectron sheath. As discussed in previous work [*Farrell et al.*, 2007, 2010], boulders and craters on the lunar surface that are equal to or larger than the local plasma Debye length can generate 'mini-wakes' as the solar wind convects past the obstacle. Additionally, even simple surface relief can introduce changes in the vertical and especially horizontal electric fields as compared to the one-dimensional case.

Using the three-dimensional PIC simulation code, VORPAL© [*Verboncoeur et al.*, 1995; *Nieter and Cary*, 2004], the role of surface topography in altering the lunar plasma environment can be extensively explored. Initial simulations have focused on the plasma environment above a 10 m scale crater on the lunar surface, with typical solar wind conditions ($T_{ph} = 2.2$ eV, $T_{sw} = 10$ eV, $u_i = 400$ km s^{-1}). Figure 2.16 shows the electric potential above the crater for three different solar wind / UV incidence angles: 0°, 45° and 90°. In the 0° case, areas outside the crater have potential profiles similar to the one-dimensional simulation, as expected, but near and in the crater, the surface potential is lower than outside. This is most likely due to a $\cos(\theta)$ factor present in the

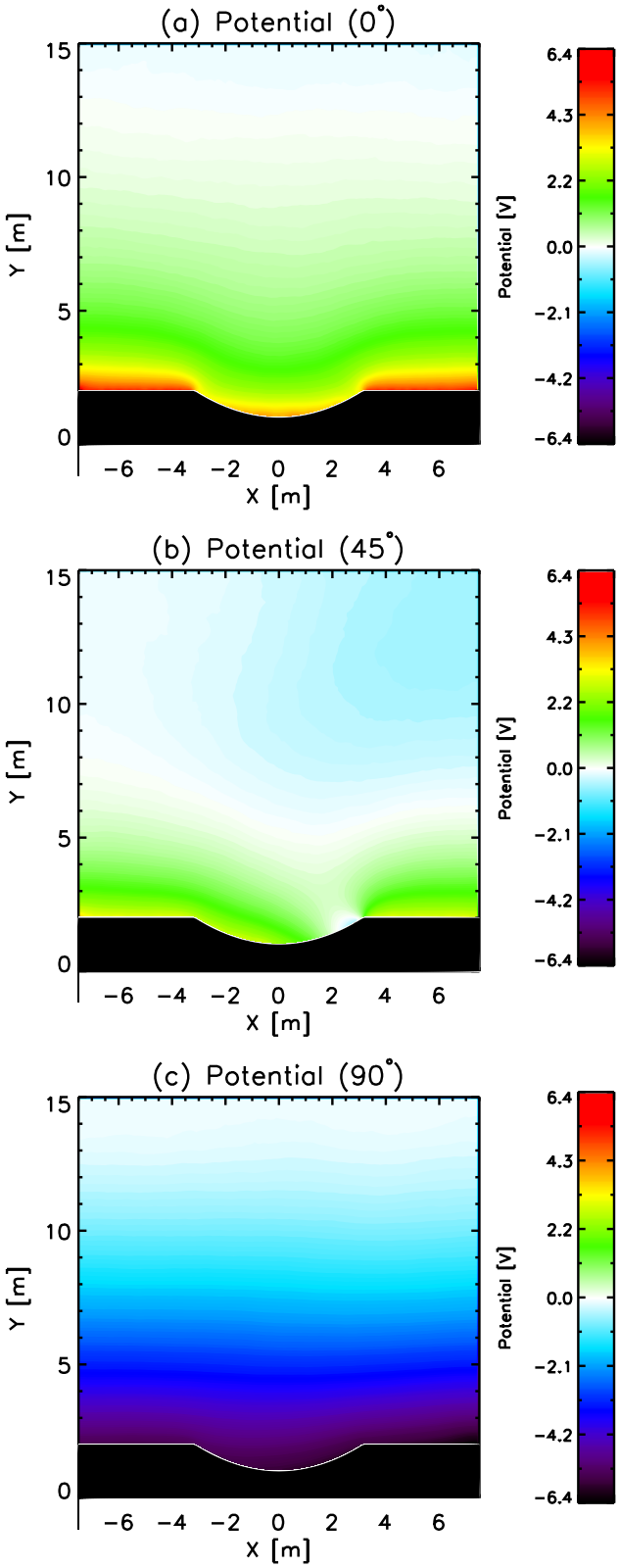

Figure 2.16: The potential above a lunar crater for three cases of the solar wind / UV incidence: (a) 0°; (b) 45°; (c) 90°.

photoemission from the sloped surfaces. For the 45° case, a more complex potential environment is present due to increasingly different photoemission levels from the surface. While none of the surface is directly shadowed for this topography, part of the leeward side of the crater surface has actually charged negatively as the comparatively high photoemission from neighboring areas overwhelms the meager photoemission in this area. Finally, for the 90° case, the surface has no photoemission and correspondingly charges negative due to the collection of solar wind electrons.

The horizontal variation of the surface potential across the crater can also be explored with these simulations. Figure 2.17 shows the surface potential (following the crater surface) as a function of horizontal position for seven different values of the solar zenith angle (0° to 90° at 15° intervals). Over the entire range of solar zenith angles, the average surface potential is seen to progressively decrease, as expected from Figure 2.16. Additionally, the effect of the surface topography is also readily evident by examining the potential within the crater. For $\alpha < 60°$, decreasing solar zenith angle causes a decrease in the surface potential on the leeward side ($0 < x < 3$ m) faster than on the windward side ($-3 < x < 0$ m) of the crater. The decreasing photoemission from the leeward side, especially relative to the windward side, whose photoemission actually increases initially as the sun is more normal to the surface, causes the significant drop in surface potential. This dichotomy reaches a maximum around $\alpha = 75°$, where the surface potential across the crater is antisymmetric, with the windward potential even greater than the surface potential outside the crater. These simulations of (relatively) simple surface topographies have begun to show the complexity that can arise in the near-surface plasma environment due to surface topography. Future work will focus on other geophysically relevant topographies, including the presence of various-sized lunar boulders or crater rims.

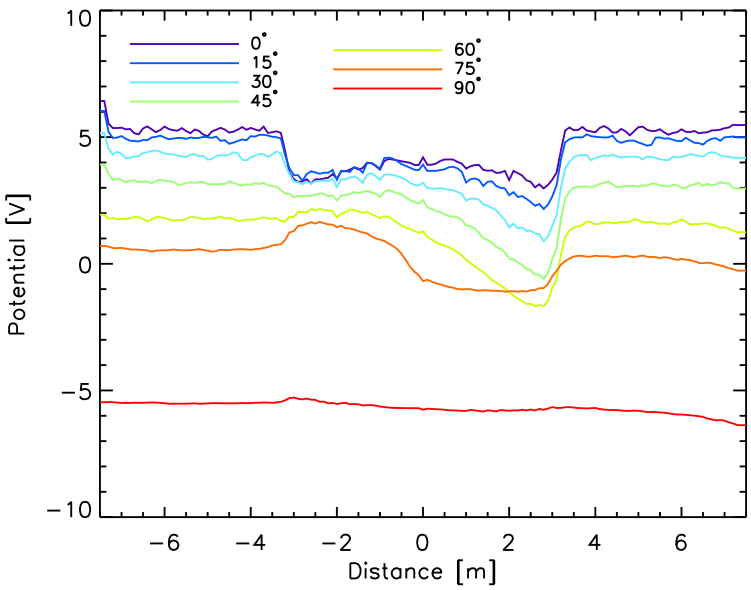

Figure 2.17: The surface potential as a function of horizontal distance along the crater surface (shown in Figure 2.16) for solar zenith angles ranging from 0° to 90°. As the sun sets, the leeward side of the crater (approximately $0 < x < 3$ m), becomes increasingly negative. For large values of the solar zenith angle ($\alpha > 75°$), the entire surface potential rapidly becomes negative.

Chapter 3

Comparison with Theory

Previous work has addressed the physical characteristics of photoelectron sheaths with applications to planetary bodies and spacecraft. Theoretical and simulation studies have focused on the role of different photoelectron velocity distributions in determining the sheath characteristics, with a drifting Maxwellian ambient plasma, typical of the solar wind [*Guernsey and Fu*, 1970; *Fu*, 1971; *Nitter et al.*, 1998; *Poppe and Horányi*, 2010]. The photoelectron distributions studied included a Fermi distribution ($f(v) \propto v$), a Maxwellian distribution ($f(v) \propto e^{-v^2}$) and an experimentally measured distribution for lunar dust ($f(v) \propto v^4 e^{-v^4}$ [*Feuerbacher et al.*, 1972]) and found differing sheath potential and density profiles above the photoemitting surface. Previous analytical work with Fermi and Maxwellian photoelectron distributions predicted the presence of non-monotonic potentials [*Guernsey and Fu*, 1970; *Fu*, 1971; *Nitter et al.*, 1998] and recent simulations of Maxwellian and lunar dust photoelectron distributions have shown not only the existence of non-monotonic potentials, but also the energetic preferability of non-monotonic structures over the corresponding monotonic solution [*Poppe and Horányi*, 2010; *Ergun et al.*, 2010]. Additionally, analysis of Lunar Prospector (LP) Electron Reflectometry (ER) data has identified observations of stable non-monotonic potentials above the dayside lunar surface during periods when the Moon was exposed to the terrestrial plasma sheet (see Chapter 4 and *Poppe et al.* [2011]). These observations point to the ubiquity of non-monotonic potentials above photoemitting surfaces in space and indicate the need for further theoretical work in order to understand the structure, stability and variability of non-monotonic potentials.

In this Chapter, we consider theoretical descriptions of photoelectron sheaths in a wide variety of environments and compare this analysis to results from the one-dimensional PIC code. Furthermore, we extend a previous analytic theory of photoelectron sheaths to include the effect of solar wind electron κ-distributions. Finally, we outline future areas of theoretical investigation that would strengthen our understanding of photoelectron sheaths throughout the solar system.

3.1 Kinetic Derivation - Maxwellian Solar Wind

Previous work has addressed the nature of photoelectron sheaths immersed in an ambient plasma using kinetic theory [*Guernsey and Fu*, 1970; *Nitter et al.*, 1998]. The derivations used specified velocity distributions for both the photoelectrons and solar wind electrons, combined with several boundary conditions to solve for the potential structure of the system. Both analyses found that non-monotonic potentials exist for two different photoelectron velocity distributions: a Fermi distribution and a Maxwellian. First, we compare theoretical results from the Maxwellian case to results from the 1-dimensional PIC code in order to validate the code with the inclusion of the solar wind [*Nitter et al.*, 1998].

Similar to *Nitter et al.* [1998], we assume the following conditions for our analysis of Maxwellian photoelectron sheaths:

(1) the ions form a cold, supersonic beam with drift velocity, v_d, large enough to overcome any electrostatic potential barriers ($v_d \gg \sqrt{qV_o/m_i}$);

(2) the photoelectrons and solar wind electrons are half-Maxwellians with temperature, T_{ph} and T_{sw}, respectively;

(3) the plasma is quasi-neutral at infinity;

(4) the sheath is in a steady-state with no net current flow;

(5) the sheath electric field is zero at infinity; and,

(6) the sheath solutions are either monotonically positive or non-monotonic. Monotonically negative sheath solutions are predicted to exist for various other *in-situ* environments; however, we do not consider this situation at this time.

The photoelectron and solar wind electron velocity distributions, $f_{ph}(0,v)$ and $f_{sw}(\infty,v)$, at the plate and infinity, respectively, are given by:

$$f_{ph}(0,v) = n_{ph}\sqrt{\frac{m_e}{2\pi k T_{ph}}}\exp\left(-\frac{v^2}{2v_{ph}^2}\right), \tag{3.1}$$

and

$$f_{sw}(\infty,v) = n_{sw}\sqrt{\frac{m_e}{2\pi k T_{sw}}}\exp\left(-\frac{v^2}{2v_{sw}^2}\right), \tag{3.2}$$

where n_{ph} and n_{sw} are the photoelectron and solar wind electron densities at the plate and infinity, respectively, v_{ph} and v_{sw} are the photoelectron and solar wind electron thermal velocities, m_e is the electron mass and k is Boltzmann's constant.

We start with Equations 9, 10 and 15 from *Nitter et al.* [1998], corresponding to the third through fifth assumptions above, with the sole modification that we do not allow an angular dependence in the solar wind flow at this time. Defining a normalized potential, $Y_j = eV_j/kT_{ph}$, where $j = \{o,m\}$, representing the wall and minimum potentials, respectively, we can express the three conditions as:

$$0 = n_{ph}e^{-Y_o}\left(1 - \mathrm{Erf}\sqrt{-Y_m}\right) + n_{sw}\left(1 + \mathrm{Erf}\sqrt{-Y_m/\alpha}\right) - 2n_i, \tag{3.3}$$

$$0 = n_{ph}e^{Y_m - Y_o} - n_{sw}\alpha^{1/2}\exp(Y_m/\alpha) + n_i\sqrt{\frac{2\pi\alpha m_e}{m_i}}M, \tag{3.4}$$

and,

$$\begin{aligned} 0 \;=\; & n_{ph}e^{-Y_o}\left[1 - \mathrm{Erf}\sqrt{-Y_m} - \left(1 - \frac{2}{\sqrt{\pi}}\sqrt{-Y_m}\right)\right] \\ & + n_{sw}\alpha\left[1 + \mathrm{Erf}\sqrt{-\frac{Y_m}{\alpha}} - \left(1 + \frac{2}{\sqrt{\pi}}\sqrt{-\frac{Y_m}{\alpha}}\right)e^{Y_m/\alpha}\right] \\ & + 2n_i\alpha M^2\left[1 - \sqrt{1 - \frac{2Y_m}{\alpha M^2}}\right], \end{aligned} \tag{3.5}$$

where $\alpha = T_{sw}/T_{ph}$, $M = v_i/u_B$ is the Mach number and $u_B = \sqrt{kT_{sw}/m_i}$ is the Bohm velocity. The three unknown variables in the above set of equations are the solar wind electron density at infinity, n_{sw}, the wall potential, Y_o, and the minimum potential, Y_m. Equation 3.3 can be straightforwardly used to eliminate the solar wind electron density at infinity, n_{sw}, from Equations 3.4 and 3.5. This yields a set of two coupled, non-linear equations for two unknowns, Y_o and Y_m. Given the five parameters, T_{ph}, T_{sw}, M, n_{ph} and n_i, a solution for Y_o and Y_m can be numerically calculated. Shown in Figure 3.1 is the range of existence for both types of solutions in the basic lunar case of $M \approx 3$ (with $m_i = 100\ m_e$ in order to compare to the PIC code), $n_{ph} = 1.0 \times 10^8$ m^{-3} and $n_i = 10^7$ m^{-3}. The Mach number for this case, $M \approx 3$, corresponds to a solar wind ion beam with a drift speed of 400 km s^{-1}, standard for the solar wind. Monotonic solutions exist for all values of $T_{sw} > 1.43$, regardless of T_{ph}, while non-monotonic solutions have an existence cutoff in T_{sw} dependent on T_{ph}. In the region where both monotonic and non-monotonic solutions exist, it has been suggested that the non-monotonic solution is energetically preferable to the monotonic case and therefore, one would expect the potential to relax to the non-monotonic case [*Nitter et al.*, 1998].

3.1.1 Comparison of Theory and Simulation

We compare the theoretical and simulation results for the surface potential, V_o, the minimum potential, V_m and the non-monotonic potential drop, $V_{nm} \equiv V_o - V_m$, as a function of the solar wind temperature, T_{sw}, and the photoelectron temperature, T_{ph}, respectively. Shown in Figure 3.2 is the dependence of all three potentials on T_{sw}. As seen in both Figure 3.2(a) and 3.2(b), the theory and simulations agree well with each other and both show that the surface and minimum potentials decrease as the solar wind temperature increases. Additionally, the non-monotonic potential drop from the surface to the minimum is shown to be relatively constant over this range in T_{sw}. For $T_{sw} > \approx 80$ eV, it should be noted that the theoretical assumptions begin to break down, as the 400 km s^{-1} ion drift velocity becomes subsonic. This assumption was key to the kinetic theory derivation and therefore, the theory should not be extended further in T_{sw}. Nevertheless, the theory

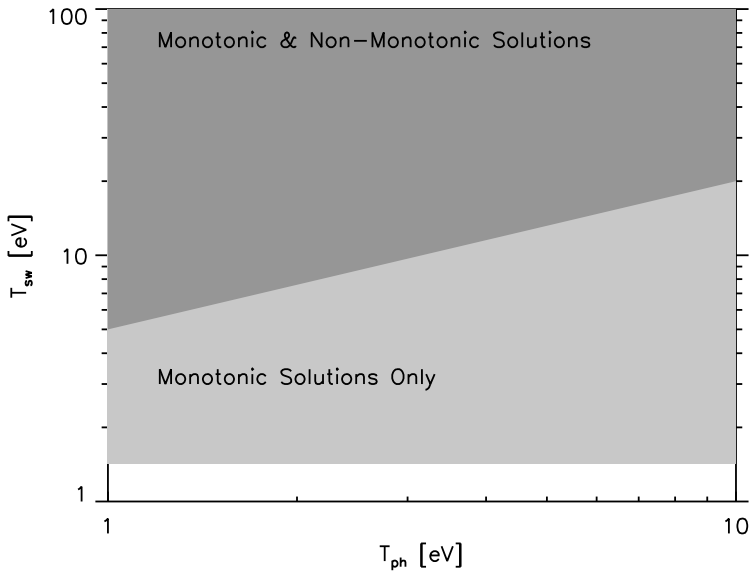

Figure 3.1: The existence of monotonic and non-monotonic potential structures in the T_{sw}-T_{ph} phasespace for typical lunar values of the other parameters ($n_{ph} = 1.3 \times 10^8$ m^{-3}, $n_{sw} = 10^7$ m^{-3}, $M \approx 3$).

and simulation results for the potentials show excellent agreement both in magnitude and slope as a function of T_{sw}.

The theory and simulation can also be compared as a function of the photoelectron temperature for $1 < T_{ph} < 10$ eV. While the comparison against the solar wind temperature, T_{sw}, was for a regime in which both monotonic and non-monotonic potentials are allowed according to Figure 3.1 ($T_{sw} > 10$ eV and $T_{ph} = 2.2$ eV), the photoelectron temperature is explored on a curve ($T_{sw} = 10$ eV) where for large enough T_{ph}, only monotonic solutions should exist. Therefore, we should expect the PIC results to switch from a non-monotonic to a monotonic sheath for large enough values of T_{ph}. Figure 3.3 shows the theoretical and simulation results for the surface potential as a function of T_{ph}. For the range where both solutions exist, the theoretical predictions for the monotonic and non-monotonic surface potentials are indistinguishable. In contrast, the simulation results show non-monotonic potentials exclusively for the range of photoelectron temperatures, $T_{ph} < 6$ eV, and monotonic potentials for larger temperatures. While the exact values of the surface potential and

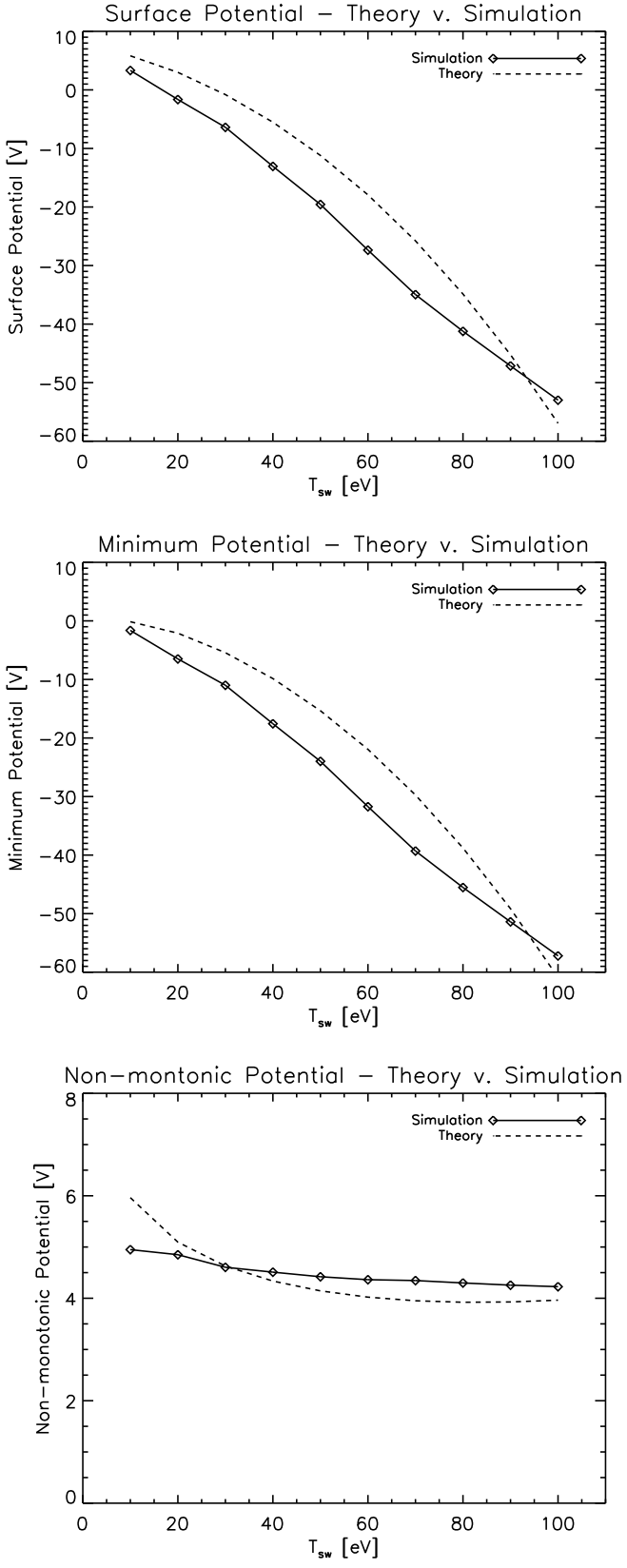

Figure 3.2: A comparison of simulation and theoretical results of the surface potential, V_o, the minimum potential, V_m, and the non-monotonic potential drop, $V_o - V_m$, versus the solar wind temperature, T_{sw}.

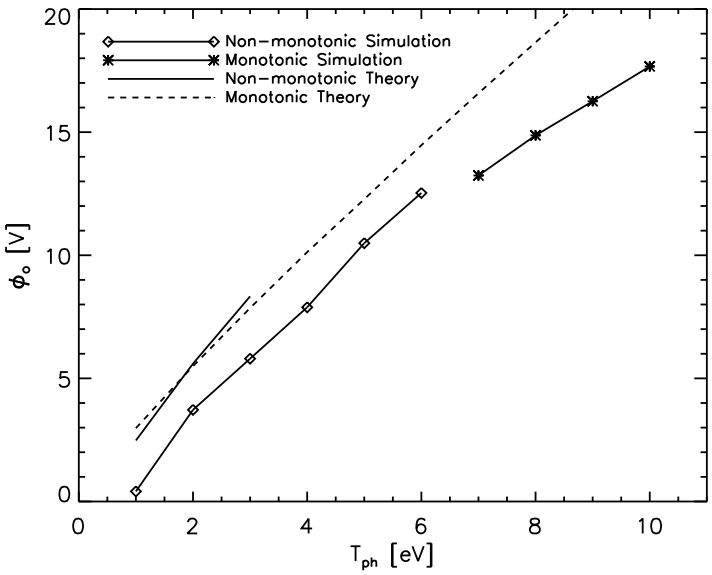

Figure 3.3: A comparison of simulation and theoretical results for the surface potential as a function of the photoelectron temperature, T_{ph}. The theory predicts simultaneous solutions for both monotonic and non-monotonic potentials for $T_{ph} < 3$ eV, while the simulation results predict non-monotonic potentials only for $T_{ph} < 6$ eV.

the photoelectron temperature at which the solution becomes monotonic differ slightly between the theory and the simulation, the agreement between the two curves is still good. The theory predicts that both types of potential solutions exist for low enough photoelectron temperatures, yet the simulation relaxes exclusively to the non-monotonic solution. As noted in previous work [*Guernsey and Fu*, 1970; *Nitter et al.*, 1998], this may be due to the non-monotonic solution being energetically preferable to the monotonic solution.

In summary, the theoretical and simulation results show agreement over a wide range of parameters, validating the PIC code for this situation. While the PIC code is advantageous for its easy applicability to a wide range of physical systems with minor modifications to the code, the theory presents an opportunity, once fully established, to extend results to a geophysically correct parameter space (namely, the ion mass). A combination of the two approaches to studying photoelectron sheaths yields a deeper understanding of the physics involved.

3.2 Kinetic Derivation - κ-Distribution Solar Wind

While previous work has mainly focused on the role of the photoelectron distribution and current in determining the sheath characteristics, further work is needed to understand the role played by the ambient plasma distribution. Typically, the solar wind has been used as a model for the ambient plasma due to its geophysical relevance, with Maxwellian electron and ion distributions with temperatures, $T_e \approx T_i \approx 10$ eV, density, $n_{sw} \approx 10^7$ m^{-3} and drift speed, $v_d = 400$ km s^{-1}. *In-situ* measurements of a variety of space plasmas, including the solar wind and the terrestrial geomagnetic tail and plasma sheet, have shown that electron distributions are best represented by κ-distributions, rather than Maxwellians [*Vasyliunas*, 1971; *Slavin et al.*, 1985; *Christon et al.*, 1988, 1989; *Halekas et al.*, 2005b]. A κ-distribution has an increased tail and decreased core population with respect to a Maxwellian, and for large energies, E, the distribution scales as $f \propto E^{-\kappa}$ [*Christon et al.*, 1988]. The analytic form of a κ-distribution is given by,

$$f_\kappa(v) = \frac{\Gamma(\kappa+1)}{(\pi\kappa)^{3/2}\Gamma(\kappa-1/2)}\frac{n_o}{\theta^3}\left[1+\frac{v^2}{\kappa\theta^2}\right]^{-(\kappa+1)} \tag{3.6}$$

$$= n_o A_\kappa \left[1+\frac{1}{\kappa\theta^2}(v_x^2+v_y^2+v_z^2)\right]^{-(\kappa+1)}, \tag{3.7}$$

where,

$$A_\kappa = \frac{\Gamma(\kappa+1)}{(\pi\kappa)^{3/2}\Gamma(\kappa-1/2)}\frac{1}{\theta^3}, \tag{3.8}$$

n_o is the density, θ is the average thermal velocity and κ is the spectral index. One can also define the κ-distribution temperature, roughly equivalent to its Maxwellian counterpart, as,

$$kT_{sw}^\kappa = \frac{\kappa}{(\kappa-3/2)}\frac{m\theta^2}{2}. \tag{3.9}$$

In the limit, $\kappa \to \infty$, the distribution returns to a Maxwellian, which provides a convenient method of validating theoretical results including κ-distributions with previous analytic work. Figure 3.4 shows the κ-distribution for a set of κ values to illustrate the characteristics of the distribution. Additionally, a Maxwellian distribution with equivalent temperature is shown as a comparison for the limit, $\kappa \to \infty$.

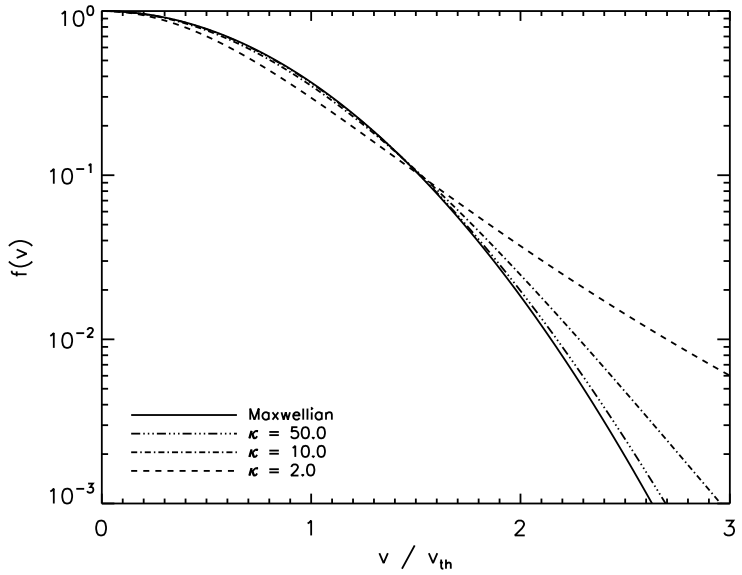

Figure 3.4: A comparison of the Maxwellian and κ-distributions for various values of κ.

3.2.1 Distributions

3.2.1.1 κ-Solar Wind Distribution

The presence of an electric potential throughout the photoelectron sheath will modify the various distributions and thus, in order to evaluate the necessary integrals for the boundary conditions, the distributions must be modified to take this into account. Assuming the potential variation is one-dimensional in the x-direction, conservation of energy gives,

$$\frac{1}{2}mv_x(\infty)^2 - eV(\infty) = \frac{1}{2}mv_x(x)^2 - eV(x), \tag{3.10}$$

where $V(x)$ is the electric potential at the position x. Solving for $v_x(\infty)^2$ gives,

$$v_x(\infty)^2 = v_x(x)^2 - \frac{2e}{m}(V(x) - V(\infty)). \tag{3.11}$$

Thus, the solar wind distribution at any point in space, x, is given by,

$$\begin{aligned} f_\kappa(x,v) &= n_o A_\kappa \left[1 + \frac{1}{\kappa\theta^2}\left(v_x(x)^2 - \frac{2e}{m}\left(V(x) - V(\infty)\right)\right) + \frac{1}{\kappa\theta^2}(v_y^2 + v_z^2)\right]^{-(\kappa+1)} \\ &= n_o A_\kappa \left[1 + \frac{1}{\kappa\theta^2}(v_x(x)^2 + v_y^2 + v_z^2) - \frac{2e}{\kappa\theta^2 m}\left(V(x) - V(\infty)\right)\right]^{-(\kappa+1)}. \end{aligned} \tag{3.12}$$

3.2.1.2 Photoelectron Distribution

The photoelectron distribution is assumed to be Maxwellian, and thus, similar to the solar wind, the distribution of photoelectrons at any point in space is given by,

$$f_{ph}(x,v) = n_{ph,o}\left(\frac{m}{2\pi kT_{ph}}\right)^{3/2}\exp\left[-\frac{mv^2}{2kT_{ph}} + \frac{e(V(x)-V_o)}{kT_{ph}}\right], \tag{3.13}$$

where $n_{ph,o}$ is the photoelectron density at the surface, T_{ph} is the photoelectron temperature and V_o is the surface potential.

3.2.1.3 Ions

The ion population in the solar wind is a cold, supersonic beam and therefore, ion continuity and energy conservation can be used to determine the density at any point in space,

$$n_i(x) = n_i(\infty)\left[1 - \frac{2eV(x)}{m_i u_i(\infty)^2}\right]^{-1/2}. \tag{3.14}$$

3.2.2 Conditions

Nitter et al. [1998] identified three conditions that could be simultaneously solved for the minimum and wall potentials of the photoelectron sheath. In summary, the first two conditions, neutrality and zero net current at infinity are,

$$n^{\kappa}_{sw}(\infty) + n_{ph}(\infty) = n_i(\infty), \tag{3.15}$$

and

$$\int_{v_m(0)}^{\infty}\int_{-\infty}^{\infty}\int_{-\infty}^{\infty} v_x f_{ph}(0,v)dv + \int_{-\infty}^{-v_m(\infty)}\int_{-\infty}^{\infty}\int_{-\infty}^{\infty} v_x f_{\kappa}(\infty,v)dv - n_i(\infty)v_i(\infty) = 0, \tag{3.16}$$

where n^{κ}_{sw}, n_{ph}, n_i are the solar wind, photoelectron and ion densities, respectively, f_{ph}, f_{κ} are the photoelectron and solar wind distributions, respectively, and $v_m(x)$ is the velocity required to overcome the non-monotonic potential barrier from any point in space, x, defined as,

$$v_m(x) = \sqrt{\frac{2e(V(x)-V_m)}{m}}. \tag{3.17}$$

Additionally, using the surface potential, $V(x=0)=V_o$ and the potential at infinity, $V(x=\infty)=V_\infty \equiv 0$, we can define two specific values of v_m that will recur throughout the analysis,

$$v_m(0) = \sqrt{\frac{2e(V_o - V_m)}{m}} \tag{3.18}$$

$$v_m(\infty) = \sqrt{\frac{-2eV_m}{m}}. \tag{3.19}$$

3.2.2.1 Condition 1: Quasineutrality at Infinity

The first condition stipulates that the density at $x=\infty$ must be quasineutral. Below, we derive the density at infinity for all three species (photoelectrons, solar wind electron, and solar wind ions) to establish the quasineutrality condition.

κ-Solar Wind Electrons

The density of the solar wind electrons can be derived using distribution given in Equation 3.12, recognizing that for non-monotonic potentials, there must be two different integrals over the velocity, representing free solar wind electrons ($v > v_m$, where v_m is the minimum velocity needed to overcome the non-monotonic potential barrier) and captured solar wind electrons that do not overcome the potential barrier and are reflected back to infinity ($v < v_m$). The density for free and captured solar wind electrons are given by,

$$n^\kappa_{free}(x) = \int_{-\infty}^{\infty} dv_y dv_z \int_{v_m(x)}^{\infty} f_\kappa(x,v) dv_x, \tag{3.20}$$

and,

$$\begin{aligned} n^\kappa_{capt}(x) &= \int_{-\infty}^{\infty}\int_{-\infty}^{\infty} dv_y dv_z \int_{-v_m(x)}^{v_m(x)} f_\kappa(x,v) dv_x \\ &= 2\int_{-\infty}^{\infty}\int_{-\infty}^{\infty} dv_y dv_z \int_{0}^{v_m(x)} f_\kappa(x,v) dv_x, \end{aligned} \tag{3.21}$$

respectively, where we have condensed the integral over v_x from $[-v_m(x), v_m(x)]$ to $[0, v_m(x)]$ due to the even-ness of the integrand.

The density for heights greater than the non-monotonic potential minimum ($x > x_m$) is given by the sum of the free and captured densities,

$$n_\kappa(x) = \int_{-\infty}^{\infty}\int_{-\infty}^{\infty} dv_y dv_z \int_{-v_m(x)}^{\infty} f_\kappa(x,v) dv_x. \tag{3.22}$$

After integrating over $[-\infty, \infty]$ in both v_y and v_z, we then break up the integral over v_x into two regions, $[0, \infty]$ and $[0, v_m(x)]$, (where the second region is allowable since the integral is even), to allow for easier calculation of the integral. The integral over the first set of bounds is,

$$\begin{aligned}
\int_0^\infty f_\kappa(x, v_x) dv_x &= A_\kappa n_o \pi \theta^2 \left(\frac{1}{\theta^2 \kappa}\right)^{-\kappa} \sqrt{\pi} \left(\frac{m}{-2eV(x) + m\theta^2\kappa}\right)^{\kappa - 1/2} \frac{\Gamma(\kappa - 1/2)}{2\Gamma(\kappa)} \\
&= A_\kappa n_o \pi \theta^2 \left(\frac{1}{\theta^2 \kappa}\right)^{-\kappa} \sqrt{\pi} \frac{\Gamma(\kappa - 1/2)}{2\Gamma(\kappa)} \left(\theta^2\kappa - \frac{2eV(x)}{m}\right)^{-(\kappa - 1/2)} \\
&= \frac{n_o}{2} \left[1 - \frac{2eV(x)}{\theta^2 \kappa m}\right]^{-(\kappa - 1/2)}. \qquad (3.23)
\end{aligned}$$

The integral over the second set of bounds ($[0, v_m(x)]$) is given by,

$$\begin{aligned}
\int_0^{v_m(x)} f_\kappa(x, v_x) dv_x &= A_\kappa n_o \pi \theta^2 \left(\frac{1}{\theta^2 \kappa}\right)^{-\kappa} v_m \left(\frac{m}{m v_m^2 - 2eV(x) + m\theta^2\kappa}\right)^{\kappa} \times \\
&\quad \times \left(1 + \frac{m v_m^2}{-2eV(x) + m\theta^2\kappa}\right)^{\kappa} {}_2F_1\left[\frac{1}{2}, \kappa; \frac{3}{2}; \frac{m v_m^2}{2eV(x) - m\theta^2\kappa}\right] \\
&= A_\kappa n_o \pi \theta^2 (\theta^2\kappa)^\kappa v_m \left(-\frac{2eV(x)}{m} + \theta^2\kappa\right)^{-\kappa} \times \\
&\quad \times {}_2F_1\left[\frac{1}{2}, \kappa; \frac{3}{2}; \frac{m v_m^2}{2eV(x) - m\theta^2\kappa}\right] \\
&= A_\kappa n_o \pi \theta^2 v_m \left(1 - \frac{2eV(x)}{m\theta^2\kappa}\right)^{-\kappa} \times \\
&\quad \times {}_2F_1\left[\frac{1}{2}, \kappa; \frac{3}{2}; \frac{m v_m^2}{2eV(x) - m\theta^2\kappa}\right], \qquad (3.24)
\end{aligned}$$

where ${}_2F_1[a, b; c; z]$ is the hypergeometric function of the second kind. The hypergeometric function of the second kind is convergent for argument, $|z| < 1$, and is shown in Figure 3.5 for values typical in this derivation. Thus, the net density for the solar wind electrons for heights greater than the potential barrier is given by the sum of the two integrals,

$$\begin{aligned}
n_{sw}^\kappa(x > x_m) &= \frac{n_o}{2} \left[1 - \frac{2eV(x)}{\theta^2 \kappa m}\right]^{-(\kappa - 1/2)} + A_\kappa n_o \pi \theta^2 v_m \left(1 - \frac{2eV(x)}{m\theta^2\kappa}\right)^{-\kappa} \times \\
&\quad \times {}_2F_1\left[\frac{1}{2}, \kappa; \frac{3}{2}; \frac{m v_m^2}{2eV(x) - m\theta^2\kappa}\right]. \qquad (3.25)
\end{aligned}$$

Here, we define the following normalized variables (similar to *Nitter et al.* [1998]),

$$Y(x) \equiv \frac{eV(x)}{kT_{ph}}, \tag{3.26}$$

$$Y_m \equiv \frac{eV_m}{kT_{ph}}, \tag{3.27}$$

$$Y_o \equiv \frac{eV_o}{kT_{ph}}, \tag{3.28}$$

$$\alpha_\kappa \equiv \frac{kT_{ph}}{(\kappa - 3/2)kT_{sw}^\kappa}. \tag{3.29}$$

The density can then be expressed as,

$$\begin{aligned} n_{sw}^\kappa(x > x_m) &= \frac{n_o}{2}\left[1 - \alpha_\kappa Y(x)\right]^{-(\kappa-1/2)} + \\ &+ \frac{n_o}{\sqrt{\pi}}\frac{\Gamma(\kappa)}{\Gamma(\kappa-1/2)}\sqrt{\alpha_\kappa(Y(x)-Y_m)}\left[1-\alpha_\kappa Y(x)\right]^{-\kappa} \times \\ &\times {}_2F_1\left[\frac{1}{2}, \kappa; \frac{3}{2}; \frac{\alpha_\kappa(Y(x)-Y_m)}{\alpha_\kappa Y(x) - 1}\right]. \end{aligned} \tag{3.30}$$

Specifically, the density at $x = \infty$, where we define $Y(x = \infty) = 0$, is given by,

$$n_{sw}^\kappa(x=\infty) = \frac{n_o}{2} + \frac{n_o}{\sqrt{\pi}}\frac{\Gamma(\kappa)}{\Gamma(\kappa-1/2)}\sqrt{-\alpha_\kappa Y_m}\ {}_2F_1\left[\frac{1}{2}, \kappa; \frac{3}{2}; \alpha_\kappa Y_m\right]. \tag{3.31}$$

For later ease of evaluation, we use a linear transform for the hypergeometric equation (Equation 15.3.5 in *Abramowitz and Stegun* [1970]),

$${}_2F_1[a, b; c; z] = (1-z)^{-b}\ {}_2F_1\left[b, c-a; c; \frac{z}{z-1}\right], \tag{3.32}$$

which gives,

$$n_{sw}^\kappa(x=\infty) = \frac{n_o}{2} + \frac{n_o}{\sqrt{\pi}}\frac{\Gamma(\kappa)}{\Gamma(\kappa-1/2)}\sqrt{-\alpha_\kappa Y_m}(1-\alpha_\kappa Y_m)^{-\kappa}\ {}_2F_1\left[\kappa, 1; \frac{3}{2}; \frac{\alpha_\kappa Y_m}{\alpha_\kappa Y_m - 1}\right]. \tag{3.33}$$

Photoelectrons

The densities of captured and free photoelectrons for a Maxwellian distribution were derived previously [*Nitter et al.*, 1998], and are given by,

$$n_{ph}^{free}(x) = \frac{n_{ph,o}}{2}\exp\left(\frac{e(V(x)-V_o)}{kT_{ph}}\right) \times \left[1 - \mathrm{Erf}\left(\frac{e(V(x)-V_m)}{kT_{ph}}\right)^{1/2}\right], \tag{3.34}$$

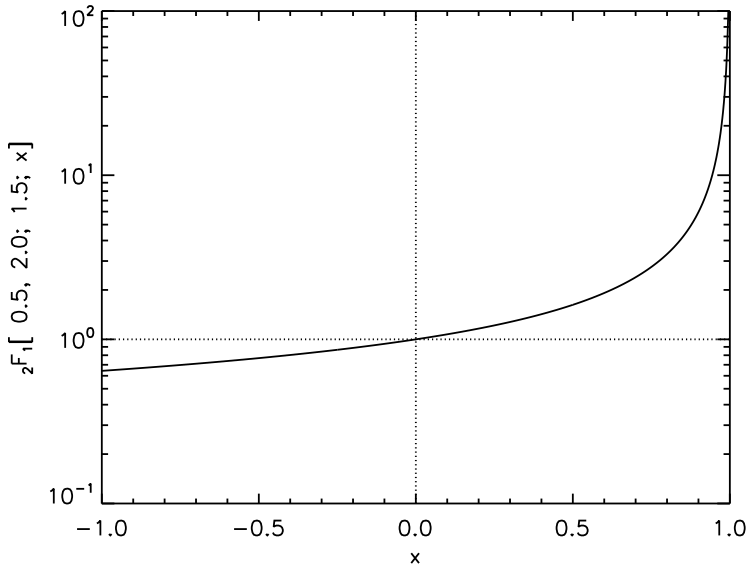

Figure 3.5: The hypergeometric function of the second kind, ${}_2F_1[0.5, 2.0; 1.5; x]$, for $-1 < x < 1$.

and,

$$n_{ph}^{capt}(x) = n_{ph,o} \exp\left(\frac{e(V(x) - V_o)}{kT_{ph}}\right) \text{Erf}\left(\frac{e(V(x) - V_m)}{kT_{ph}}\right)^{1/2}, \tag{3.35}$$

respectively. Defining this in terms of the normalized variables gives,

$$n_{ph}^{free}(x) = \frac{n_{ph,o}}{2} e^{Y(x)-Y_o} \left[1 - \text{Erf}(Y(x) - Y_m)^{1/2}\right], \tag{3.36}$$

and

$$n_{ph}^{capt}(x) = n_{ph,o} e^{Y(x)-Y_o} \text{Erf}(Y(x) - Y_m)^{1/2}. \tag{3.37}$$

The density at $x = \infty$ is then given by,

$$n_{ph}(\infty) = n_{ph}^{free}(\infty) = \frac{n_{ph,o}}{2} e^{-Y_o} \left[1 - \text{Erf}(-Y_m)^{1/2}\right]. \tag{3.38}$$

Ions

Converting the ion density from Equation 3.14 into normalized variables, and using a modified definition of the Bohm sheath velocity for κ-distributions,

$$v_B^\kappa = \sqrt{\frac{(\kappa - 3/2)kT_{sw}^\kappa}{m_i}}, \tag{3.39}$$

gives,

$$n_i(x) = n_i(\infty)\left[1 - \frac{2{v_B^\kappa}^2}{u_i(\infty)^2}\alpha_\kappa Y(x)\right]^{-1/2}. \tag{3.40}$$

Defining the Mach number for the κ-distribution as,

$$M_\kappa = \frac{u_i(\infty)}{v_B^\kappa}, \tag{3.41}$$

gives,

$$n_i(x) = n_i(\infty)\left[1 - \frac{2\alpha_\kappa Y(x)}{M_\kappa^2}\right]^{-1/2}. \tag{3.42}$$

Final Form of Condition 1

Using the form of the density condition,

$$n_{sw}^\kappa(\infty) + n_{ph}(\infty) = n_i(\infty), \tag{3.43}$$

and inserting the densities for the solar wind ions, electrons and photoelectrons at $x = \infty$ gives,

$$\begin{aligned} n_i(\infty) &= \frac{n_o}{2} + \frac{n_o}{\sqrt{\pi}}\frac{\Gamma(\kappa)}{\Gamma(\kappa - 1/2)}\sqrt{-\alpha_\kappa Y_m}(1 - \alpha_\kappa Y_m)^{-\kappa}\ {}_2F_1\left[\kappa, 1; \frac{3}{2}; \frac{\alpha_\kappa Y_m}{\alpha_\kappa Y_m - 1}\right] + \\ &\quad + \frac{n_{ph,o}}{2}e^{-Y_o}\left[1 - \mathrm{Erf}(-Y_m)^{1/2}\right]. \end{aligned} \tag{3.44}$$

3.2.2.2 Condition 2: Zero Net Current at Infinity

The second condition states that the sheath must have no net current at infinity, $J_i(\infty) + J_{ph}(\infty) + J_{sw}^\kappa(\infty) = 0$. Below, we calculate the current term for each population and combine these to form the second condition.

Solar Wind Electrons

The solar wind electron current at infinity, $J_{sw}^\kappa(\infty)$, is given by,

$$J_{sw}^\kappa(\infty) = \int_{-\infty}^{\infty}\int_{-\infty}^{\infty} dv_y dv_z \int_{-\infty}^{-v_m(\infty)} v_x f_\kappa(\infty, v) dv_x, \tag{3.45}$$

where v_x is the velocity in the x-direction. The integral is only taken from $[-\infty, -v_m(\infty)]$, as any solar wind electrons with $|v| < |v_m(\infty)|$ will be reflected back to infinity by the sheath potential

and contribute no net current. Using Mathematica, this is integrated to be,

$$\begin{aligned} &= -A_\kappa n_o \pi \theta^2 \left(\frac{1}{\theta^2 \kappa}\right)^{-\kappa} \frac{1}{2(\kappa-1)} \left(v_m(\infty)^2 + \theta^2 \kappa\right)^{-(\kappa-1)} \\ &= -\frac{A_\kappa n_o \pi}{2(\kappa-1)} \theta^4 \kappa \left(1 + \frac{v_m(\infty)^2}{\theta^2 \kappa}\right)^{-(\kappa-1)} . \end{aligned} \tag{3.46}$$

Substituting for A_κ (Eq. 3.8) and $v_m(\infty)$ (Eq. 3.19) gives,

$$= -\frac{\Gamma(\kappa+1)}{2\sqrt{\kappa}(\kappa-1)\Gamma(\kappa-1/2)} \frac{\theta n_o}{\sqrt{\pi}} \left[1 - \frac{2eV_m}{m\theta^2\kappa}\right]^{-(\kappa-1)} . \tag{3.47}$$

Re-writing in terms of normalized variables gives,

$$J_{sw}^{\kappa}(\infty) = -\frac{n_o}{\sqrt{2\pi}} \frac{1}{\kappa-1} \frac{\Gamma(\kappa)}{\Gamma(\kappa-1/2)} \sqrt{\frac{(\kappa-3/2)kT_{sw}^{\kappa}}{m}} \left[1 - \alpha_\kappa Y_m\right]^{-(\kappa-1)} , \tag{3.48}$$

as the solar wind electron current at infinity.

Photoelectrons

The photoelectron current at infinity, $J_{ph}(\infty)$, is given by *Nitter et al.* [1998],

$$\begin{aligned} J_{ph}(\infty) = \int_{v_m(0)}^{\infty} \int_{-\infty}^{\infty} \int_{-\infty}^{\infty} v_x f_{ph}(0,v) dv &= \frac{n_{ph,o}}{\sqrt{2\pi}} \sqrt{\frac{kT_{ph}}{m}} \exp\left[\frac{e(V_m - V_o)}{kT_{ph}}\right] \\ &= \frac{n_{ph,o}}{\sqrt{2\pi}} \sqrt{\frac{kT_{ph}}{m}} \exp\left[Y_m - Y_o\right] . \end{aligned} \tag{3.49}$$

Final Form of Condition 2

Thus, including the ion current, $J_i = -n_i(\infty)u_i(\infty)$, the full condition for current neutrality at infinity becomes,

$$\begin{aligned} -n_i(\infty)u_i(\infty) &= \int_{v_m(0)}^{\infty} \int_{-\infty}^{\infty} \int_{-\infty}^{\infty} v_x f_{ph}(0,v) dv + \\ &\quad + \int_{-\infty}^{-v_m(\infty)} \int_{-\infty}^{\infty} \int_{-\infty}^{\infty} v_x f_{\kappa}(\infty,v) dv, \\ -n_i(\infty)u_i(\infty) &= \frac{n_{ph,o}}{\sqrt{2\pi}} \sqrt{\frac{kT_{ph}}{m}} \exp\left[\frac{e(V_m - V_o)}{kT_{ph}}\right] - \\ &\quad - \frac{\Gamma(\kappa+1)}{2\sqrt{\kappa}(\kappa-1)\Gamma(\kappa-1/2)} \frac{\theta n_o}{\sqrt{\pi}} \left[1 - \frac{2eV_m}{m\theta^2\kappa}\right]^{-(\kappa-1)} . \end{aligned} \tag{3.50}$$

Substituting for normalized variables and multiplying through by $\sqrt{m/kT_{ph}}$ gives,

$$\frac{n_{ph,o}}{\sqrt{2\pi}} e^{Y_m - Y_o} - \frac{n_o}{\sqrt{2\pi}(\kappa-1)} \frac{\Gamma(\kappa)}{\Gamma(\kappa-1/2)} \frac{1}{\sqrt{\alpha_\kappa}} \left(1 - \alpha_\kappa Y_m\right)^{-(\kappa-1)} + n_i \frac{M_\kappa}{\sqrt{\alpha_\kappa}} \sqrt{\frac{m_e}{m_i}} = 0. \tag{3.51}$$

3.2.2.3 Condition 3: Zero Electric Field at Infinity

The final boundary condition is given by mandating zero electric field at infinity. The electric field throughout the photoelectron sheath can be calculated by integrating Poisson's equation,

$$\frac{d^2V}{dx^2} = -\frac{e}{\epsilon_o}\left[n_i - n_{ph}^{free} - n_{ph}^{capt} - n_{sw}^{free} - n_{sw}^{capt}\right], \tag{3.52}$$

from $V = V_m$ to an arbitrary V using the boundary condition, $(dV/dx)(x_m) = 0$, where x_m is the location of the potential minimum [*Nitter et al.*, 1998]. After integration, Poisson's equation becomes,

$$\left(\frac{dV}{dx}\right)^2 = \int_{V_m}^{V} -\frac{2e}{\epsilon_o}\left[n_i(V') - n_{ph}^{free}(V') - n_{ph}^{capt}(V') - n_{sw}^{free}(V') - n_{sw}^{capt}(V')\right] dV'. \tag{3.53}$$

Since the integral for the boundary condition is for $x > x_m$, this implies that $n_{ph}^{capt} \equiv 0$. We can separate the four integrals that need to be performed for the condition above.

Ions

First, the ion term is given by,

$$\begin{aligned} -\frac{2e}{\epsilon_o}\int_{V_m}^{V} n_i(V)dV &= -\frac{2e}{\epsilon_o}\int_{V_m}^{V} n_i(\infty)\left[1 - \frac{2eV(x)}{m_i u_i(\infty)^2}\right]^{-1/2} dV \\ &= \frac{2m_i n_i(\infty)u_i(\infty)^2}{\epsilon_o}\sqrt{1 - \frac{2eV}{m_i u_i(\infty)^2}} - \\ &\quad -\frac{2m_i n_i(\infty)u_i(\infty)^2}{\epsilon_o}\sqrt{1 - \frac{2eV_m}{m_i u_i(\infty)^2}}. \end{aligned} \tag{3.54}$$

In terms of normalized variables, this reads,

$$= \frac{2(\kappa - 3/2)kT_{sw}^{\kappa}}{\epsilon_o} M_\kappa^2 n_i(\infty)\left[\sqrt{1 - \frac{2\alpha_\kappa Y(x)}{M_\kappa^2}} - \sqrt{1 - \frac{2\alpha_\kappa Y_m}{M_\kappa^2}}\right]. \tag{3.55}$$

Evaluating at $Y(x = \infty) \equiv 0$ gives,

$$= \frac{2(\kappa - 3/2)kT_{sw}^{\kappa}}{\epsilon_o} M_\kappa^2 n_i(\infty)\left[1 - \sqrt{1 - \frac{2\alpha_\kappa Y_m}{M_\kappa^2}}\right], \tag{3.56}$$

as the ion contribution to the electric field at infinity.

Photoelectrons

Next, the free photoelectron term is given by,

$$\begin{aligned}
-\frac{2e}{\epsilon_o}\int_{V_m}^{V} n_{ph}^{free}(V)dV &= -\frac{2e}{\epsilon_o}\int_{V_m}^{V}\frac{n_{ph,o}}{2}\exp\left(\frac{e(V(x)-V_o)}{kT_{ph}}\right)\times \\
&\quad\times\left[1-\mathrm{Erf}\left(\frac{e(V(x)-V_m)}{kT_{ph}}\right)^{1/2}\right]dV \\
&= -\frac{n_{ph,o}kT_{ph}}{\epsilon_o}\exp\left(\frac{e(V(x)-V_o)}{kT_{ph}}\right)\left(1-\mathrm{Erf}\left(\frac{e(V(x)-V_m)}{kT_{ph}}\right)^{1/2}\right)- \\
&\quad -\frac{n_{ph,o}kT_{ph}}{\epsilon_o}\exp\left(\frac{e(V_m-V_o)}{kT_{ph}}\right)\times \\
&\quad\times\left[\frac{2}{\sqrt{\pi}}\sqrt{\frac{e(V(x)-V_m)}{kT_{ph}}}-1\right] \qquad (3.57)
\end{aligned}$$

In normalized variables, this reads,

$$= -\frac{n_{ph,o}kT_{ph}}{\epsilon_o}\left[e^{Y(x)-Y_o}\left(1-\mathrm{Erf}\,\sqrt{Y(x)-Y_m}\right)+e^{Y_m-Y_o}\left(\frac{2}{\sqrt{\pi}}\sqrt{Y(x)-Y_m}-1\right)\right]. \qquad (3.58)$$

Evaluating at $Y(x=\infty)\equiv 0$ gives,

$$= -\frac{n_{ph,o}kT_{ph}}{\epsilon_o}\left[e^{-Y_o}\left(1-\mathrm{Erf}\,\sqrt{-Y_m}\right)+e^{Y_m-Y_o}\left(\frac{2}{\sqrt{\pi}}\sqrt{-Y_m}-1\right)\right]. \qquad (3.59)$$

Solar Wind Electrons

The net solar wind density for $x > x_m$ is given by,

$$\begin{aligned}
n_{sw}^{\kappa}(x>x_m) &= n_{sw}^{free}+n_{sw}^{capt} \\
&= \frac{n_o}{2}\left[1-\frac{2eV(x)}{\theta^2\kappa m}\right]^{-(\kappa-1/2)}+A_\kappa n_o\pi\theta^2 v_m\left(1-\frac{2eV(x)}{m\theta^2\kappa}\right)^{-\kappa}\times \\
&\quad\times {}_2F_1\left[\frac{1}{2},\kappa;\frac{3}{2};\frac{mv_m^2}{2eV(x)-m\theta^2\kappa}\right]. \qquad (3.60)
\end{aligned}$$

To ease integration, we first convert to normalized variables, which gives,

$$\begin{aligned}
n_{sw}^{\kappa}(x>x_m) &= \frac{n_o}{2}[1-\alpha_\kappa Y(x)]^{-(\kappa-1/2)}+ \\
&\quad+\frac{n_o}{\sqrt{\pi}}\frac{\Gamma(\kappa)}{\Gamma(\kappa-1/2)}\sqrt{\alpha_\kappa(Y(x)-Y_m)}\,[1-\alpha_\kappa Y(x)]^{-\kappa}\times \\
&\quad\times {}_2F_1\left[\frac{1}{2},\kappa;\frac{3}{2};\frac{\alpha_\kappa(Y(x)-Y_m)}{\alpha_\kappa Y(x)-1}\right]. \qquad (3.61)
\end{aligned}$$

Additionally, we simplify the function by again using an identity (Eq. 15.3.5 of *Abramowitz and Stegun* [1970]),

$$ {}_2F_1[a,b;c;z] = (1-z)^{-b}\ {}_2F_1\left[b, c-a; c, \frac{z}{z-1}\right], \tag{3.62} $$

which gives,

$$ \begin{aligned} n_{sw}^{\kappa}(x > x_m) &= \frac{n_o}{2}(1-\alpha_\kappa Y(x))^{-(\kappa-1/2)} + \\ &\quad + \frac{n_o}{\sqrt{\pi}}\frac{\Gamma(\kappa)}{\Gamma(\kappa-1/2)}(1-\alpha_\kappa Y_m)^{-\kappa}\sqrt{\alpha_\kappa(Y(x)-Y_m)}\times \\ &\quad \times\ {}_2F_1\left[\kappa, 1; \frac{3}{2}; \frac{\alpha_\kappa Y(x) - \alpha_\kappa Y_m}{1-\alpha_\kappa Y_m}\right]. \end{aligned} \tag{3.63} $$

The integral over the first term then becomes,

$$ \begin{aligned} &\frac{kT_{ph}}{e}\int_{Y_m}^{Y(x)} \frac{n_o}{2}\left[1-\alpha_\kappa Y(x)\right]^{-(\kappa-1/2)} dY = \\ &= -\frac{n_o}{2}\frac{kT_{ph}}{\alpha_\kappa e(\kappa-3/2)} \times \left[(1-\alpha_\kappa Y_m)^{3/2-\kappa} - (1-\alpha_\kappa Y(x))^{3/2-\kappa}\right] \end{aligned} \tag{3.64} $$

The integral over the second term is,

$$ \begin{aligned} &\frac{kT_{ph}}{e}\int_{Y_m}^{Y(x)} \frac{n_o}{\sqrt{\pi}}\frac{\Gamma(\kappa)}{\Gamma(\kappa-1/2)}(1-\alpha_\kappa Y_m)^{-\kappa}\sqrt{\alpha_\kappa(Y(x)-Y_m)}\times \\ &\qquad \times\ {}_2F_1\left[\kappa, 1; \frac{3}{2}; \frac{\alpha_\kappa Y(x) - \alpha_\kappa Y_m}{1-\alpha_\kappa Y_m}\right] dY = \\ &= \frac{2kT_{ph}}{3e}\frac{n_o\sqrt{\alpha_\kappa}}{\sqrt{\pi}}\frac{\Gamma(\kappa)}{\Gamma(\kappa-1/2)}(1-\alpha_\kappa Y_m)^{-\kappa}\times \\ &\qquad \times (Y(x)-Y_m)^{3/2}\ {}_2F_1\left[1, \kappa; \frac{5}{2}; \frac{\alpha_\kappa(Y(x)-Y_m)}{1-\alpha_\kappa Y_m}\right]. \end{aligned} \tag{3.65} $$

Thus, the total solar wind term is given by,

$$ \begin{aligned} &\frac{kT_{ph}}{e}\int_{Y_m}^{Y} n_{sw}^{\kappa}(x > x_m) dY = \\ &= -\frac{n_o}{2}\frac{kT_{ph}}{\alpha_\kappa e(\kappa-3/2)} \times \left[(1-\alpha_\kappa Y_m)^{3/2-\kappa} - (1-\alpha_\kappa Y(x))^{3/2-\kappa}\right] + \\ &\quad + \frac{2kT_{ph}}{3e}\frac{n_o\sqrt{\alpha_\kappa}}{\sqrt{\pi}}\frac{\Gamma(\kappa)}{\Gamma(\kappa-1/2)}(1-\alpha_\kappa Y_m)^{-\kappa}\times \\ &\quad \times (Y(x)-Y_m)^{3/2}\ {}_2F_1\left[1, \kappa; \frac{5}{2}; \frac{\alpha_\kappa(Y(x)-Y_m)}{1-\alpha_\kappa Y_m}\right]. \end{aligned} \tag{3.66} $$

Multiplying by the coefficient from Equation 3.53 ($-2e/\epsilon_o$) and evaluating at $Y(x=\infty)\equiv 0$ gives,

$$\begin{aligned}
&= \frac{n_o}{\epsilon_o}\frac{kT_{ph}}{\alpha_\kappa(\kappa-3/2)} \times \left[(1-\alpha_\kappa Y_m)^{3/2-\kappa}-1\right] - \\
&\quad -\frac{4kT_{ph}}{3\epsilon_o}\frac{n_o\sqrt{\alpha_\kappa}}{\sqrt{\pi}}\frac{\Gamma(\kappa)}{\Gamma(\kappa-1/2)}(1-\alpha_\kappa Y_m)^{-\kappa} \times \\
&\quad \times(-Y_m)^{3/2}\ {}_2F_1\left[1,\kappa;\frac{5}{2};\frac{\alpha_\kappa Y_m}{\alpha_\kappa Y_m-1}\right].
\end{aligned} \tag{3.67}$$

Final Form of Condition 3

Combining the three component terms gives the full condition for zero electric field at $x=\infty$,

$$\begin{aligned}
0 = &\frac{2M^2}{\alpha_\kappa}n_i(\infty)\left[1-\sqrt{1-\frac{2\alpha_\kappa Y_m}{M^2}}\right] + \\
&+ n_{ph,o}e^{-Y_o}\left[1-e^{Y_m}-\mathrm{Erf}(-Y_m)^{1/2}+\frac{2}{\sqrt{\pi}}e^{Y_m}\sqrt{-Y_m}\right] - \\
&-\frac{n_o}{\alpha_\kappa(\kappa-3/2)}\left[(1-\alpha_\kappa Y_m)^{3/2-\kappa}-1\right] + \\
&+\frac{4n_o}{3}\sqrt{\frac{\alpha_\kappa}{\pi}}\frac{\Gamma(\kappa)}{\Gamma(\kappa-1/2)}(1-\alpha_\kappa Y_m)^{-\kappa}(-Y_m)^{3/2}\ {}_2F_1\left[1,\kappa;\frac{5}{2};\frac{\alpha_\kappa Y_m}{\alpha_\kappa Y_m-1}\right].
\end{aligned} \tag{3.68}$$

3.2.2.4 Summary of Conditions

In summary, the three equations we have derived for the three unknowns, n_o, Y_o, and Y_m, are given by,

$$\begin{aligned}
n_i \;=\; &\frac{n_o}{2}+\frac{n_o}{\sqrt{\pi}}\frac{\Gamma(\kappa)}{\Gamma(\kappa-1/2)}\sqrt{-\alpha_\kappa Y_m}(1-\alpha_\kappa Y_m)^{-\kappa}\ {}_2F_1\left[\kappa,1;\frac{3}{2};\frac{\alpha_\kappa Y_m}{\alpha_\kappa Y_m-1}\right] + \\
&+\frac{n_{ph,o}}{2}e^{-Y_o}\left[1-\mathrm{Erf}(-Y_m)^{1/2}\right],
\end{aligned} \tag{3.69}$$

$$\frac{n_{ph,o}}{\sqrt{2\pi}}e^{Y_m-Y_o}-\frac{n_o}{\sqrt{2\pi}(\kappa-1)}\frac{\Gamma(\kappa)}{\Gamma(\kappa-1/2)}\frac{1}{\sqrt{\alpha_\kappa}}(1-\alpha_\kappa Y_m)^{-(\kappa-1)}+n_i\frac{M}{\sqrt{\alpha_\kappa}}\sqrt{\frac{m_e}{m_i}}=0, \tag{3.70}$$

and,

$$0 = \frac{2M^2}{\alpha_\kappa} n_i(\infty) \left[1 - \sqrt{1 - \frac{2\alpha_\kappa Y_m}{M^2}}\right] +$$
$$+ n_{ph,o} e^{-Y_o} \left[1 - e^{Y_m} - \mathrm{Erf}(-Y_m)^{1/2} + \frac{2}{\sqrt{\pi}} e^{Y_m} \sqrt{-Y_m}\right] -$$
$$- \frac{n_o}{\alpha_\kappa(\kappa - 3/2)} \left[(1 - \alpha_\kappa Y_m)^{3/2-\kappa} - 1\right] +$$
$$+ \frac{4n_o}{3} \sqrt{\frac{\alpha_\kappa}{\pi}} \frac{\Gamma(\kappa)}{\Gamma(\kappa - 1/2)} (1 - \alpha_\kappa Y_m)^{-\kappa} (-Y_m)^{3/2} \; {}_2F_1\left[1, \kappa; \frac{5}{2}; \frac{\alpha_\kappa Y_m}{\alpha_\kappa Y_m - 1}\right]. \quad (3.71)$$

3.2.3 Monotonic Potential Solutions

To investigate monotonic potential solutions, we set $Y_m \equiv 0$, implying that the minimum potential is at $x = \infty$. The third condition is then eliminated as an identity ($0 \equiv 0$), and the remaining two conditions are,

$$\frac{n_o}{2} + \frac{n_{ph,o}}{2} e^{-Y_o} = n_i(\infty), \quad (3.72)$$

and,

$$\frac{n_{ph,o}}{\sqrt{2\pi}} e^{-Y_o} + \frac{n_o}{\sqrt{2\pi}(\kappa - 1)} \frac{\Gamma(\kappa)}{\Gamma(\kappa - 1/2)} \frac{1}{\sqrt{\alpha_\kappa}} - n_i \frac{M}{\sqrt{\alpha_\kappa}} \sqrt{\frac{m_e}{m_i}} = 0. \quad (3.73)$$

The solar wind density, n_o, can be eliminated from the second equation via the first. This yields an exact expression for the normalized surface potential, Y_o, including the dependence on the solar wind electron κ value, of,

$$e^{Y_o} = \frac{n_{ph,o}}{n_{i,\infty}} \left[\frac{1 + \frac{\Gamma(\kappa)}{\sqrt{\alpha_\kappa}(\kappa-1)\Gamma(\kappa-1/2)}}{\frac{2\Gamma(\kappa)}{\sqrt{\alpha_\kappa}(\kappa-1)\Gamma(\kappa-1/2)} - \frac{\sqrt{2\pi}M_\kappa}{\sqrt{\alpha_\kappa}} \sqrt{\frac{m_e}{m_i}}}\right]. \quad (3.74)$$

This solution can be compared with the monotonic solution of the Maxwellian solar wind case [*Nitter et al.*, 1998] by taking the limit as $\kappa \to \infty$, which serves to turn the original κ-function into a Maxwellian. Using the relations,

$$\lim_{\kappa\to\infty} \sqrt{\alpha_\kappa} \;\; \to \;\; \sqrt{\frac{\alpha}{\kappa}}, \quad (3.75)$$
$$\lim_{\kappa\to\infty} \frac{\Gamma(\kappa)}{\Gamma(\kappa - 1/2)} \;\; \to \;\; \sqrt{\kappa}, \quad (3.76)$$
$$\lim_{\kappa\to\infty} M_\kappa \;\; \to \;\; \frac{M}{\sqrt{\kappa}}, \quad (3.77)$$

yields,

$$e^{Y_o} = \frac{n_{ph,o}}{n_{i,\infty}} \left[\frac{1 + 1/\sqrt{\alpha}}{2/\sqrt{\alpha} - M\sqrt{2\pi m_e/(m_i \alpha)}} \right], \tag{3.78}$$

which matches the Maxwellian solution (recognizing that the α defined in this work is $1/\alpha_{Nitter}$) [*Nitter et al.*, 1998].

Figure 3.6 shows the surface potential, V_o, normalized to the Maxwellian surface potential ($\kappa \to \infty$) as a function of κ for typical solar wind conditions ($T_{ph} = 2.2$ eV, $T_{sw} = 10.0$ eV, $u_i = 400$ km s^{-1}). For large κ, the surface potential is seen to approach the Maxwellian solution, as expected. As κ decreases, the higher energy tail of the solar wind electron distribution grows relative to the core population, generating a higher solar wind electron current to the surface. In terms of simple point-wise charging theory [*Manka*, 1973], this increased electron current should drive the surface to a lower potential, as seen in Figure 3.6. Over the full range of κ ($[1.5, \infty]$), the change in surface potential is on the order of 20%.

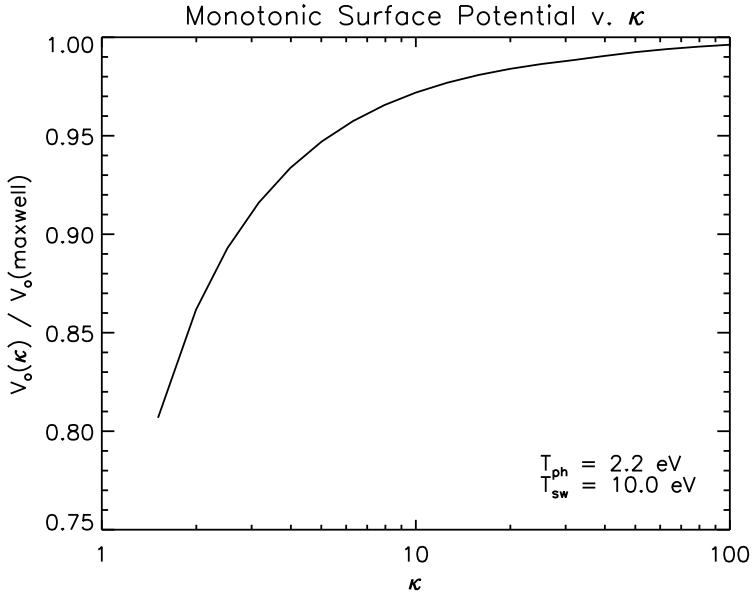

Figure 3.6: The ratio of the κ-dependent surface potential to the Maxwellian surface potential, $V_o(\kappa)/V_o(maxwell)$, as a function of κ. Decreasing the κ value yields a larger high energy tail of incoming solar wind electrons and correspondingly lowers the surface potential.

3.2.4 Non-monotonic Potential Solutions

For the non-monotonic solution, Y_m differs from Y_o, and thus both variables must be found. This is accomplished by deriving two separate equations for $\exp(-Y_o)$ from the second and third boundary conditions and solving these numerically for Y_o and Y_m. We first eliminate the solar wind density at infinity, n_o, via the first condition,

$$\begin{aligned} n_i &= \frac{n_o}{2} + \frac{n_o}{\sqrt{\pi}}\frac{\Gamma(\kappa)}{\Gamma(\kappa-1/2)}\sqrt{-\alpha Y_m}(1-\alpha Y_m)^{-\kappa}\ {}_2F_1\left[\kappa,1;\frac{3}{2};\frac{\alpha_\kappa Y_m}{\alpha_\kappa Y_m - 1}\right] + \\ &\quad + \frac{n_{ph,o}}{2}e^{-Y_o}(1-\mathrm{Erf}\,\sqrt{-Y_m}), \end{aligned} \tag{3.79}$$

which gives,

$$n_o = \frac{1}{G(Y_m)}\left[n_i - \frac{n_{ph,o}}{2}e^{-Y_o}\left(1-\mathrm{Erf}\,\sqrt{-Y_m}\right)\right], \tag{3.80}$$

where we have defined,

$$G(Y_m) \equiv \frac{1}{2} + \frac{1}{\sqrt{\pi}}\frac{\Gamma(\kappa)}{\Gamma(\kappa-1/2)}\sqrt{-\alpha_\kappa Y_m}(1-\alpha_\kappa Y_m)^{-\kappa}\ {}_2F_1\left[\kappa,1;\frac{3}{2};\frac{\alpha_\kappa Y_m}{\alpha_\kappa Y_m - 1}\right]. \tag{3.81}$$

This expression for n_o can be inserted into the second condition, which reads,

$$\frac{n_{ph,o}}{\sqrt{2\pi}}e^{Y_m - Y_o} - \frac{n_o}{\sqrt{2\pi}(\kappa-1)}\frac{\Gamma(\kappa)}{\Gamma(\kappa-1/2)}\frac{1}{\sqrt{\alpha_\kappa}}(1-\alpha_\kappa Y_m)^{-(\kappa-1)} + n_i\frac{M}{\sqrt{\alpha_\kappa}}\sqrt{\frac{m_e}{m_i}} = 0, \tag{3.82}$$

and solved for $\exp(-Y_o)$, which gives,

$$e^{-Y_o} = \frac{n_i}{n_{ph,o}}\left[\frac{-\frac{M}{\sqrt{\alpha_\kappa}}\sqrt{\frac{m_e}{m_i}} + \frac{1}{G(Y_m)}\frac{1}{\sqrt{2\pi}(\kappa-1)}\frac{\Gamma(\kappa)}{\Gamma(\kappa-1/2)}\frac{1}{\sqrt{\alpha_\kappa}}(1-\alpha_\kappa Y_m)^{-(\kappa-1)}}{\frac{1}{\sqrt{2\pi}}e^{Y_m} + \frac{1}{2}(1-\mathrm{Erf}\,\sqrt{Y_m})\frac{1}{G(Y_m)}\frac{1}{\sqrt{2\pi}(\kappa-1)}\frac{\Gamma(\kappa)}{\Gamma(\kappa-1/2)}\frac{1}{\sqrt{\alpha_\kappa}}(1-\alpha_\kappa Y_m)^{-(\kappa-1)}}\right]. \tag{3.83}$$

In order to find the second expression for $\exp(-Y_o)$, the solar wind density is eliminated from the third condition, which reads,

$$\begin{aligned} 0 &= \frac{2M^2}{\alpha_\kappa}n_i(\infty)\left[1-\sqrt{1-\frac{2\alpha_\kappa Y_m}{M^2}}\right] + \\ &\quad + n_{ph,o}e^{-Y_o}\left[1-e^{Y_m}-\mathrm{Erf}(-Y_m)^{1/2}+\frac{2}{\sqrt{\pi}}e^{Y_m}\sqrt{-Y_m}\right] - \\ &\quad - \frac{n_o}{\alpha_\kappa(\kappa-3/2)}\left[(1-\alpha_\kappa Y_m)^{3/2-\kappa}-1\right] + \\ &\quad + \frac{4n_o}{3}\sqrt{\frac{\alpha_\kappa}{\pi}}\frac{\Gamma(\kappa)}{\Gamma(\kappa-1/2)}(1-\alpha_\kappa Y_m)^{-\kappa}(-Y_m)^{3/2}\times \\ &\quad \times\ {}_2F_1\left[1,\kappa;\frac{5}{2};\frac{\alpha_\kappa Y_m}{\alpha_\kappa Y_m - 1}\right]. \end{aligned} \tag{3.84}$$

To ease the derivation, we first define,

$$\begin{aligned} H(Y_m) &= -\frac{1}{\alpha_\kappa(\kappa-3/2)}\left[(1-\alpha_\kappa Y_m)^{3/2-\kappa}-1\right]+ \\ &\quad +\frac{4}{3}\sqrt{\frac{\alpha_\kappa}{\pi}}\frac{\Gamma(\kappa)}{\Gamma(\kappa-1/2)}(1-\alpha_\kappa Y_m)^{-\kappa}(-Y_m)^{3/2}\times \\ &\quad \times {}_2F_1\left[1,\kappa;\frac{5}{2};\frac{\alpha_\kappa Y_m}{\alpha_\kappa Y_m-1}\right]. \end{aligned} \tag{3.85}$$

After substituting for both n_o and $H(Y_m)$, the third condition then reads,

$$\begin{aligned} 0 = &\frac{2M^2}{\alpha_\kappa}n_i(\infty)\left[1-\sqrt{1-\frac{2\alpha_\kappa Y_m}{M^2}}\right]+ \\ &+n_{ph,o}e^{-Y_o}\left[1-e^{Y_m}-\mathrm{Erf}(-Y_m)^{1/2}+\frac{2}{\sqrt{\pi}}e^{Y_m}\sqrt{-Y_m}\right]+ \\ &+\frac{H(Y_m)}{G(Y_m)}\left[n_i-\frac{n_{ph,o}}{2}e^{-Y_o}(1-\mathrm{Erf}\,\sqrt{Y_m})\right]. \end{aligned} \tag{3.86}$$

Finally, the second expression for $\exp(-Y_o)$ is,

$$e^{-Y_o}=\frac{n_i}{n_{ph,o}}\left[\frac{-\frac{H(Y_m)}{G(Y_m)}-\frac{2M^2}{\alpha_\kappa}\left(1-\sqrt{1-\frac{2\alpha_\kappa Y_m}{M^2}}\right)}{1-e^{Y_m}-\mathrm{Erf}\,\sqrt{-Y_m}+\frac{2}{\sqrt{\pi}}e^{Y_m}\sqrt{-Y_m}-\frac{H(Y_m)}{2G(Y_m)}(1-\mathrm{Erf}\,\sqrt{-Y_m})}\right]. \tag{3.87}$$

Using this expression for $\exp(-Y_o)$, combined with the expression from the second condition, and given the parameters, $n_{ph,o}$, n_i, κ, T_{sw}, T_{ph}, and $u_i(\infty)$, the two equations can be numerically solved for Y_o and Y_m. Figure 3.7 shows the surface and minimum potentials, V_o and V_m, respectively, as a function of κ for $T_{ph}=2.2$ eV and $u_i=400$ km s^{-1} for $10<T_{sw}<50$ eV. For small solar wind electron temperatures ($T_{sw}\approx 10$ eV), there is little change in either the surface or minimum potentials as a function of κ, while for larger values of the solar wind temperature ($T_{sw}\approx 50$ eV), the surface and minimum potentials are significantly decreased as $\kappa\rightarrow 1.5$. The potential minimum must decrease as κ decreases in order to reflect a constant amount of solar wind electrons to maintain quasineutrality in the solar wind. Additionally, as $\kappa\rightarrow\infty$, the solutions return to the values predicted by the Maxwellian derivation [*Nitter et al.*, 1998] (compare to Figure 3.2).

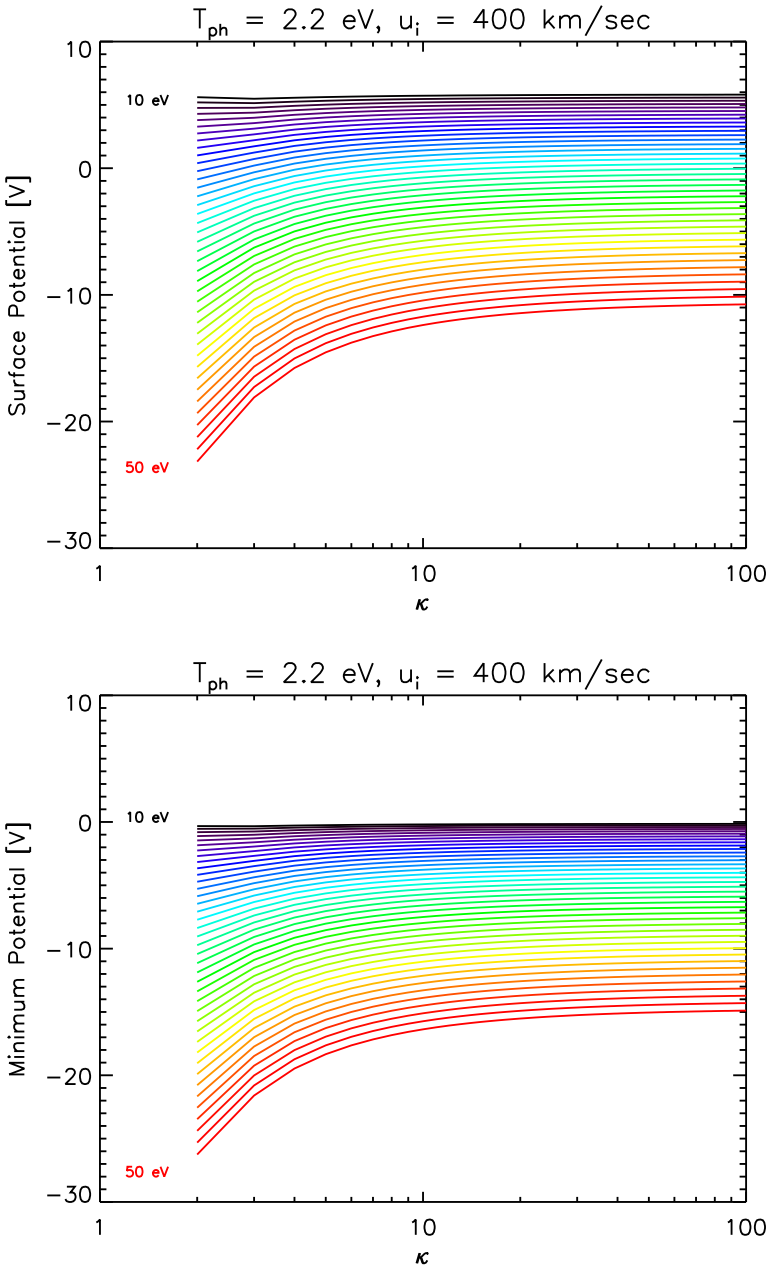

Figure 3.7: The surface and minimum potentials as a function of κ for solar wind temperatures, $10 < T_{sw} < 50$ eV. Black lines represent $T_{sw} = 10$ eV while red lines represent $T_{sw} = 50$ eV.

3.3 Future Theoretical Work

3.3.1 Energy of Sheath Solutions

While the kinetic theory presented above has described several of the main characteristics of photoelectron sheaths immersed in an ambient plasma, questions remain as to the energy state of the sheath. Specifically, in certain areas of parameter space (for example, low photoelectron temperatures and high ambient electron temperatures), both a monotonic and non-monotonic solution are theoretically allowable. Comparisons with results from the PIC code, for example, Figure 3.3, show that while the kinetic theory predicts both types of solutions, the PIC code relaxes exclusively to the non-monotonic case. Previous work has suggested that a preference for the non-monotonic case may be due to the non-monotonic sheath having less electrostatic energy than its monotonic counterpart [*Guernsey and Fu*, 1970; *Fu*, 1971; *Nitter et al.*, 1998]. The electrostatic energy for the monotonic, U_m, and non-monotonic cases, U_{nm}, respectively, are given by,

$$U_m = C\int_0^{Y_o}\sqrt{F(Y)}dY, \tag{3.88}$$

$$U_{nm} = C\int_{Y_m}^{Y_o}\sqrt{F(Y)}dY + C\int_{Y_m}^{0}\sqrt{F(Y)}dY, \tag{3.89}$$

where $F(Y)$ is the right-hand-side of Equation 3.53 transformed into normalized coordinates, $C = \epsilon_o kT_{ph}/2\lambda e$, and λ is the photoelectron Debye length at the surface [*Reitz et al.*, 1993; *Nitter et al.*, 1998]. An analysis of the energies of the κ-distribution sheath solutions (inherently containing the Maxwellian solutions as well) is currently underway and may shed light on the energetic preferability of non-monotonic sheaths over their monotonic counterparts.

3.3.2 Photoelectron Sheaths in the Terrestrial Plasma Sheet

The cases explored analytically in Sections 3.1 and 3.2 have both modeled the solar wind distribution, in which the ions are assumed to be a cold, supersonic beam. Recent *in-situ* measurements, discussed in detail in Chapter 4, have observed non-monotonic potentials while the Moon was immersed in both the terrestrial geomagnetic tail lobes and plasma sheet [*Halekas et al.*, 2008c;

Poppe et al., 2011]. In these cases, the plasma has no bulk flow and the ions are considerably hotter, rendering the supersonic ion assumption invalid. The inclusion of a Maxwellian or κ-distribution ion population would be relatively straightforward as many of the integrals have already been computed for the solar wind electron κ-distribution. The analytical investigation of the photoelectron sheath with the terrestrial plasma sheet as the ambient plasma would provide a method of further confirming and understanding the observations seen above the lunar surface.

Chapter 4

Comparison with In-situ Measurements

4.1 Lunar Prospector

While the previous two chapters have discussed simulations and theoretical efforts to understand the near-surface lunar plasma environment, the ultimate test of these theories must come in the form of experimental measurements. The Lunar Prospector (LP) mission provided the first *in-situ* measurements of various properties of the lunar surface plasma environment, most notably, the surface remanent magnetic field and electrostatic potential. Lunar surface remanent magnetic fields have been known to exist since their measurement in the Apollo era [*Coleman et al.*, 1972; *Anderson et al.*, 1976; *Lin*, 1979; *Fuller and Cisowski*, 1987]; however, a global map was not provided until the Lunar Prospector spacecraft arrived in orbit around the Moon [*Lin et al.*, 1998; *Halekas et al.*, 2001]. The LP Electrostatic Reflectometer (ER) and Magnetometer (MAG) instruments used the magnetic mirroring effect to measure the surface magnetic field and, fortuitously, the surface electrostatic potential as well [*Halekas et al.*, 2005b]. By combining these measurements with data on the ambient plasma conditions (density, temperature, etc.), a near-complete picture of the interaction of the lunar surface with an ambient plasma can be constructed.

Data from the LP spacecraft has told us much of what we know today regarding the lunar plasma environment. By using the electron reflectometry technique, detailed maps of the surface magnetic field strength can be constructed. These surface fields, which have the ability to reflect and deflect incoming solar wind and geomagnetic tail plasmas, range up to hundreds of nT and have been extensively mapped by LP [*Halekas et al.*, 2001, 2010]. The interaction of surface remanent

magnetic fields with the incoming solar wind can create mini-magnetospheres, with complicated dynamics [*Harnett and Winglee*, 2000, 2002, 2003; *Halekas et al.*, 2006a,b, 2008a,b; *Hasimoto et al.*, 2010]. These mini-magnetospheres can cause ions and electrons to be either reflected back into space or deflected laterally, thus altering the near-surface plasma environment. Some areas of strong surface remanent magnetic fields have been associated with lunar swirls, which are areas of anomalous surface albedo [*Hood and Williams*, 1989; *Hood et al.*, 2001; *Kurata et al.*, 2005; *Blewett et al.*, 2007, 2011] and one theory of lunar swirl formation states that differential surface albedo between swirl and non-swirl areas is due to the shielding of solar wind protons from swirl regions.

Surface maps of the electrostatic potential can also be constructed from the LP reflectometry data, shown in Figure 4.1. Above the Moon, incoming electrons are reflected from surface magnetic fields, regardless of energy, if their pitch angle is above a certain cutoff angle, $\alpha_c = \sin^{-1}\sqrt{B_{LP}/B_s}$, where B_{LP} and B_s are the magnetic field strengths at LP's orbit and the surface, respectively. In the presence of an electrostatic potential, electrons are reflected not only magnetically, but also electrostatically, giving rise to energy-dependent reflection. By using the appropriately modified equation for the energy-dependent cutoff angle, $\alpha_c(E) = \sin^{-1}\sqrt{B_{LP}/B_s} \times (1 + e\Phi/E)$, where e is the fundamental charge, Φ is the potential difference between LP and the lunar surface and E is the electron energy, the surface potential can be calculated from the LP reflectometry data [*Feldman et al.*, 1983; *Halekas et al.*, 2002]. Global maps of the surface potential have been constructed and confirm standard understanding of surface charge processes. On the lunar dayside, while in the solar wind, the surface potential typically reaches a value between 10 and 100 V, commensurate with photoemission driving the surface to a positive potential. As the solar zenith angle increases from the sub-solar point, the potential drops towards zero and eventually becomes negative as solar wind electron collection begins to dominate over photoemission. On the lunar nightside, the combination of the lack of photoemission, increased electron temperature and decreased plasma density drives the lunar surface to very large, negative potentials (≈ -300 to -500 V) [*Halekas et al.*, 2005a]. Deviations from this general outline are typically due to changes in the external plasma environment, such as crossings of the terrestrial plasma sheet, during which time the surface

potential in daylight has been observed to reach several hundred volts negative [*Halekas et al.*, 2008c; *Poppe et al.*, 2011], and solar energetic particle events, when measurements of the nightside lunar surface potential have been as low as -4.5 kV [*Halekas et al.*, 2007, 2009b].

In this Chapter, we present a comparison of *in-situ* measurements of the lunar surface potential by the LP ER instrument with the one-dimensional particle-in-cell code. This comparison focuses on a single orbit of LP ER data and successfully shows the measurement of a non-monotonic potential above the lunar surface while the Moon was exposed to the terrestrial plasma sheet. This initial comparison validates both the simulation and theoretical predictions of non-monotonic potentials and provides direction for extensive future work. Section 4.2.1 describes the LP ER measurements and Section 4.2.2 compares these measurements with the results of the PIC simulation. Section 4.2.3 summarizes the results and addresses the extension of these measurements to other bodies in the solar system. Section 4.3 discusses various future data-model comparisons, including surface charging in the solar wind and the role of secondary electrons in producing non-monotonic potentials.

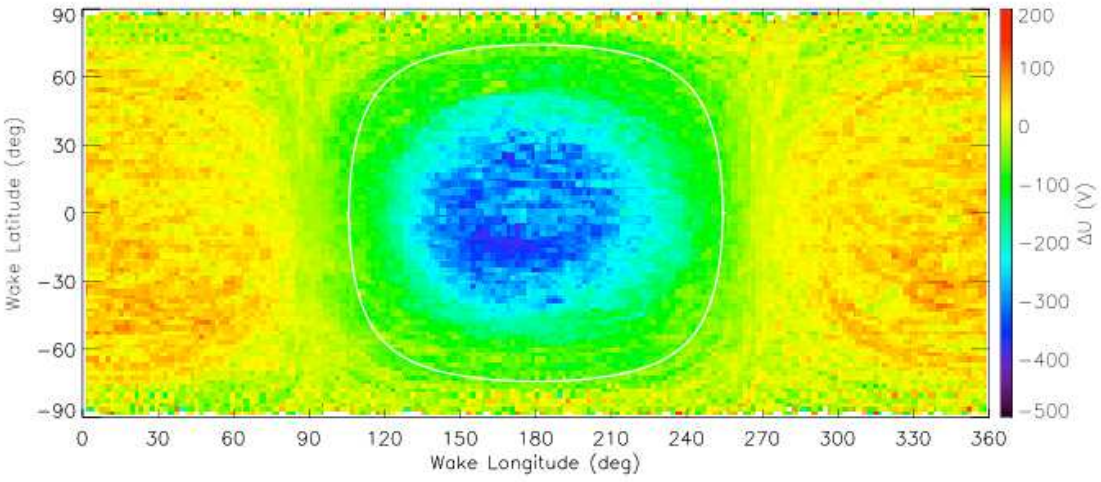

Figure 4.1: The average lunar surface potential as measured by the Lunar Prospector MAG/ER instrument. From *Halekas et al.* [2005a].

4.2 Lunar Surface Charging in Daylight - Plasma Sheet

While magnetic reflection of electrons alone is an energy-independent process, observations of energy-dependent loss cones by the LP ER were interpreted as the result of the combined effects of surface remanent magnetic fields and surface electrostatic potentials [*Halekas et al.*, 2005b, 2007, 2008c]. The majority of the surface potential measurements confirmed previous models of lunar surface charging, yet some measurements presented challenges to these models. Specifically, the LP ER observed large negative potentials (≈ -500 V) above the day-side lunar surface while the Moon was exposed to the terrestrial plasma sheet [*Halekas et al.*, 2008c]. Figure 4.2 shows a time-series during passage through the geomagnetic tail and terrestrial plasma sheet in April 1999, with the panels showing the calculated spacecraft potential, ambient electron density, electron temperature, electron current to the lunar surface, inferred lunar surface potential and sunlight/shadow flag. The terrestrial plasma sheet crossing occurs around 20:00, denoted by the significant increase in electron temperature ($T_{ps} > 500$ eV). During this time, lunar surface potentials in excess of -500 V were seen while in sunlight, contradicting the standard point-wise charging calculations (i.e., *Manka* [1973]) and suggesting the presence of non-monotonic potential structures above the lunar surface [*Halekas et al.*, 2008c].

Chapters 2 and 3 and other previous work have addressed the possibility of non-monotonic potentials above airless bodies using both theoretical and simulation methods [*Guernsey and Fu*, 1970; *Fu*, 1971; *Nitter et al.*, 1998; *Poppe and Horányi*, 2010], and found that not only do non-monotonic potential solutions exist, but that they are energetically preferred to the monotonic solution. These potential structures are significant in that they can affect the interpretation of observational results of surface potentials using the electron reflectometry technique. Non-monotonic potentials are likely to be ubiquitous throughout the solar system in various forms, including at Mercury [*Grard*, 1997], asteroids, and various satellites of Mars and the giant planets. These potential structures should be taken into account when modeling or interpreting observations of near-surface plasma environments [*Reasoner and Burke*, 1972a; *Manka*, 1973; *Dubinin et al.*, 1991;

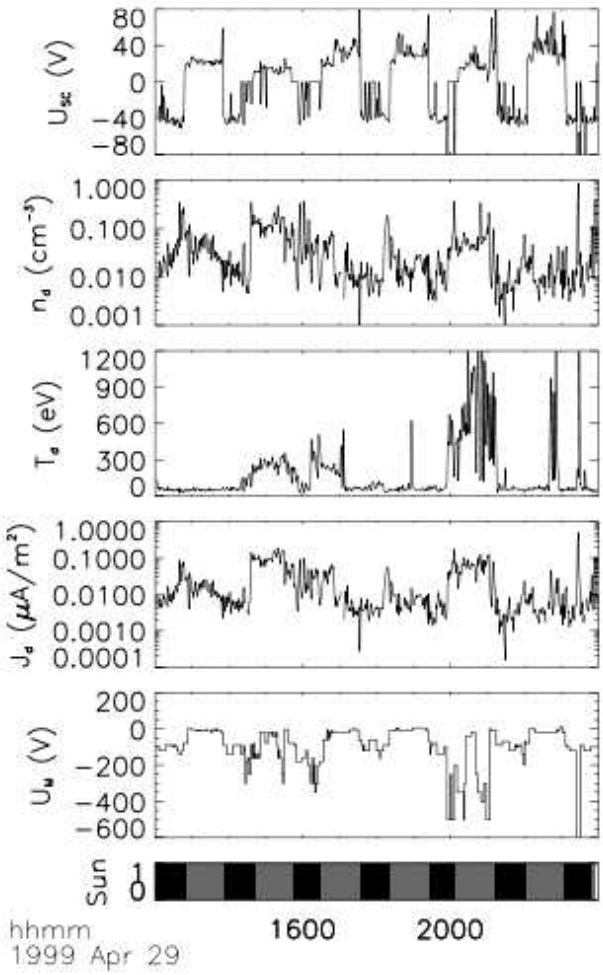

Figure 4.2: Data from Lunar Prospector during a passage through the terrestrial current sheet in April, 1999. The panels show the calculated spacecraft potential, ambient electron density, electron temperature, electron current to the lunar surface, inferred lunar surface potential and sunlight/shadow flag. From *Halekas et al.* [2008c].

Roussos et al., 2010]. Below, we compare a sample LP ER observation of negative potentials above the dayside lunar surface in the terrestrial plasma sheet with a one-dimensional particle-in-cell (PIC) simulation in order to confirm the presence of non-monotonic potentials.

4.2.1 Measurements

4.2.1.1 Data

This study utilizes data from the LP ER instrument to characterize electrons of both magnetospheric and lunar origin. The ER employed a top-hat electrostatic analyzer design to measure the full 3-D electron distribution function. At the time of this study, the energy range of the instrument covered 38 eV to 17 keV. The ER had an intrinsic energy resolution of $\Delta E/E \approx 0.25$, but the onboard processor summed adjacent energy bins, resulting in an effective $\Delta E/E \approx 0.5$. The ER utilized a 360° planar field of view oriented perpendicular to the spin plane to cover all look directions every half-spin (2.5 s), with an angular resolution of 22.5°. Though the ER only had sufficient telemetry to send back full 3-D measurements with an 80 s cadence (corresponding to 120 km separation), the integration lasted only 2.5 s, ensuring an intrinsic spatial resolution for each individual measurement of a few km.

The orbit analyzed in this Section ($\approx$ 90 min in length) came early in the LP extended mission, at $\approx$ 30 km altitude, during a time period when the Moon passed through the center of the terrestrial magnetosphere and encountered the plasma sheet.

4.2.1.2 Analysis

We concentrate on data taken in the terrestrial plasma sheet (characterized by increased electron temperatures and decreased magnetic field strength relative to the lobes), when the spacecraft was in an orbit that covered a wide range of solar zenith angles and the surface magnetic field was relatively small ($<$ 10s of nT). Figure 4.3 shows the magnetic field, the calculated plasma sheet electron temperature, the differential electron energy distribution for five pitch angle bins, the sunlight and magnetic connection flags, and the solar zenith angle of the magnetic footprint. During this time period, we observe an upward-going beam of electrons whenever the spacecraft was on a field line that intersected the Moon, as determined by a straight-line extrapolation of the magnetic field measured at the spacecraft. Previously, such measurements have been used to infer

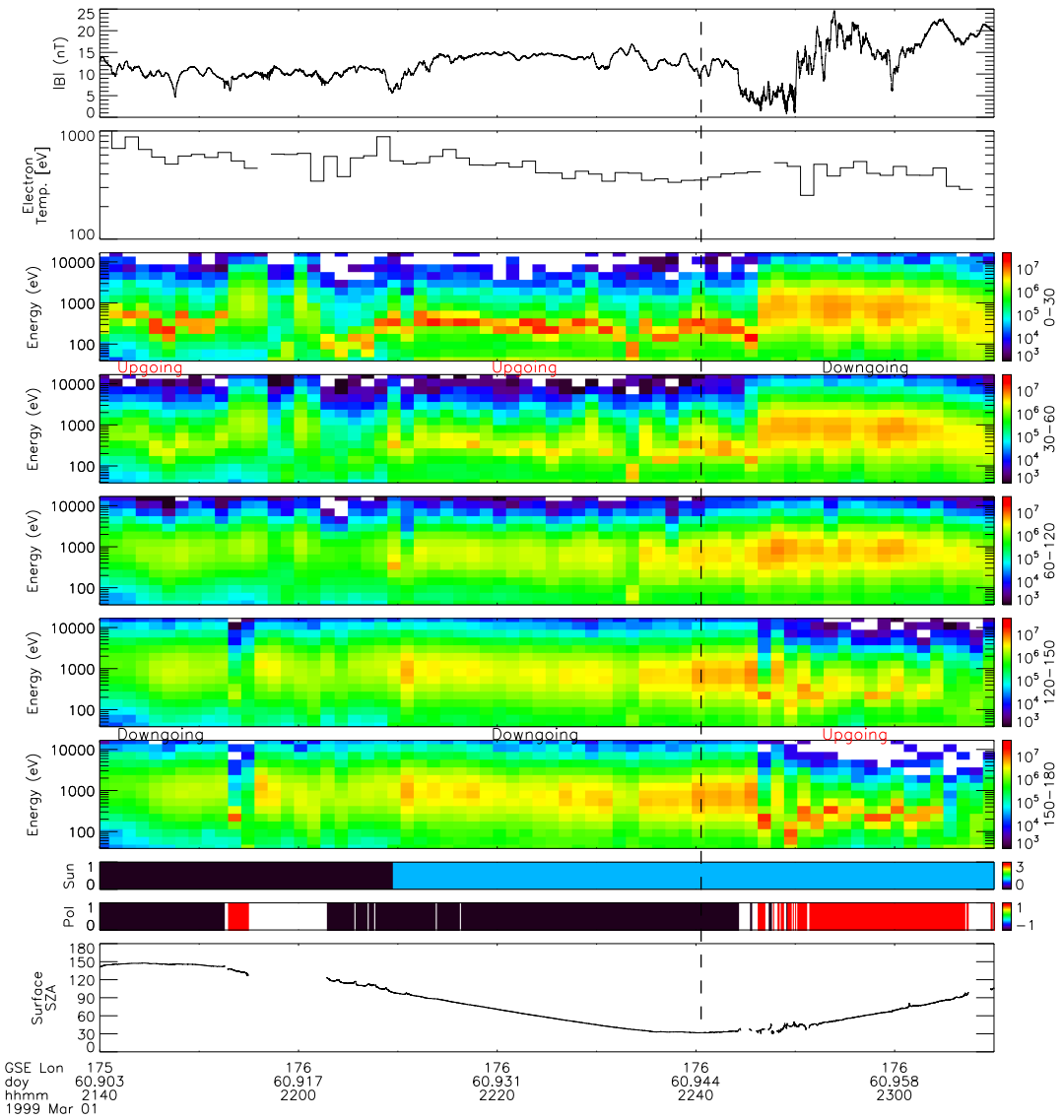

Figure 4.3: Lunar Prospector orbit in the terrestrial magnetotail during a series of plasmasheet passages on March 1, 1999, showing the magnetic field at LP [nT], the plasma sheet electron temperature [eV], electron differential energy flux [eV/(cm^2 sr s eV)] in five different pitch angle channels (0-30°, 30-60°, 60-120°, 120-150°, 150-180°), sun/shadow color bar, 'Sun' (blue = sun, black = shadow), magnetic connection to surface, 'Pol' (assuming no field curvature, red = positive connection, black = negative connection, white = no connection), and solar zenith angle (SZA) of connection to surface. Lunar Prospector observes an upward-going electron beam during this time period whenever magnetically connected to the surface, in both sunlight and shadow.

the presence of a negative surface potential below the spacecraft [*Halekas et al.*, 2005b, 2008c], as expected in shadow or at high solar zenith angle (SZA) in sunlight. However, in this case, we see the upward-going beam of electrons throughout a significant portion of the time period, including times when the magnetic footpoint of the field line passing through the spacecraft reached solar zenith angles of up to $\approx 30^{\circ}$. At these low SZA, the expected photoelectron current from the surface should exceed the magnetospheric electron current by orders of magnitude. This should necessarily force the lunar surface to float to a positive potential, under the assumption that the electrostatic potential varies monotonically above the surface [*Manka*, 1973].

We choose a sample time to investigate in more detail, near the smallest SZA reached on this orbit. We correct the ER data for variations in anode sensitivity, and also apply corrections to the data for the effects of scattered photons and photoelectrons produced on internal surfaces of the instrument by these photons. Due to its large geometric factor, the LP ER was particularly sensitive to these background sources. In order to find the correction, we utilized a spectrum measured at a nearby time (23:09), when the spacecraft was not magnetically connected to the surface. At this time, the measured distribution, other than the photon background, was very well-fit by an isotropic Maxwellian distribution. We therefore subtracted a best-fit Maxwellian to determine the contribution from photon contamination, which should be relatively constant over short time periods. We then subtracted this contamination spectrum from our spectrum of interest to obtain a clean pitch angle-energy spectrum, shown in Figure 4.4. Analysis of the spectrum yielded an electron temperature of $T_{ps} \approx 350$ eV and an electron density of $n_{ps} \approx 10^5$ m^{-3} [*Halekas et al.*, 2009b]. The corrected flux for down-going pitch angles ($90 < \alpha < 180^{\circ}$) now shows a nearly isotropic signal, as expected. The electron beam is clearly seen as an enhancement centered around 300 eV for pitch angles, $\alpha < 45^{\circ}$. While some contamination may remain in the up-going pitch angles at large energies, it remains at a low level compared to the signal of interest. Indeed, none of the corrections described here change the key features of this distribution markedly. At times when the magnetic field aligns with the Earth-Sun line, photon contamination can make a significant difference, especially at small pitch angles; however, at this time the disturbed plasma

sheet magnetic field points sixty degrees away from the Sun, therefore, photon corrections have little impact on field-aligned features.

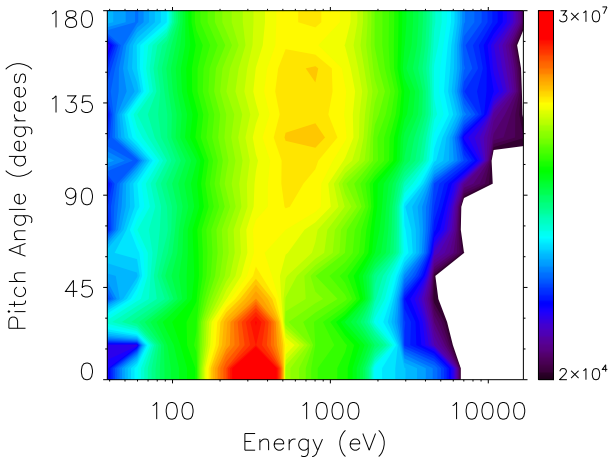

Figure 4.4: Energy pitch angle spectrogram at 22:40:10 on March 1, 1999, shown in units of electron differential energy flux [eV/(cm^2 sr s eV)]. Counts from scattered photons and internally produced photoelectrons have been approximately subtracted, as described in the text. Some residual background counts may remain at energies above 1000 eV in the upward-going pitch angles. The upward-going beam is seen in the loss cone at energies of ∼200-500 eV and pitch angles of 0-45°.

4.2.2 Simulations

We used a one-dimensional, particle-in-cell simulation designed to model the electrostatic plasma environment above the dayside lunar surface while the Moon was in the terrestrial plasma sheet (see Chapter 2 or *Poppe and Horányi* [2010] for an in-depth description of the PIC code). Given the scales required for the simulations (< 10 km), a one-dimensional code is adequate for investigating the LP measurements provided a variable grid is used. We used experimentally measured values for the lunar photoelectron current and energy distribution ($J_{ph} = 4.5 \times 10^{-6}$ A m^{-2}, $T_{ph} = 2.2$ eV [*Feuerbacher et al.*, 1972]) and values representative of the LP ER plasma sheet measurement of Figure 4.3 ($T_{ps} = 100 - 500$ eV, $n_{ps} = 10^5$ m^{-3}). Due to the lack of ion observations, all ion parameters are assumed equal to the electron parameters. Previous work has

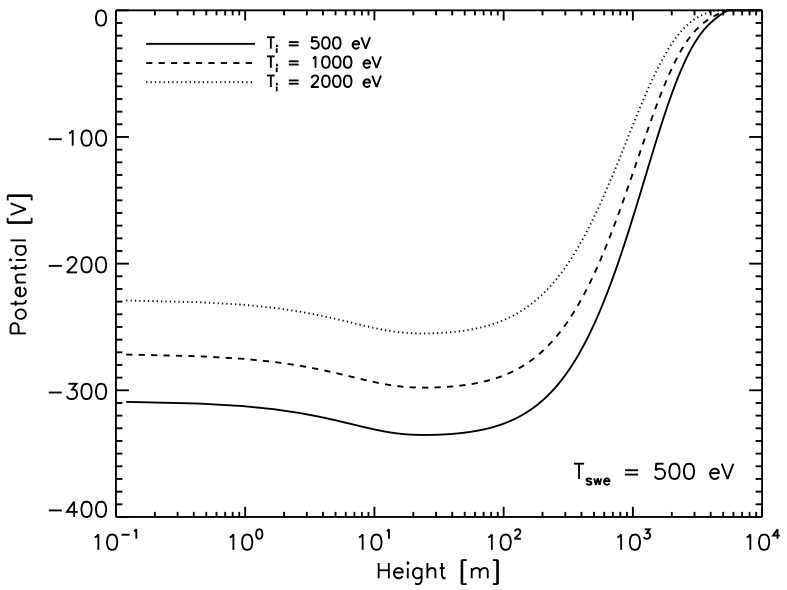

Figure 4.5: The potential as a function of height above the lunar surface for plasma sheet conditions ($T_{ps} = 500$ eV) for varying values of the plasma sheet ion temperature with $m_i/m_e = 100$.

shown that the plasma sheet ion temperature can range up to approximately ten times the electron temperature at lunar distances [*Slavin et al.*, 1985], and preliminary modeling, shown in Figure 4.5 has shown that this may have a small effect on the potential structure. Note that while increasing the ion temperature does change the minimum potentials, the ion mass ratio most likely also plays a role. For the simulations shown, $m_i/m_e = 100$, and increasing this ratio towards the physical value will likely reduce the effect of increasing the solar wind temperature. Future work will investigate the role of the ion temperature, as well as various electron and ion distributions (ie. κ-distributions, see Chapter 3) on the potential structure.

Figure 4.6 shows the potential as a function of height above the lunar surface for various cases of the electron/ion temperature in the plasma sheet, T_{ps}, with the potential normalized to zero at infinity. The potential profiles are consistently non-monotonic, with the region below ≈ 50 m dominated by photoelectrons from the surface and the region above ≈ 50 m dominated by the plasma sheet. Only the most energetic photoelectrons are able to escape out of the near-surface potential well, with most of the photoelectrons trapped near the surface. The photoelectrons that

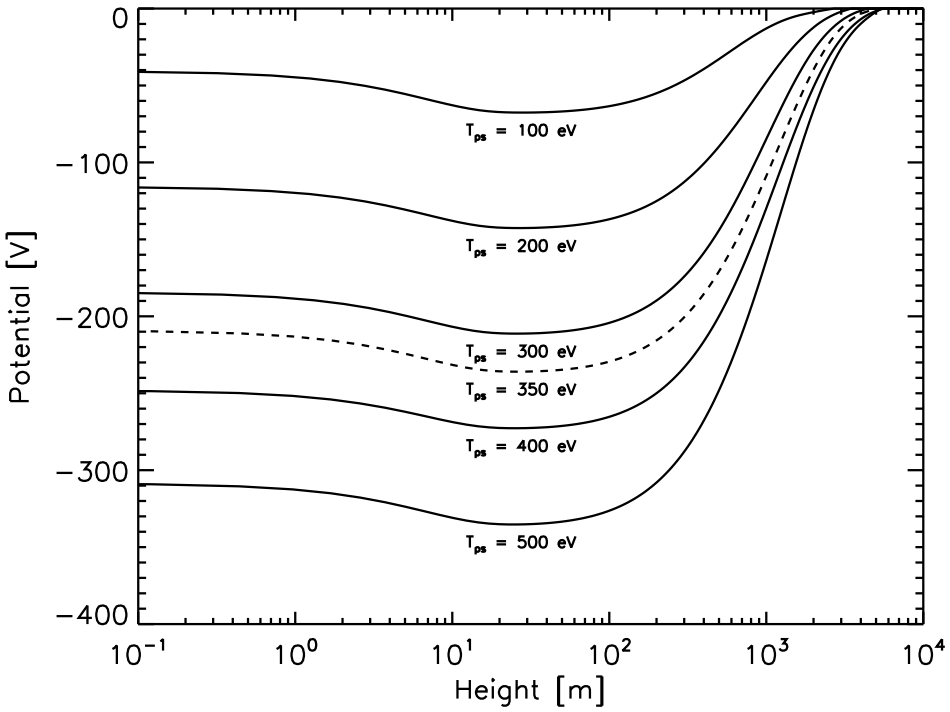

Figure 4.6: The potential as a function of height above the lunar surface from the simulations for five different cases (solid lines) of the plasma sheet electron temperature, T_{ps}. Additionally, the potential for the $T_{ps} = 350$ eV case is also shown (dashed line).

do escape are subsequently accelerated by a potential drop of several hundred volts up to the spacecraft position at an altitude of approximately 30 km. Additionally, the lower-energy bulk of the plasma sheet electrons (ie., $T_{ps} < 220$ eV for the $T_{ps} = 350$ eV case) are reflected by the potential barrier and return to the spacecraft.

In order to provide the best comparison to the 1-d model results, we calculated the reduced distribution function, $f(v_{||})$, from the LP data, and computed the ratio of upward going to downward going phase space density as a function of parallel energy, for the case discussed in Section 4.2.1. To accomplish this, we first re-gridded the measured distribution in terms of parallel and perpendicular velocity, and then calculated, $f(v_{||}) = \int f(v_{||}, v_{\perp}) 2\pi v_{\perp} dv_{\perp}$. In order to reduce the confounding effects of magnetic mirroring, which cannot be captured in a 1-d simulation, we included only data within 0-45° and 130-180° pitch angle in the integral. This selection eliminates

electrons that mirror magnetically before reaching the near-surface sheath region. Though the magnetic mirror force still plays some role in the dynamics of the remaining electrons, the selected population provides the most direct comparison to the simulation.

Figure 4.7 compares the modeled differential energy distributions for both plasma sheet electrons and photoelectrons with the LP ER measurements, all normalized to the downward plasma sheet electron differential energy distribution. Both the model and the LP measurements show a ratio of approximately unity for energies, $E < 150$ eV, and a peak in the upward / downward ratio at energies, $E \approx 220$ eV. The disagreement in the spread of the 220 eV peak is due to the instrinsic LP energy resolution, which acts to smear out the electron flux in energy. As the model shows, the lower energy portion is composed of the reflected plasma sheet electrons, while the peak is composed of escaping photoelectrons accelerated to energies matching the potential barrier above the lunar surface. While the energy resolution of the LP ER smears out the photoelectron peak to some degree, the agreement between the data and the PIC model confirms that the apparent negative surface charging is in fact due to large, non-monotonic potential structures above the lunar surface.

4.2.3 Summary and Discussion

We have presented measurements indicating large negative surface potentials on the dayside lunar surface while in the terrestrial plasma sheet that contradict the standard point-wise charging theory for the lunar surface [*Manka*, 1973]. A one-dimensional PIC simulation of this environment revealed that the LP ER measurements are best explained by the presence of stable, non-monotonic potentials above the lunar surface. Additionally, preliminary work suggests that non-monotonic potentials may also be present while the Moon is in the solar wind [*Halekas et al.*, 2011], and on the lunar nightside. Non-monotonic potentials on the lunar nightside could explain a deficiency in observed lunar secondary electrons, as the potential would serve to trap the secondaries near the surface [*Halekas et al.*, 2009a]. The model also predicts that while electron reflectometry measurements will sense a negative potential, the lunar surface will be charged positively due to

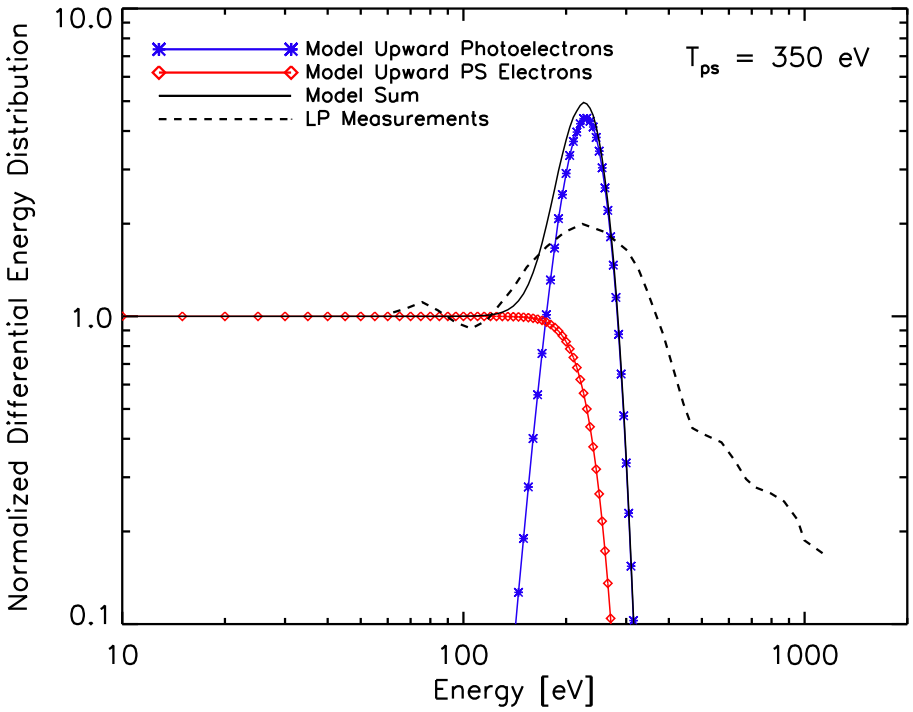

Figure 4.7: The differential energy distribution of escaping photoelectrons (blue curve), reflected (upward-traveling) plasma sheet electrons (red curve), the sum of photoelectrons and reflected plasma sheet electrons (black curve), and LP ER measurements (dashed line), all normalized by the downward-traveling plasma sheet electron differential energy distribution, from the simulation with $T_{ps} = 350$ eV. LP-measured fluxes greater than 500 eV are most likely due to remaining noise contamination.

the change in slope of the potential. By keeping track of particles emitted and absorbed at the left boundary (see *Poppe and Horányi* [2010]), the model indicates that the lunar surface charge density is approximately $+3.9 \times 10^{-11}$ C m^{-2}, regardless of the plasma sheet parameters. The independence of the surface charge density from the external plasma parameters is due to the shielding effect of the non-monotonic potential, and such potentials should be taken into account when estimating surface charge densities.

The measurement of non-monotonic potentials above the Moon suggests that this process may be present at all airless bodies throughout the solar system, including at Mercury [*Grard*, 1997], the Martian moons [*Dubinin et al.*, 1991], and the satellites of the giant planets [*Roussos*

et al., 2010]. Measurements around these bodies should be investigated for any evidence of non-monotonic potentials. Non-monotonic potentials above airless surfaces will also impact the study of electrostatic charging and transport of dust grains and should be taken into account in any models thereof [*Ip*, 1986; *Colwell et al.*, 2005; *Stubbs et al.*, 2006; *Colwell et al.*, 2009; *Poppe and Horányi*, 2010]. Spacecraft may also generate non-monotonic potentials when photoemitting and such an effect should be considered in spacecraft design and data interpretation [*Ergun et al.*, 2010]. Future work will continue to investigate the presence of these non-monotonic potential structures, including any possible dependence on the strength of surface remanent magnetic fields, and the role of instabilities and waves due to the interaction between the upward accelerated beam of photoelectrons and the plasma flow towards the Moon.

4.3 Future Work

4.3.1 Lunar Surface Charging in Daylight - Solar Wind

Similar to when the Moon crosses the terrestrial plasma sheet, the dayside lunar surface is expected to charge positively when in the solar wind. Current balance theory predicts a surface potential of +5-10 V for typical solar wind values ($T_{sw} = 10$ eV, $u_i = 400$ km s^{-1}) [*Manka*, 1973]. However, as discussed in Section 2.3.3 and shown in Figure 2.8(b), non-monotonic potentials are predicted to exist above the lunar surface for solar wind temperatures in the range, $10 < T_{sw} < 100$ eV. The positive identification of non-monotonic potentials in the terrestrial plasma sheet encouraged a search for similar potentials while the Moon was in the solar wind [*Poppe et al.*, 2011; *Halekas et al.*, 2011]. While some limitations of the energy resolution and range of the Electron Reflectometry instrument onboard LP make this a more difficult analysis than for the plasma sheet, there are nonetheless intriguing observations of energy-dependent magnetic reflection above the dayside lunar surface [*Halekas et al.*, 2011]. While this would typically be interpreted as evidence of negative potentials (and most likely negative, non-monotonic potentials) above the lunar surface, the electron distributions measured during these time periods are considerably more complex than

their counterparts in the plasma sheet.

A survey of the LP ER data for energy-dependent magnetic reflection signatures on the day-side lunar surface while in the solar wind yielded three general categories of observations. Some of the observations show an upward-traveling field-aligned photoelectron beam, similar to the plasma sheet case, indicative of non-monotonic potentials above the lunar surface [*Poppe et al.*, 2011]. The second category of observations show a conic distribution in the upward-traveling electrons, where the electron pitch angle distribution peaks at an angle to the magnetic field. This distributions could be the result of a loss-cone instability (first observed near Earth) that excites upper-hybrid waves and heats the electrons in the perpendicular direction, as observed in the terrestrial magnetosphere [*Roth et al.*, 1989]. Finally, the third category of observations include those that show no upward enhancement in flux. Figure 4.8 show the unnormalized (top row) and median-normalized (bottom row) electron $v_{\perp} - v_{||}$ distributions for the three categories of observations ("None", "Conic", "Beam"). While initial work has focused on identifying and categorizing the LP ER observations, future work will investigate these measurements further, including identifying any correlation of the measurements with various parameters, such as solar wind temperature or κ value and the strength of the inferred lunar surface remanent magnetic field strength. The 1-d PIC code can be enhanced to a 1d3v code, which uses one spatial dimension but keeps track of all three velocity dimensions [*Birdsall and Langdon*, 1985]. This code would allow investigation of the proposed loss cone instability that is theorized to produce the conic distributions [*Roth et al.*, 1989].

4.3.2 Lunar Secondary Electron Emission

Secondary electrons are produced when energetic primary electrons strike the lunar surface and stimulate the emission of one or more electrons. The yield of secondaries, δ, is typically characterized by the formula,

$$\delta = 7.4\delta_m(E/E_m)\exp(-2\sqrt{E/E_m}), \tag{4.1}$$

where δ_m is the peak yield and E_m is the energy at which the peak occurs [*Sternglass*, 1954], which varies based on the surface material. Laboratory measurements conducted on lunar dust returned by the Apollo astronauts determined best values of $\delta_m = 1.55$ and $E_m = 400$ eV [*Horányi et al.*, 1998]. Similar to the method by which photoelectrons from the lunar dayside can be measured by LP ER, secondary electrons can be measured above the lunar nightside and by comparing the flux relative to the incoming primary electrons, the parameters δ_m and E_m can be determined [*Halekas et al.*, 2009a]. Shown in Figure 4.9 is a histogram of the ratio, J_{sec}/J_e, as measured by LP ER, where J_{sec} and J_e are the secondary and primary electron currents, respectively. The *in-situ* measurements show that the peak value for the secondary yield is approximately 0.5, roughly three times smaller than that measured in the laboratory [*Horányi et al.*, 1998].

The solution to this discrepancy could be found in considering the effect of non-monotonic potentials in affecting the upcoming secondary electron current. In essence, the secondaries pro-

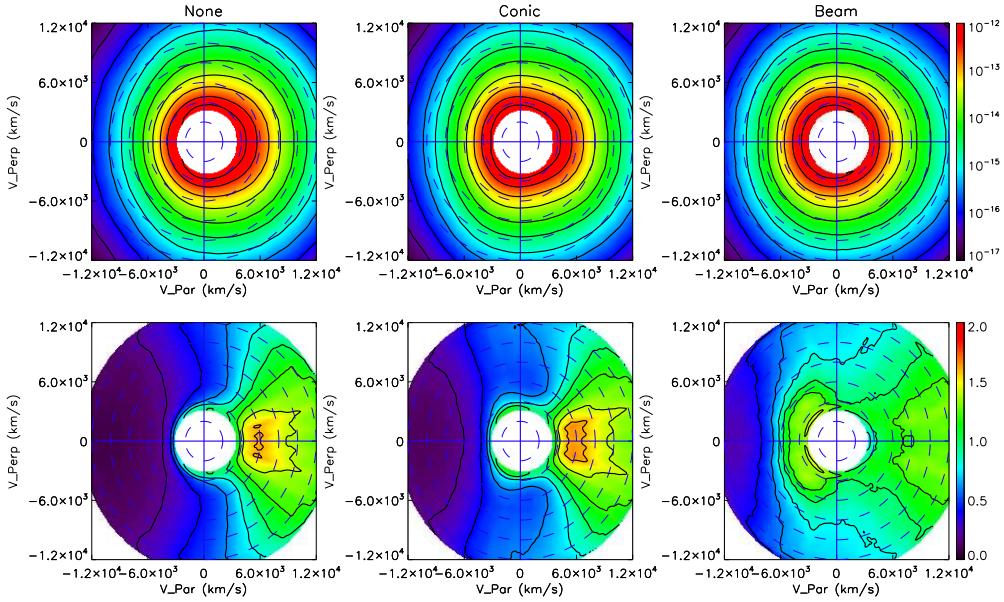

Figure 4.8: The median electron distribution for LP observations above the dayside lunar surface in the solar wind, categorized into: (a) "None", those with no upward going enhancement, (b) "Conic", those with an upward conic pitch angle distribution, and (c) "Beam", those with a upward field-aligned beam distribution. The top panel shows the unnormalized distribution and the bottom panel shows the distribution normalized by the median downward electron distribution for all observations.

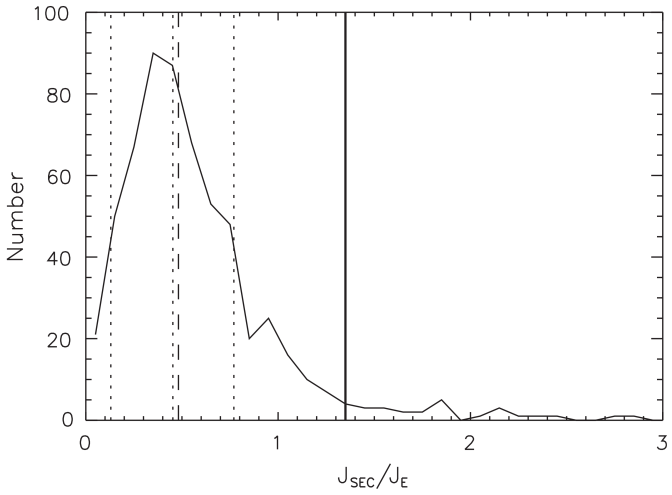

Figure 4.9: The frequency distribution of measurements of the ratio of secondary to primary electron currents above the lunar nightside made by the Lunar Prospector Electron Reflectometer. The dashed line shows the median value while the solid line shows the value approximately consistent with laboratory measurements. From *Halekas et al.* [2009a].

duced at the surface, which have typical temperatures of 2-3 eV [*Whipple*, 1981], would act in a near-identical fashion to photoelectrons. Thus, one might expect the presence of non-monotonic potentials on the lunar nightside due to secondary emission, similar to those found on the dayside due to photoelectrons [*Poppe and Horányi*, 2010; *Poppe et al.*, 2011]. These potentials would then trap secondaries near the surface and reduce the apparent yield of secondaries at the orbit of LP. A relatively straightforward set of PIC simulations can be performed with a secondary emission model to investigate the nightside potential structure and calculate apparent secondary yields at LP in order to reconcile laboratory and *in-situ* measurements.

4.3.3 Upcoming Measurements: ARTEMIS

While comparisons of the PIC simulations and Lunar Prospector measurements of the lunar surface potential have yielded an excellent first comparison, there are numerous questions still open regarding the physics of the solar wind - lunar interaction. In mid-2011, a pair of spacecraft, ARTEMIS P1 and P2, will arrive in lunar orbit, having been retasked from the THEMIS mission, which explored the physics of terrestrial substorms and their role in producing aurorae. The two

ARTEMIS probes will not only bring electron reflectometry and magnetic field measurements to the Moon, similar to Lunar Prospector, but also ion spectrometry. Figure 4.10 shows a schematic of one of the ARTEMIS probes, noting the instruments on-board: Fluxgate Magnetometer (FGM) [Auster *et al.*, 2008], SearchCoil Magnetometer (SCM) [Roux *et al.*, 2008], Electric Field Instrument (EFI) [Bonnell *et al.*, 2008], Electrostatic Analyzer (ESA) [McFadden *et al.*, 2008] and Solid State Telescope (SST) [Angelopoulos *et al.*, 2008; *Angelopoulos*, 2010]. Measurements of the total plasma environment will build upon the LP measurements, allowing a more detailed exploration of the interaction between the lunar photoelectron sheath and ambient plasmas, such as the solar wind or the terrestrial plasma sheet.

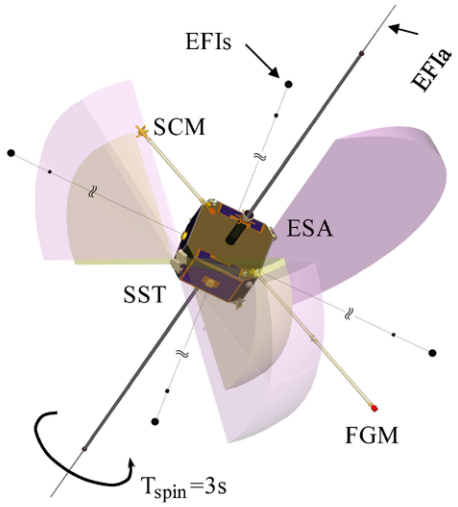

Figure 4.10: A picture of the ARTEMIS spacecraft. From *Angelopoulos* [2010].

Chapter 5

Conclusion

5.1 Summary

This thesis has explored the nature of the lunar photoelectron sheath and the near-surface lunar dusty plasma environment, motivated by a series of puzzling observations of electrostatic dust transport around the Moon. These observations have included measurements by the Lunar Ejecta and Meteorites Experiment of slowly-moving, highly-charged dust grains, images of lunar horizon glow by the Surveyor spacecraft immediately after sunset, and excess brightness in the Apollo coronagraph images [*Criswell*, 1972; *Berg et al.*, 1974; *Rennilson and Criswell*, 1974; *McCoy*, 1976; *Colwell et al.*, 2007; *Glenar et al.*, 2011]. While each of these observations is somewhat circumstantial, the repeated indication of dust dynamics near the lunar surface has motivated a wealth of experimental tests and simulations. In the process of investigating lunar dust dynamics, advances have been made in a wide variety of geophysical fields, including (a) the characterization of dust grain charging processing, such as photoemission, secondary emission and electron/ion collection [*Walch et al.*, 1994, 1995; *Horányi et al.*, 1995, 1998], (b) the role of UV radiation in creating complex plasma environments [*Wang et al.*, 2007b], and (c) the generation of dust ponds such as those found on the asteroid 433 Eros [Veverka *et al.*, 2001; *Robinson et al.*, 2001; *Cheng et al.*, 2002; *Colwell et al.*, 2005; *Hughes et al.*, 2008].

Before the charging, dynamics and possible transport of lunar dust grains can be fully understood, we must have accurate and complete knowledge of the plasma environment in which these grains are immersed. To address this, a one-dimensional particle-in-cell code was developed

following standard procedures [*Birdsall and Langdon*, 1985]. In addition to exploring the geophysically relevant lunar plasma environment, the code was also used to investigate the basic physics of photoelectron sheaths, including their dependence on a variety of parameters (photoelectron temperature, solar wind temperature, solar zenith angle, etc.). The major conclusions of the one-dimensional modeling included that for the sub-solar point, (a) the lunar photoelectron sheath is on the order of 1-10 m in size, (b) has photoelectron densities roughly 10^8 m^{-3} (a factor ten higher than the background solar wind), and (c) utilizing the measured photoelectron emission distribution, has a weaker electric field than would typically be predicted with an equivalent temperature Maxwellian [*Poppe and Horányi*, 2010]. Further variability in the photoelectron sheath parameters comes from external inputs, such as the solar wind temperature and flow speed, the solar zenith angle, and the solar UV radiation intensity. Lunar-based effects on the photoelectron sheath may include modifications to the photoelectron distribution due to the composition of lunar dust grains and complex topography, such as boulders and craters. Three-dimensional PIC simulations have begun to explore the role that topography plays in altering the near surface plasma environment, but significant work remains to be done.

Using the model plasma environments described above, dust dynamics and transport have been studied via a test-particle approach. Similar to previous studies [*Nitter et al.*, 1998; *Colwell et al.*, 2005; *Hughes et al.*, 2008], the charging and trajectories of individual dust grains was followed to study if the photoelectron sheath is capable of levitating dust grains. The test-particle simulations showed that the lunar near-surface electric fields were too weak to permit the levitation of dust grains (even under relatively extreme conditions) much larger than 0.1 μm in radius. Comparison of these limits to grain sizes estimated to comprise the lunar horizon glow observed by the Surveyor spacecraft ($\approx$ 5 μm in radius) [*Criswell*, 1972; *Rennilson and Criswell*, 1974] suggests the possibility that the grains observed by Surveyor were most likely on ballistic trajectories (sometimes described as "hopping"), rather than stable levitation above the lunar surface. Preliminary three-dimensional simulations support this conclusion, as oblique photoillumination conditions have shown regions of strong negative electric fields, which will efficiently attract any positively-charged grains (assuming

the grains are exposed to UV), causing them to rapidly re-impact the lunar surface.

While our knowledge of the near-surface lunar plasma environment has been advanced through the work in this thesis, there remains much yet to be done. Research in two main areas related to PIC and test-particle simulations would help to bring closure and understanding to the issue of lunar dust dynamics:

- The role of three-dimensional topography in altering the lunar near-surface plasma environment: As discussed above, surface topography can have a significant effect on the charging and potential properties of the lunar surface. Obstacles to the solar wind flow, such as boulders or crater rims, may lead to the generation of mini-wakes, which in turn may impact the efficiency of dust grain transport [*Farrell et al.*, 2010]. The VORPAL© PIC simulation software is an excellent tool for robustly modeling the lunar near-surface plasma environment and should be vigorously pursued in the future.

- The "microphysics" of lunar dust grain charging and electrostatic ejection from the surface. While the test-particle simulations of lunar dust grain dynamics have explored the ability of the photoelectron sheath to levitate and transport grains, there is significant uncertainty regarding the method of grain ejection off of the surface. Investigation, both theoretical and experimental, regarding the combined role of adhesive, cohesive and electrostatic forces on micron-sized dust grains in a plasma environment are required to understand the method(s) by which dust grains can be ejected off the lunar surface.

This research has application not only to lunar dust dynamics from a scientific perspective, but would also be applicable to the engineering design of any future exploration habitats and/or equipment on the lunar surface.

In an effort to complement our understanding of the lunar plasma environment via the PIC code, a theoretical description of a photoemitting surface immersed in an ambient plasma was developed with the use of kinetic theory. Distribution functions for the photoelectrons and solar wind electrons, combined with the continuity equation for solar wind ions, are used with several

boundary conditions to find the values for the surface and minimum potential for the static case. Previous work, using either a Fermi and Maxwellian distribution for the solar wind electrons and a Maxwellian for the photoelectrons [*Guernsey and Fu*, 1970; *Fu*, 1971; *Nitter et al.*, 1998], has been compared to the PIC simulations in order to validate the code. In order to increase the geophysical applicability of the previous theories, we have presented a derivation of the photoelectron sheath potentials for a solar wind electron κ-distribution, which is prevalent in a wide variety of space plasmas. Notably, for both the previous Maxwellian distributions and the κ-distributions used in this thesis, there exist regions in parameter space where both monotonic and non-monotonic potentials are solutions. Additionally, the derivations have shown that for $\kappa \rightarrow 1.5$, which causes the hot tail of the electron distribution to increase relative to the core population, that the surface and minimum potentials (for both the monotonic and non-monotonic cases) decrease accordingly. Further work with the theoretical analysis should include a comparison of the electrostatic energy of monotonic and non-monotonic potentials for the same parameters in order to determine which solution may be energetically preferable. Additionally, the theory should be extended to the case where the ions are not supersonic (and thus, require a distribution function to describe), such as the terrestrial current sheet.

The final project presented in this thesis was a comparison of *in-situ* measurements by the Lunar Prospector Electron Reflectometer with PIC simulation results of the lunar photoelectron sheath in the terrestrial plasma sheet. LP ER measurements of the electron energy-pitch angle distribution above the lunar surface can be used to extrapolate the value of both the lunar surface remanent magnetic field strength and electrostatic potential. Occasionally, while the lunar surface was exposed to the terrestrial current sheet, the LP ER measurements indicated that the lunar surface potential was hundreds of volts negative, in contradiction with previous point-wise theories of surface charging, which would predict a positive potential around 10 V [*Manka*, 1973; *Halekas et al.*, 2008c]. PIC simulations of the lunar photoelectron sheet using the ambient plasma parameters measured by LP showed that the large, negative surface potentials measured by LP were due to stable non-monotonic potentials above the lunar surface. The agreement was shown

not only through the value of the simulated potential minimum (which is the potential that LP ER would sense as the "surface potential"), but also through the presence of a cold, high-energy beam of photoelectrons that escaped the near-surface potential barrier and was subsequently accelerated through several hundred volts up to the spacecraft. The LP measurement used in this comparison consisted of a single 2.5 sec observation out of approximately six months of terrestrial plasma sheet data. The wealth of LP ER data, in addition to new data soon to arrive from the dual-probe ARTEMIS mission, will allow the investigation of non-monotonic potentials from a statistical point-of-view, which may lead to further discoveries and understanding of the interaction of ambient plasma with the lunar surface.

In summary, our understanding of the near-surface lunar plasma environment and its role in influencing micron-sized dust dynamics has been extended through a robust combination of modeling, theoretical and observational studies. The work put forth in this thesis has laid the foundation for studies of several related phenomena, including the generation of spatially complex photoelectron sheaths due to surface topography, the role that this topography plays in generating the observed lunar dusty phenomena, such as horizon glow and horizontally transported dust grains, and finally, the basic physics of the interaction between an airless body in the solar system and an ambient plasma.

Bibliography

Abbas, M. M., Tankosic, D., Craven, P. D., Spann, J. F., LeClair, A. and West, E. A., Lunar dust charging by photoelectric emissions, *Planet. Space Sci.*, **55**, pp. 953–965 (2007).

Abbas, M. M., Tankosic, D., Craven, P. D., Spann, J. F., LeClair, A., West, E. A., Weingartner, J. C., Tielens, A. G. G. M., Nuth, J. A., Camata, R. P. and Gerakines, P. A., Photoelectric emission measurements on the analogs of individual cosmic dust grains, *Astrophys. J.*, **645**, pp. 324–336 (2006).

Abramowitz, M. and Stegun, I. A., eds., *Handbook of Mathematical Functions with Formulas, Graphs and Mathematical Tables*, General Publishing Company, Ltd., 30 Lesmill Road, Don Mills, Toronto, Ontario, Canada, 9th edition (1970).

Anderson, K. A., Lin, R. P., McCoy, J. E. and McGuire, R. E., Measurements of lunar and planetary magnetic fields by reflection of low energy electrons, *Space Sci. Instrum.*, **1**, pp. 439–470 (1976).

Angelopoulos, V., The ARTEMIS mission, *Space Sci. Rev.* (2010).

Angelopoulos, V. *et al.*, The THEMIS mission, *Space Sci. Rev.* (2008).

Auster, H. U. *et al.*, The THEMIS fluxgate magnetometer, *Space Sci. Rev.* (2008).

Berg, O. E., Richardson, F. F. and Burton, H., Apollo 17 preliminary science report, Technical Report NASA SP-330, National Aeronautics and Space Administration (1973).

Berg, O. E., Richardson, F. F., Rhee, J. W. and Auer, S., Preliminary Results of a Cosmic Dust Experiment on the Moon, *Geophys. Res. Lett.*, **1**(7), pp. 289–290 (1974).

Birdsall, C. K. and Bridges, W. B., Space-Charge Instabilities in Electron Diodes and Plasma Converters, *J. Appl. Phys.*, **32**(12), pp. 2611–2618 (1961).

Birdsall, C. K. and Langdon, A. B., *Plasma physics via computer simulation*, McGraw-Hill, New York (1985).

Blewett, D. T., Coman, E. I., Hawke, B. R., Gillis-Davis, J. J., Purucker, M. E. and Hughes, C. G., Lunar swirls: Examining crustal magnetic anomalies and space weathering trends, *J. Geophys. Res.*, **116**(E02002) (2011).

Blewett, D. T., Hawke, B. R., Richmond, N. C. and Hughes, C. G., A magnetic anomaly associated with an albedo feature near Airy crater in the lunar nearside highlands, *Geophys. Res. Lett.*, **34**(L24206) (2007).

Bonnell, J. W. *et al.*, The Electric Field Instrument (EFI) for THEMIS, *Space Sci. Rev.* (2008).

Borisov, N. and Mall, U., Charging and motion of dust grains near the terminator of the moon, *Planet. Space Sci.*, **54**, pp. 572–580 (2006).

Bridges, W. B. and Birdsall, C. K., Space-Charge Instabilities in Electron Diodes. II, *J. Appl. Phys.*, **34**(10), pp. 2946–2955 (1963).

Chamberlin, P. C., Woods, T. N. and Eparvier, F. G., New flare model using recent measurements of the solar ultraviolet irradiance, *Adv. Space Res.*, **42**, pp. 912–916 (2008).

Cheng, A. F., Izenberg, N., Chapman, C. R. and Zuber, M. T., Ponded deposits on asteroid 433 Eros, *Meteorit. Planet. Sci.*, **37**, pp. 1095–1105 (2002).

Christon, S. P., Mitchell, D. G. and Williams, D. J., Energy Spectra of Plasma Sheet Ions and Electrons from 50 eV/e to 1 MeV During Plasma Temperature Transitions, *J. Geophys. Res.*, **93**(A4), pp. 2562–2572 (1988).

Christon, S. P., Williams, D. J. and Mitchell, D. G., Spectral Characteristics of Plasma Sheet Ion and Electron Populations During Undisturbed Geomagnetic Conditions, *J. Geophys. Res.*, **94**(A10), pp. 13,409–13,424 (1989).

Coleman, P. J., Lichtenstein, B., Russell, C., Sharp, L. and Schubert, G., Magnetic fields near the Moon, *Proc. 3rd Lunar Sci. Conf.*, **3**(2271-2286) (1972).

Colwell, J. E., Batiste, S., Horányi, M., Robertson, S. and Sture, S., Lunar surface: Dust dynamics and regolith mechanics, *Rev. Geophys.*, **45** (2007).

Colwell, J. E., Gulbis, A. A. S., Horányi, M. and Robertson, S., Dust transport in photoelectron layers and the formation of dust ponds on Eros, *Icarus*, **175**, pp. 159–169 (2005).

Colwell, J. E., Robertson, S., Horányi, M., Wang, X., Poppe, A. and Wheeler, P., Lunar dust levitation, *J. Aero. Eng.*, **1**, pp. 2–9 (2009).

Courant, R., Friedrichs, K. and Lewy, H., On the Partial Difference Equations of Mathematical Physics, *Mathematische Annalen*, **100**, pp. 32–74 (1928).

Criswell, D. R., Lunar dust motion, *Proc. 3rd Lunar Sci. Conf.*, **3**, pp. 2671–2680 (1972).

Criswell, D. R. and De, B. R., Intense Localized Photoelectric Charging in the Lunar Sunset Terminator Region: 2. Supercharging at the Progression of Sunset, *J. Geophys. Res.*, **82**(7) (1977).

De, B. R. and Criswell, D. R., Intense Localized Photoelectric Charging in the Lunar Sunset Terminator Region: 1. Development of Potentials and Fields, *J. Geophys. Res.*, **82**(7) (1977).

Dubinin, E. M., Pissarenko, N. F., Barabash, S. V., Zakharov, A. V., Lundin, R., Pellinen, R. and Schwingenschuh, K., Plasma and magnetic field effects associated with Phobos and Deimos tori, *Planet. Space Sci.*, **39**(1/2), pp. 113–121 (1991).

Ergun, R. E., Malaspina, D. M., Bale, S. D., McFadden, J. P., Larson, D. E., Mozer, F. S., Meyer-Vernet, N., Maksimovic, M., Kellogg, P. J. and Wygant, J. R., Spacecraft charging and ion wake formation in the near-Sun environment, *Phys. Plasma*, **17** (2010).

Farrell, W. M., Stubbs, T. J., Halekas, J. S., Killen, R. M., Delory, G. T., Collier, M. R. and Vondrak, R. R., Anticipated electrical environment within permanently shadowed lunar craters, *J. Geophys. Res.*, **115**(E03004) (2010).

Farrell, W. M., Stubbs, T. J., Vondrak, R. R., Delory, G. T. and Halekas, J. S., Complex electric fields near the lunar terminator: The near-surface wake and accelerated dust, *Geophys. Res. Lett.*, **34** (2007).

Feldman, W. C., Anderson, R. C., Bame, S. J., Gary, S. P., Gosling, J. T., McComas, D. J., Thosen, M. F., Paschmann, G. and Hoppe, M. M., Electron Velocity Distributions Near the Earth's Bow Shock, *J. Geophys. Res.*, **88**(A1), pp. 96–110 (1983).

Feuerbacher, B., Anderegg, M., Fitton, B., Laude, L. D., Willis, R. F. and Grard, R. J. L., Photoemission from lunar surface fines and the lunar photoelectron sheath, *Proc. 3rd Lunar Sci. Conf.*, **3**, pp. 2655–2663 (1972).

Flanagan, T. M. and Goree, J., Dust release from surfaces exposed to plasma, *Phys. Pl.*, **13** (2006).

Freeman, J. W., Balsiger, H. and Hills, H. K., Suprathermal Ion Detector Experiment - Apollo 12 Preliminary Science Report, Technical Report SP 235, Section 6, NASA (1970).

Freeman, J. W., Fenner, M. A., Hills, H. K., Lindeman, R. A., Medrano, R. and Meister, J., Suprathermal Ions Near the Moon, *Icarus*, **16**, pp. 328–338 (1972).

Freeman, J. W. and Ibrahim, M., Lunar electric fields, surface potential and associated plasma sheaths, *The Moon*, **14**, pp. 103–114 (1975).

Fu, J. H. M., Surface Potential of a Photoemitting Plate, *J. Geophys. Res.*, **76**(10), pp. 2506–2509 (1971).

Fuller, M. and Cisowski, S., Lunar paleomagnetism, in J. Jacobs, ed., *Geomagnetism*, volume 2, pp. 307–456, Academic, San Diego, Calif. (1987).

Glenar, D. A., Stubbs, T. J., McCoy, J. E. and Vondrak, R. R., A Reanalysis of the Apollo Light Scattering Observations, and Implications for Lunar Exospheric Dust, *Planet. Space Sci.* (2011).

Goertz, C. K., Dusty Plasmas in the Solar System, *Rev. Geophys.*, **27**(2), pp. 271–292 (1989).

Grard, R., Photoemission on the surface of Mercury and related electrical phenomena, *Planet. Space Sci.*, **45**(1), pp. 67–72 (1997).

Grard, R., Laakso, H. and Pulkkinen, T. I., The role of photoemission in the coupling of the Mercury surface and magnetosphere, *Planet. Space Sci.*, **47**, pp. 1459–1463 (1999).

Grard, R. J. L. and Tunaley, J. K. E., Photoelectron sheath near a planar probe in interplanetary space, *J. Geophys. Res.*, **76**(10), pp. 2498–2505 (1971).

Guernsey, R. L. and Fu, J. H. M., Potential distribution surrounding a photo-emitting plate in a dilute plasma, *J. Geophys. Res.*, **75**(16), pp. 3193–3199 (1970).

Halekas, J. S., Bale, S. D., Mitchell, D. L. and Lin, R. P., Electrons and magnetic fields in the lunar plasma wake, *J. Geophys. Res.*, **110** (2005a).

Halekas, J. S., Brain, D. A., Lin, R. P. and Mitchell, D. L., Solar wind interaction with lunar crustal magnetic anomalies, *Adv. Space Res.*, **41**, pp. 1319–1324 (2008a).

Halekas, J. S., Brain, D. A., Mitchell, D. L. and Lin, R. P., Whistler waves observed near lunar crustal magnetic sources, *Geophys. Res. Lett.*, **33**(L22104) (2006a).

Halekas, J. S., Brain, D. A., Mitchell, D. L., Lin, R. P. and Harrison, L., On the occurrence of magnetic enhancements caused by solar wind interaction with lunar crustal fields, *Geophys. Res. Lett.*, **33**(L08106) (2006b).

Halekas, J. S., Delory, G. T., Brain, D. A., Lin, R. P., Fillingim, M. O., Lee, C. O., Mewaldt, R. A., Stubbs, T. J., Farrell, W. M. and Hudson, M. K., Extreme lunar surface charging during solar energetic particle events, *Geophys. Res. Lett.*, **34** (2007).

Halekas, J. S., Delory, G. T., Brain, D. A., Lin, R. P. and Mitchell, D. L., Density cavity observed over a strong lunar crustal magnetic anomaly in the solar wind: A mini-magnetosphere?, *Adv. Space Res.*, **56**, pp. 941–946 (2008b).

Halekas, J. S., Delory, G. T., Lin, R. P., Stubbs, T. J. and Farrell, W. M., Lunar prospector observations of the electrostatic potential of the lunar surface and its response to incident currents, *J. Geophys. Res.*, **113** (2008c).

Halekas, J. S., Delory, G. T., Lin, R. P., Stubbs, T. J. and Farrell, W. M., Lunar Prospector measurements of secondary electron emission from lunar regolith, *Planet. Space Sci.*, **57**(78-82) (2009a).

Halekas, J. S., Delory, G. T., Lin, R. P., Stubbs, T. J. and Farrell, W. M., Lunar surface charging during solar energetic particle events: Measurement and prediction, *J. Geophys. Res.*, **114**(A05110) (2009b).

Halekas, J. S., Lillis, R. J., Lin, R. P., Manga, M., Purucker, M. E. and Carley, R. A., How strong are lunar crustal magnetic fields at the surface?: Considerations from a reexamination of the electron reflectometry technique, *J. Geophys. Res.*, **115**(E03006) (2010).

Halekas, J. S., Lin, R. P. and Mitchell, D. L., Large negative lunar surface potentials in sunlight and shadow, *Geophys. Res. Lett.*, **32** (2005b).

Halekas, J. S., Mitchell, D. L., Lin, R. P., Frey, S., Hood, L. L., Acuña, M. H. and Binder, A. B., Mapping of crustal magnetic anomalies on the lunar near side by the Lunar Prospector electron reflectometer, *J. Geophys. Res.*, **106**(E11), pp. 27,841–27,852 (2001).

Halekas, J. S., Mitchell, D. L., Lin, R. P., Hood, L. L., Acuña, M. H. and Binder, A. B., Evidence for negative charging of the lunar surface in shadow, *Geophys. Res. Lett.*, **29**(10), p. 1435 (2002).

Halekas, J. S., Poppe, A., Delory, G. T., Farrell, W. M. and Horányi, M., Solar Wind Electron Interaction with the Dayside Lunar Surface and Crustal Magnetic Fields: Evidence for Precursor Effects, *Earth Planets Space* (2011).

Harnett, E. M. and Winglee, R., Two-dimensional MHD simulation of the solar wind interaction with magnetic field anomalies on the surface of the Moon, *J. Geophys. Res.*, **105**(A11), pp. 24,997–25,007 (2000).

Harnett, E. M. and Winglee, R. M., 2.5D Particle and MHD simulations of mini-magnetospheres at the Moon, *J. Geophys. Res.*, **107**(A12) (2002).

Harnett, E. M. and Winglee, R. M., 2.5-D simulations of the solar wind interacting with multiple dipoles on the surface of the Moon, *J. Geophys. Res.*, **108**(A2) (2003).

Hasimoto, K., Hashitani, M., Kasahara, Y., Omura, Y., Nishino, M. N., Saito, Y., Yokota, S., Ono, T., Tsunakawa, H., Shibuya, H., Matsushima, M., Shimizu, H. and Takahashi, F., Electrostatic solitary waves associated with magnetic anomalies and wake boundary of the Moon observed by KAGUYA, *Geophys. Res. Lett.*, **37**(L19204) (2010).

Hill, J. R. and Mendis, D. A., On the braids and spokes in Saturn's ring system, *The Moon and the Planets*, **24**, pp. 431–436 (1981).

Hood, L. L. and Williams, C. R., The Lunar Swirls: Distribution and Possible Origins, *Proc. 19th Lunar Sci. Conf.*, **19**, pp. 99–113 (1989).

Hood, L. L., Zakharian, A., Halekas, J., Mitchell, D. L., Lin, R. P., Acuña, M. H. and Binder, A. B., Initial mapping and interpretation of lunar crustal magnetic anomalies using Lunar Prospector magnetometer data, *J. Geophys. Res.*, **106**(E11), pp. 27,825–27,839 (2001).

Horányi, M., Charged dust dynamics in the solar system, *Annu. Rev. Astron. Astrophys.*, **34**, pp. 383–418 (1996).

Horányi, M., Robertson, S. and Walch, B., Electrostatic charging properties of simulated lunar dust, *Geophys. Res. Lett.*, **22**(16), pp. 2,079–2,082 (1995).

Horányi, M., Walch, B., Robertson, S. and Alexander, D., Electrostatic charging properties of apollo 17 lunar dust, *J. Geophys. Res.*, **103**(E4), pp. 8575–8580 (1998).

Hughes, A. L. H., Colwell, J. E. and DeWolfe, A. W., Electrostatic dust transport on Eros: 3-D simulations of pond formation, *Icarus*, **195**, pp. 630–648 (2008).

Intrator, T., Cho, M. H., Wang, E. Y., Hershkowitz, N., Diebold, D. and DeKock, J., The virtual cathode as a transient double sheath, *J. Appl. Phys.*, **64**(6), pp. 2927–2933 (1988).

Ip, W.-H., Electrostatic charging and dust transport at Mercury's surface, *Geophys. Res. Lett.*, **13**(11), pp. 1133–1136 (1986).

Kadish, A., Faehl, R. J. and Snell, C. M., Analysis and simulation of virtual cathode oscillations, *Phys. Fluids*, **29**(12), pp. 4192–4203 (1986).

Kurata, M., Tsunakawa, H., Saito, Y., Shibuya, H., Matsushima, M. and Shimizu, H., Mini-magnetosphere over the Reiner Gamma magnetic anomaly region on the Moon, *Geophys. Res. Lett.*, **32**(L24205) (2005).

Lin, R. P., Constraints on the origins of lunar magnetism from electron reflection measurements of surface magnetic fields, *Phys. Earth Planet. Int.*, **20**, pp. 271–280 (1979).

Lin, R. P., Mitchell, D. L., Curtis, D. W., Anderson, K. A., Carlson, C. W., McFadden, J., Acuña, M. H., Hood, L. L. and Binder, A. B., Lunar Surface Magnetic Fields and Their Interaction with the Solar Wind: Results from Lunar Prospector, *Science*, **281**, pp. 1480–1484 (1998).

Manka, R. H., Plasma and potential at the lunar surface, in R. J. L. Grard, ed., *Photon and particle interactions with surfaces in space*, *Astrophysics and Space Science Library*, volume 37, pp. 347–361 (1973).

McCoy, J. E., Photometric studies of light scattering above the lunar terminator from Apollo solar corona photography, *Proc. 7th Lunar Sci. Conf.*, pp. 1087–1112 (1976).

McFadden, J. P. *et al.*, The THEMIS ESA plasma instrument and in-flight calibration, *Space Sci. Rev.* (2008).

Neugebauer, M., Snyder, C. W., Clay, D. R. and Goldstein, B. E., Solar wind observations on the lunar surface with the Apollo-12 ALSEP, *Planet. Space Sci.*, **20**, pp. 1577–1591 (1972).

Nieter, C. and Cary, J. R., VORPAL: a versatile plasma simulation code, *J. Comp. Phys.*, **196**, pp. 448–473 (2004).

Nitter, T., Aslaksen, T. K., Melandsø, F. and Havnes, O., Levitation and dynamics of a collection of dust particles in a fully ionized plasma sheath, *IEEE Trans. Plasma Sci.*, **22**(2), pp. 159–172 (1994).

Nitter, T. and Havnes, O., Dynamics of dust in a plasma sheath and injection of dust into the plasma sheath above moon and asteroidal surfaces, *Earth, Moon and Planets*, **56**, pp. 7–34 (1992).

Nitter, T., Havnes, O. and Melandsø, F., Levitation and dynamics of charged dust in the photoelectron sheath above surfaces in space, *J. Geophys. Res.*, **103**(A4), pp. 6605–6620 (1998).

Northrop, T. G. and Birmingham, T. J., Equilibrium electric potential of spherical, cylindrical, and planar dust grains moving through a plasma, *J. Geophys. Res.*, **101**(A5), pp. 10,793–10,796 (1996).

O'Brien, B. J. and Reasoner, D. L., Charged-Particle Lunar Environment Experiment, Technical Report SP-272, Section 10, NASA (1971).

Olhoeft, G. R., Frisillo, A. L. and Strangway, D. W., Electrical Properties of Lunar Soil Sample 15301,38, *J. Geophys. Res.*, **79**(11) (1974).

Poppe, A., Halekas, J. S. and Horányi, M., Negative potentials above the day-side lunar surface in the terrestrial plasma sheet: evidence of non-monotonic potentials, *Geophys. Res. Lett.*, **38**(L02103) (2011).

Poppe, A. and Horányi, M., Simulations of the Photoelectron Sheath and Dust Levitation on the Lunar Surface, *J. Geophys. Res.*, **115**(A08106) (2010).

Reasoner, D. L. and Burke, W. J., Characteristics of the Lunar Photoelectron Layer in the Geomagnetic Tail, *J. Geophys. Res.*, **77**(34), pp. 6671–6687 (1972a).

Reasoner, D. L. and Burke, W. J., Direct observation of the lunar photoelectron layer, *Proc. 3rd Lunar Sci. Conf.*, **3**, pp. 2639–2654 (1972b).

Reitz, J. R., Milford, J. F. and Christy, R. W., eds., *Foundations of Electromagnetic Theory*, Addison-Wesley, Reading, Mass., 4th edition (1993).

Rennilson, J. J. and Criswell, D. R., Surveyor observations of lunar horizon-glow, *The Moon*, **10**, pp. 121–142 (1974).

Rich, F. J., Reasoner, D. L. and Burke, W. J., Plasma Sheet at Lunar Distance: Characteristics and Interactions with the Lunar Surface, *J. Geophys. Res.*, **78**(34), pp. 8097–8112 (1973).

Robertson, S., Gulbis, A. A. S., Colwell, J. and Horányi, M., Dust grain charging and levitation in a weakly collisional plasma sheath, *Phys. Plasma*, **10**, pp. 3874–3880 (2003).

Robinson, M. S., Thomas, P. C., Veverka, J., Murchie, S. and Carcich, B., The nature of ponded deposits on Eros, *Nature*, **413**, pp. 396–400 (2001).

Roth, I., Hudson, M. K. and Temerin, M., Generation Models of Electron Conics, *J. Geophys. Res.*, **94**(A8), pp. 10,095–10,102 (1989).

Roussos, E., Krupp, N., Krüger, H. and Jones, G. H., Surface charging of Saturn's plasma-absorbing moons, *J. Geophys. Res.*, **115**(A08225) (2010).

Roux, A. *et al.*, The search coil magnetometer for THEMIS, *Space Sci. Rev.* (2008).

Saito, Y. *et al.*, Solar wind proton reflection at the lunar surface: Low energy ion measurement by MAP-PACE onboard SELENE (KAGUYA), *Geophys. Res. Lett.*, **35** (2008).

Sickafoose, A. A., Colwell, J. E., Horányi, M. and Robertson, S., Photoelectric charging of dust particles in vacuum, *Phys. Rev. Lett.*, **84**(26) (2000).

Sickafoose, A. A., Colwell, J. E., Horányi, M. and Robertson, S., Experimental investigations of photoelectric and triboelectric charging of dust, *J. Geophys. Res.*, **106**(A5), pp. 8343–8356 (2001).

Sickafoose, A. A., Colwell, J. E., Horányi, M. and Robertson, S., Experimental levitation of dust grains in a plasma sheath, *J. Geophys. Res.*, **107**(A11) (2002).

Slavin, J. A., Smith, E. J., Sibeck, D. G., Baker, D. N., Zwickl, R. D. and Akasofu, S.-I., An ISEE 3 Study of Average and Substorm Conditions in the Distant Magnetotail, *J. Geophys. Res.*, **90**(A11), pp. 10,875–10,895 (1985).

Sternglass, E. J., The Theory of Secondary Emission, Technical Report Sci. Pap. 1772, Westinghouse Res. Lab., Pittsburgh, PA (1954).

Sternovsky, Z., Chamberlin, P., Horányi, M., Robertson, S. and Wang, X., Variability of the lunar photoelectron sheath and dust mobility due to solar activity, *J. Geophys. Res.*, **113** (2008).

Stubbs, T. J., Vondrak, R. R. and Farrell, W. M., A dynamic fountain model for lunar dust, *Adv. Space Res.*, **37**, pp. 59–66 (2006).

Vasyliunas, V. M., Deep space plasma measurements, in R. H. Lovberg and H. R. Griem, eds., *Methods of Experimental Physics: Plasma Physics, Part B*, volume 9, pp. 49–88, Academic, Orlando, FL (1971).

Verboncoeur, J. P., Langdon, A. B. and Gladd, N. T., An object-oriented electromagnetic pic code, *Comp. Phys. Comm.*, **87**, pp. 199–211 (1995).

Veverka, J. *et al.*, Imaging of Small-Scale Features on 433 Eros from NEAR: Evidence for a Complex Regolith, *Science*, **292**(484) (2001).

Walbridge, E., Lunar photoelectron layer, *J. Geophys. Res.*, **78**(19), pp. 3668–3687 (1973).

Walch, B., Horányi, M. and Robertson, S., Measurement of the Charging of Individual Dust Grains in a Plasma, *IEEE Trans. Plasma Sci.*, **22**(2), pp. 97–102 (1994).

Walch, B., Horányi, M. and Robertson, S., Charging of Dust Grains in Plasma with Energetic Electrons, *Phys. Rev. Lett.*, **75**(5), pp. 838–842 (1995).

Wang, X., Colwell, J., Horányi, M. and Robertson, S., Charge of Dust on Surfaces in Plasma, *IEEE Trans. Plasma Sci.*, **35**(2), pp. 271–279 (2007a).

Wang, X., Horányi, M. and Robertson, S., Experiments on dust transport in plasma to investigate the origin of the lunar horizon glow, *J. Geophys. Res.*, **114** (2009).

Wang, X., Horányi, M. and Robertson, S., Investigation of dust transport on the lunar surface in a laboratory plasma with an electron beam, *J. Geophys. Res.*, **115**(A11102) (2010).

Wang, X., Horányi, M. and Robertson, S., Dust transport near electron beam impact and shadow boundaries, *Planet. Space Sci.* (2011).

Wang, X., Horányi, M., Sternovsky, Z., Robertson, S. and Morfill, G. E., A laboratory model of the lunar surface potential near boundaries between sunlit and shadowed regions, *Geophys. Res. Lett.*, **34** (2007b).

Whipple, E. C., Potentials of surfaces in space, *Rep. Prog. Phys.*, **44** (1981).

Willis, R. F., Anderegg, M., Feuerbacher, B. and Fitton, B., Photoemission and secondary electron emission from lunar surface material, in R. J. L. Grard, ed., *Photon and particle interactions with surfaces in space*, pp. 369–387, Springer, New York (1973).

Zook, H. A. and McCoy, J. E., Large scale lunar horizon glow and a high altitude lunar dust exosphere, *Geophys. Res. Lett.*, **18**(11), pp. 2117–2120 (1991).

Appendix A

Publications

A.1 Published Papers: Lunar

- **A. Poppe**, J. S. Halekas and M. Horányi, Negative potentials above the day-side lunar surface in the terrestrial plasma sheet: evidence of non-monotonic potentials, *Geophys. Res. Lett*, **38**, L02103, 2011
- **A. Poppe** and M. Horányi, Simulations of the Lunar Photoelectron Sheath and Dust Levitation on the Lunar Surface, *J. Geophys. Res.*, **115**, A08106, 2010
- Colwell J.E., S.R. Robertson, M. Horányi, **A. Poppe**, P. Wheeler, Lunar Dust Levitation, *J. Aero. Eng.*, NASA Exploration 2006 Granular Materials Workshop: Science and Engineering of the Lunar Soil, **22**, 2009

A.2 Published Papers: Other

- **A. Poppe**, D. James and M. Horányi, Measurements of the Terrestrial Dust Influx by the Cosmic Dust Experiment, *Planet. Space Sci.*, **59**(4), 319-326, 2011
- **A. Poppe**, B. Jacobsmeyer, D. James, M. Horányi, Simulation of Polyvinylidene Fluoride Detector Response to Hypervelocity Particle Impact, *Nuc. Inst. Meth. A*, **622**, 2010
- **A. Poppe**, D. James, B. Jacobsmeyer, M. Horányi, First Results from the Venetia Burney Student Dust Counter on the New Horizons Mission, *Geophys. Res. Lett.*, **37**, L11101, 2010

- M. Horányi, V. Hoxie, D. James, **A. Poppe**, C. Bryant, B. Grogan, B. Lamprecht, J. Mack, F. Bagenal, S. Batiste, N. Bunch, T. Chantanowich, F. Christensen, M. Colgan, T. Dunn, G. Drake, A. Fernandez, T. Finley, G. Holland, A. Jenkins, C. Krauss, E. Krauss, O. Krauss, M. Lankton, C. Mitchell, M. Neeland, T. Resse, K. Rash, G. Tate, C. Vaudrin, J. Westfall, The Student Dust Counter on the New Horizons Mission, *Space Sci. Rev.*, 2008

A.3 Papers in Review

- J. S. Halekas, **A. Poppe**, G. T. Delory, W. M. Farrell, M. Horányi, Solar Wind Electron Interaction with the Dayside Lunar Surface and Crustal Magnetic Fields: Evidence for Precursor Effects, *Earth Plan. Space*

A.4 Papers in Preparation

- A. Poppe and M. Horányi, The Effect of Nix and Hydra on the Putative Pluto-Charon Dust Cloud

- A. Poppe and M. Horányi, On the Role of κ-Distributions in Photoelectron Sheaths